Investigation of Metal–Organic Frameworks as Thin Films and gels

A Dissertation

Presented to

The Faculty of the Department of Chemical Engineering

University of Virginia

In Partial Fulfillment

of the Requirements for the Degree of

Doctor of Philosophy in Chemical Engineering

BY

PRINCE KUMAR VERMA

December 2023

APPROVAL SHEET

This
Dissertation
is submitted in partial fulfillment of the requirements
for the degree of
Doctor of Philosophy

Author: Prince Kumar Verma

This Dissertation has been read and approved by the examining committee:

Advisor: Gaurav Giri

Advisor:

Committee Member: Rachel Letteri

Committee Member: Joshua Choi

Committee Member: Robert Davis

Committee Member: Charles Machan

Committee Member:

Committee Member:

Accepted for the School of Engineering and Applied Science:

Jennifer L. West, School of Engineering and Applied Science

December 2023

ABSTRACT

Metal-organic frameworks (MOFs) are porous crystalline materials composed of inorganic metal clusters and organic linkers. The exceptionally high specific surface area and tunable porosity of MOFs make them excellent candidates for applications in catalysis, separation, sensing, and drug delivery. Most applications require the formation of MOF thin films and polymer-MOF composites. For instance, MOF thin films are required for implementing MOFs in catalysis and sensing applications. On the other hand, utilizing MOFs in separation and drug delivery requires the formation of polymer-MOF composites. Therefore, optimizing the synthesis conditions to prepare MOF thin films and polymer-MOF composites with desired properties is of great importance. This work identifies the existing knowledge gaps in the field of MOF thin films and polymer-MOF composites and addresses those issue.

In chapter 2, we discuss the formation of zirconium (Zr)-based anisotropic MOFs NU-901 and NU-1000 thin films with excellent stability and control over crystal orientation. We use a self-assembled monolayer (SAM) method to functionalize the substrate with carboxylic acid (–COOH) groups. We find that the presence of carboxylic acid groups facilitates the formation of NU-901 and NU-1000 crystals on the substrate during solvothermal synthesis, thus obtaining MOF thin films. Furthermore, the SAM method allows excellent adhesion of MOF crystals to the substrate as suggested by scotch tape stability test. We present a unique method to control the orientation of NU-901 and NU-1000 crystals on the substrate. We find that functionalizing the substrate with metal clusters promote crystal growth in the perpendicular direction as opposed to parallel orientation obtained for carboxylic acid functionalized substrate. We hypothesize that the presence of metal clusters on the substrate before MOF formation enhances nucleation density of MOF crystals, resulting in perpendicular growth of the MOF crystals. The method presented here to control the orientation of anisotropic MOF crystals has implications in catalysis, sensing, and separation.

While solvothermal method renders excellent MOF thin films, the method usually takes 24-72 h and is not easily scalable. In chapter 3, we present a solution shearing technique to fabricate large-area (~5 cm^2) thin films of NU-901 within 15 minutes. We study the effect of solution shearing parameters (i.e., substrate temperature and linker concentration) in NU-901 thin film properties (i.e., film thickness, crystallinity, and surface coverage). We find the NU-901 crystallinity increases with increasing temperature, while decreases with increasing linker concentration. On the other hand, film thickness increases with increasing temperature and linker concentration. In all cases, high surface coverage (> 90%) of MOF thin films is achieved. To show the generalizability of the solution shearing technique, we fabricate MOF-525 films, a Zr-based MOF, using solution shearing. The metalated MOF-525 films show electrocatalytic reduction of CO_2 to CO, which has implications in CO_2 capture and utilization. The demonstration of MOF thin film formation using solution shearing can pave the way to roll-to-roll coating of MOF thin films at industrial scale.

In chapter 4, we discuss the formation of polymer-MOF composite gels and shed light on the effects of polymer-MOF interactions on the formation of MOF within the gel. We use a one-pot synthesis method, where metal clusters interact with linker and polymer to allow simultaneous formation of MOF and gel network. We find that polymers containing carboxylic acid groups either inhibit or disrupt MOF formation within the gel compared to MOF formed in the absence of polymer. On the other hand, polymers containing hydroxyl groups do not affect MOF formation within the gel. Surprisingly, using a polymer, which has minimal interactions with metal cluster also allows formation of gel network. This suggests an exciting possibility of polymer entrapment within MOF pores and this entrapment restricts the movement of polymer chains out of the MOF pores, thus rendering a gel structure. We show the formation of polymer-MOF composite gels with various MOFs and polymers with the aim to report the future design of these composite gels for therapeutic applications.

ACKNOWLEDGEMENTS

First and foremost, I would like to thank my advisor, Professor Gaurav Giri (Gino). Gino, you have been a great advisor and your passion towards science is unmatchable. You have been a constant source of inspiration throughout my Ph.D. Thank you for being a good friend outside work. I had fun playing pool and chess with you.

I would like to thank my committee members: Professor Rachel Letteri, Professor Jousha Choi, Professor Robert Davis, and Professor Charles Machan. I learned a lot from each one of you, which has helped me grow as a researcher. Thank you for your valuable contribution in my growth. Special thanks to Professor Rachel Letteri for being an awesome mentor and teaching me scientific writing.

I would like to thank Prof. George Prpich for being my teaching mentor. TAing undergraduate lab was one of the best experiences I had as a Ph.D. student and you made it possible. Thank you for sharing your valuable experience about life.

My biggest thanks goes to my lab member: Dr. Stephanie Guthrie, Dr. Luke Huelsenbeck, Dr. Steve (Sangeun) Jung, Dr. Ashley Conley, Natalie Smith, Ankit Dhakal, and Meagan Renee Phister. Day in and day out, you have been there for me. I like working with you guys because you make lab work so much fun. Thank you for being my friend. Thank you for playing board games during break. The journey would not have been possible with you guys. I would like to thank my undergrads who contributed to the research: Brenna Bartholomew, Hailey Elizabeth Hall, Sean Kim, and Heisy Urrutia. Special thanks to Hailey for being the best undergrad I can ever ask for and Natalie Smith for being the best lab mate.

I would like to thank our collaborators. Thank you, Professor Charles Machan, Dr. Asa Nichols, and Dr. Connor Koellner for your work on electrocatalysis. Thank you, Professor Rachel Letteri, Dr. Mara Kuenen, and Mark Bannon for your work on polymer-MOF composite gel. Special

thanks to Mark Bannon for conducting loading and release studies. Thank you, Dr. Timur Islamoglu for your valuable insights on pore size calculation. Thank you, Dr. Kevin Stone for helping me run Synchrotron Facilities at SLAC National Laboratory. Thank you, Professor Geoffrey Geise, for letting me use Thermogravimetric Analysis instrument in your lab.

Thank you to all my wonderful friends at UVA: Natalie, Ankit, Meagan, Tracy, Mark, Vince, Dipesh, Colby, Pardeep, Aditi, Sammy. Thank you for your constant support. Thank you, Pardeep Kumar for teaching me how to drive. Special thanks to Tracy Kuper for being my best friend and dragging me into playing ultimate Frisbee.

I would like to thank my Pool crew and partners in crime: Ankit Dhakal, Meagan Phister, and Sammy Fieser. I love hanging out with you guys. I know I beat you guys in pool always (haha)!

I would like to thank my undergraduate friends: Ram, Ankit, Kashyap, Amit, Kishan. Thank you for your support.

I would like to thank my friends back in India. Thank you for always being there for me.

And, Finally, I would like to thank my Family. Thank you to my parents, Bheekam and Sunita. I know you have sacrificed a lot so that I can be here in USA and get the best possible education. Thank you to my sister Ritu for always supporting me.

TABLE OF CONTENTS

LIST OF TABLES

LIST OF FIGURES

Chapter 1 Introduction

1.1 Metal–organic frameworks

Metal–organic frameworks (MOFs) are a class of porous crystalline materials that have attracted significant attention in the scientific community due to their unique properties and potential applications.[1–4] MOFs are consisted of metal ions or clusters bridged by organic linkers to form a three-dimensional (3D) network of interconnected pores (**Figure 1.1**).[5]

Figure 1.1. *Schematic illustration of metal–organic framework (MOF) composed of inorganic metal ions/clusters and organic linkers.*

In most cases, metal clusters are synthesized first and organic linkers are added to metal clusters to form MOFs.[6,7] Synthesis of metal clusters is achieved by adding 'modulators' during the formation of metal clusters, which stabilize metal clusters by capping them.[6] Monocarboxylic acids are usually used as modulators. **Figure 1.2** illustrates a widely used procedure to synthesize MOFs. Metal clusters are procured by adding metal salt and modulator to the solvent followed by heating at high temperatures (100 to 120 °C). Then, organic linker is dissolved into the solution of metal cluster and the solution is heated at high temperatures to obtain MOFs.

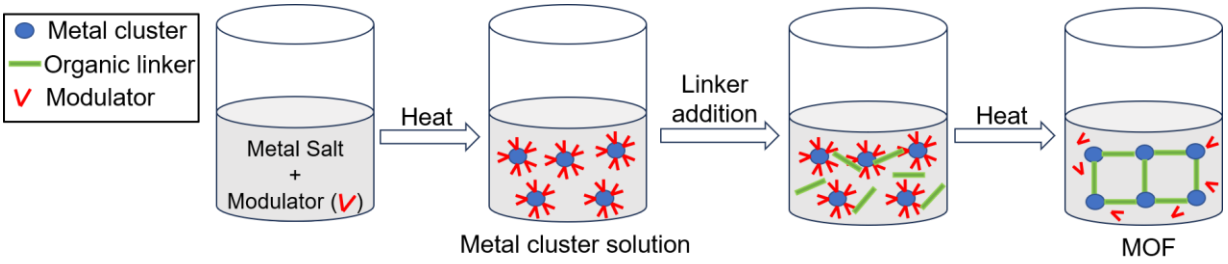

Figure 1.2. *Depiction of MOF synthesis process. Modulators are used as a capping agent to stabilize metal cluster solution and metal clusters react with organic linker to form MOF.*

Yaghi et al. coined the term MOF in 1990's and reported a first stable MOF in 1999.[8] Ever since the discovery of a stable MOF, thousands of MOFs have been synthesized with a range of specific surface areas (1000-6000 m^2/g) and pore sizes (2 Å to 40 Å).[1,9] The high specific surface area and tunable porosity of MOFs has enabled their application in gas storage,[10,11] separation,[12,13] catalysis,[14,15] and drug delivery.[16] For example, the permanent porosity of MOFs has shown potential to store gases like hydrogen, methane, and carbon dioxide.[17,18] Furthermore, the micropores of MOFs can separate gaseous mixtures like ethane/ethylene and methane/nitrogen.[19] Additionally, MOFs can slowly release drug molecules (from hours to days) due to their small pores which has implications in therapeutic applications.[20]

To target the specific applications and further improve the MOF performance, researchers have precisely tuned the chemical properties of MOFs. Chemical properties that can be tuned include metals in metal clusters and functional groups on organic linkers. For example, in one study, researchers modified the metal composition of MOFs to improve their catalytic performance for CO_2 reduction to CO.[21] They prepared a series of Ni/Ti bimetallic MOFs with different molar ratio of Ni/Ti and found that bimetallic MOFs produced an order of magnitude higher CO compared to monometallic Ni-MOF and Ti-MOF. Additionally, in another study, researchers placed amine ($–NH_2$) groups on organic linkers, which enabled the selective adsorption of CO_2 over N_2 due to the amine-CO_2 chemisorption.[22] Furthermore, conductive linkers can impart electrical conductivity to MOFs, which is useful for sensing and ion-separation.[23]

If the desired properties are difficult to achieve during MOF synthesis, post-synthetic modification (PSM) can modify the properties of MOFs after their synthesis. As the name suggests, PSM includes the modification or exchange of metal clusters or organic linkers in MOFs to enhance their performance. PSM can impart novel properties to MOFs that cannot be achieved by conventional synthesis methods. For example, in recent study, researchers synthesized a Zn-MOF and soaked Zn-MOF in Cu ions solution to substitute Zn with Cu to obtain a Cu-MOF.[24] Only

Cu-MOF showed catalytic activity, not the Zn-MOF, which suggested that Cu was responsible for catalysis. Furthermore, in another study, the organic linker of the MOF was replaced with another organic linker, which contained an acidic hydrogen.[25] The availability of acidic hydrogens improved the catalytic activity of MOF.

Another way to alter the properties of MOFs to enhance their performance is to intentionally create defects in the MOF structure. Defect engineering means removing metal clusters or organic linkers or both from the MOF structure to achieve desired functionalities, and these defects can be introduced either during MOF synthesis or after MOF synthesis. For example, in one study, MOF was soaked in HCl solution to remove the coordinated linker from the MOF structure to introduce unsaturated metal sites and increase pore volume of MOF.[26] The presence of unsaturated metal sites increased iodine (I_2) adsorption by more than 45% compared to the parent MOF, suggesting creating defects can enhance MOF performance in radioactive waste removal. Furthermore, removing linkers to create unsaturated metal sites, which serve as single-site catalysts or adsorption sites, can enhance the catalytic activity and sorptive capability of MOFs.[27,28]

The above-mentioned examples demonstrate the potential and versatility of MOFs for various applications. To enable MOFs for applications like catalysis and sensing, formation of MOF particles on a substrate to fabricate MOF thin films is required. For instance, growing MOF particles on a conductive substrate is necessary for electrocatalysis.[29,30] Furthermore, implementation of MOFs as sensors demands MOF formation on various substrates like electrodes and fibers.[31] On the other hand, utilization of MOFs for separation and drug delivery requires incorporation of MOFs with polymers to make polymer-MOF composites. For example, growing MOF particles on a porous polymer support to make polymer-MOF composite membrane is a prerequisite for gas and ion separations,[32] and making polymer-MOF composite gels equips MOFs for drug-delivery application.[20,33]

Since multiple applications require formation of either MOF thin films or polymer-MOF composites, optimizing the synthesis conditions to obtain MOF thin films and polymer-MOF composites with desired properties for target applications is indispensable. Therefore, this thesis includes the challenges and knowledge gaps in the field of MOF thin films and polymer-MOF composites, and our potential solutions to address those gaps. In the first part, I will talk about the MOF thin film formation addressing two key challenges: (i) controlling orientation of anisotropic MOF crystals to the substrate, which has implication in catalysis and sensing, and (ii) making MOF thin films using a scalable technique. The second part will focus on understanding the fundamentals of polymer-MOF composite gel formation and make the composite gel formation process more facile.

1.2 Metal-organic framework thin films

Formation of MOFs as thin films opens an avenue for multiple applications like sensing, separation, and catalysis.[34] To optimize the performance of MOFs in these applications, controlling the properties of MOF thin films (i.e., film thickness, crystal orientation, surface coverage, stability, etc.) is critical.

1.2.1 Thickness

The thickness of MOF thin films is an important parameter that can significantly impact their performance. For example, in sensing, a thick MOF film may provide a high density of binding sites, leading to excellent sensitivity. However, if the film is too thick, it can hinder the diffusion of analyte molecules through the film, increasing the sensor's response time.[35] On the other hand, a very thin film can reduce the sensor's response time, but can lead to poor sensitivity.[36] Similarly, in separation, the permeability depends on the film thickness. Therefore, optimizing the thickness of MOF thin films is critical to achieving high performances.

1.2.2 Crystal orientation

For anisotropic MOFs, pores are aligned along one direction unlike the isotropic MOFs. Therefore, orientation of anisotropic MOFs to the substrate is crucial such that pores are

accessible to guest molecules. Anisotropic MOFs can exhibit two different orientations: (i) pores are aligned parallel to the substrate, termed as parallel orientation, and (ii) pores are aligned perpendicular to the substrate, termed as perpendicular orientation (**Figure 1.3**).[7] Interestingly, pores are accessible to guest molecules only in perpendicular orientation. In this regard, Yoon et al.,[37] studied the effects of PCN-222 MOF orientation on the capability of PCN-222 to adsorb volatile organics like toluene, hexane, and benzene. They found that the perpendicularly oriented PCN-222 MOF adsorbed a higher amount of volatile solvent due to its well-aligned pores. Therefore, growing MOF thin films with desired crystal orientation can maximize MOF performance.

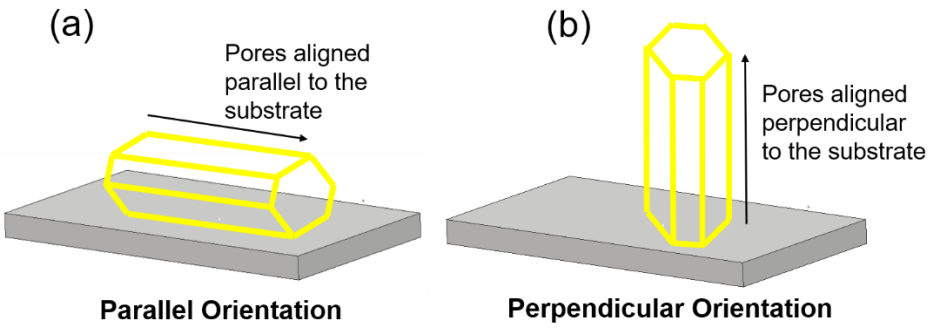

Figure 1.3. *Orientation of an anisotropic MOF crystal in two ways: (a) parallel orientation, where pores are parallel to the substrate and (b) perpendicular orientation, where pores are perpendicular to the substrate.*

1.2.3 Surface coverage

Surface coverage refers to the percentage of the substrate covered by MOF crystals. In most cases, a high surface coverage (ideally 100%) is desired. High surface coverage provides a high density of binding sites for guest molecules, which has implications in catalysis and sensing. For instance, a high density of binding sites can act as a scaffold to deposit a high amount of catalyst molecules inside the MOF, leading to excellent catalytic activity. In addition to binding sites, a high surface coverage can also reduce the chances of poor crystal intergrowth and pinholes (small voids in the MOF thin film) .[38] To this end, a study reported that crystal intergrowth and pinholes of nanometer sizes significantly influenced the mass transport of guest molecules

through MOF thin films.[39] Therefore, synthesizing MOF thin films with a high surface area and high surface coverage is desirable.

1.2.4 Stability

Since many applications require harsh conditions, like acidic and basic environments, and high temperatures, strong adhesion of MOF crystals to the substrate is necessary for their durability.[40,41] Poor adhesion of MOF crystals may impede the separation performance of MOF thin films.[32] Furthermore, applications like electrocatalysis, require deposition of catalysts inside MOF crystals, which is carried out in harsh organic solvents for several hours.[42] To survive under these conditions, MOF crystals must be strongly adhered to the substrate.

Therefore, the properties of MOF thin films can dramatically affect their performance and ability to control these properties is crucial for their future development. In the next section, the techniques to fabricate MOF thin films will be discussed, and how these techniques can provide control over various properties.

1.3 MOF thin film fabrication techniques

The MOF thin film synthesis can be realized using two ways – (i) forming MOFs directly on the substrate and (ii) depositing pre-formed MOF crystals on the substrate.

1.3.1 Forming MOFs directly on the substrate

1.3.1.1 Solvothermal synthesis

Solvothermal synthesis is one of the simplest methods to grow MOF thin films. In solvothermal synthesis (**Figure 1.4**), a substrate of interest is immersed in a MOF precursor solution (a solution containing metal clusters and organic linker) and heated at high temperatures for several hours.[29,43] During this time, MOF crystals grow in the solution as well as on the substrate. The crystal growth on the substrate provides a MOF thin film.

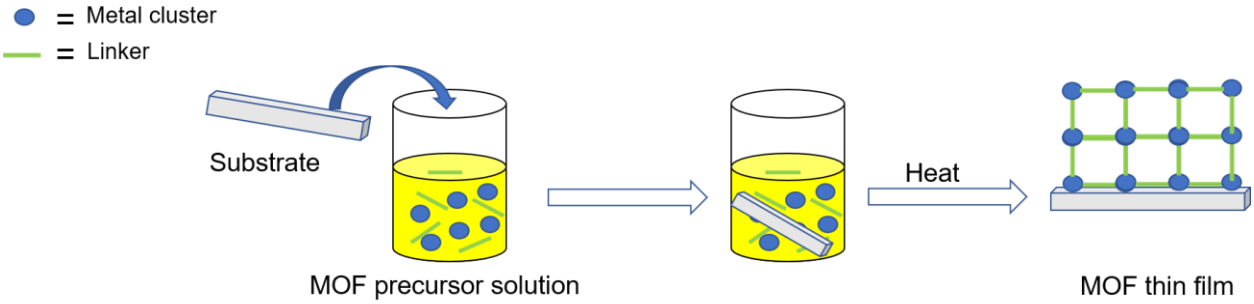

Figure 1.4. *Schematic illustration of making MOF thin films using solvothermal method. A functionalized substrate is immersed into MOF precursor solution followed by heating to synthesis MOF thin film.*

However, the substrate's surface significantly influences the MOF growth, particularly, it's acid/base properties.[44] Researchers found that growth on the surface is initiated by the binding of organic linker to the substrate. Since most MOFs contain carboxylic acid (–COOH) groups, the linker can't bind to an acidic surface, such as silica, which results in no film formation. On the other hand, MOFs containing both acidic and basic linkers can grow on a variety of substrates. Since growth on the surface is initiated by organic linkers, people have modified the surface with organic linkers to promote MOF formation.[45] The presence of organic linkers on the substrate enhances the surface coverage and provides fully covered films compared to one obtained with bare substrate only.

In terms of thin film properties, the solvothermal method is a versatile tool. The Solvothermal method creates micron level thick films (10 μm to 40 μm), and thickness can be controlled by varying the synthesis time and precursors' concentrations.[46] However, thinner films (on a nanometer scale) are difficult to achieve using the solvothermal method. On the other hand, the orientation of MOF crystals can be controlled by terminating the surface with different functional groups. For instance, a study reported that changing the surface terminating group from (–COOH) to hydroxyl (–OH) changed the orientation of MOF crystals.[47] As far as the stability is concerned, growth on bare substrate provides weak binding of MOF crystals to the substrate, while crystals strongly adhere to functionalized substrate due to the covalent binding between the substrate and functionalized groups.[48]

1.3.1.2 Layer-by-layer (LBL) growth

In LBL method (**Figure 1.5**),[49] the substrate is immersed into a metal cluster solution during which metal clusters interact with the surface to form a layer of metal clusters. Afterward, the substrate is immersed into an organic linker solution and linkers react with metal clusters to form MOF on the substrate. By repeating the number of deposition cycles, MOF thin films is created.

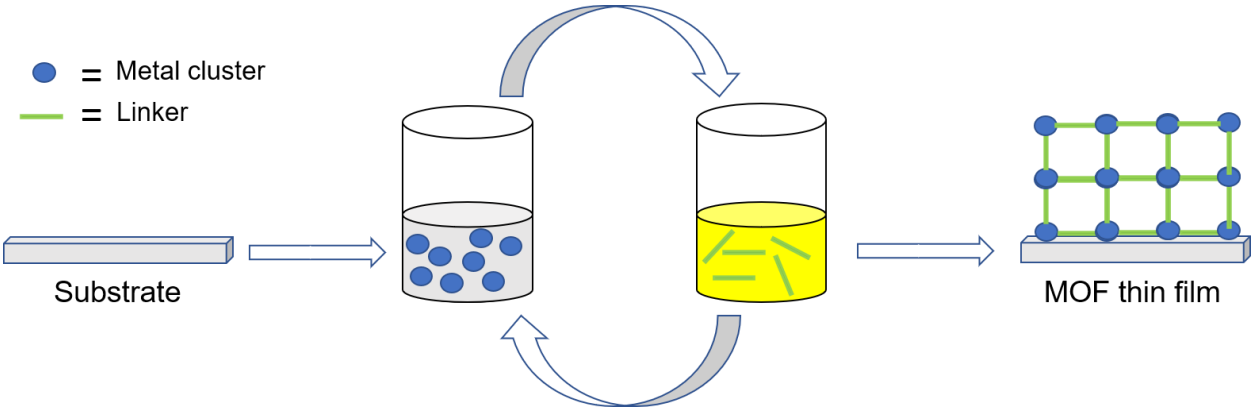

Figure 1.5. *Schematic illustration of making MOF thin films using layer-by-layer (LBL) method. A functionalized substrate is repeatedly immersed into metal cluster and linker solution to synthesize MOF thin film.*

Similar to solvothermal method, utilization of bare substrate results in no film formation. Therefore, functionalizing the substrate with (–COOH) is essential prior to film growth. For example, in one study, researchers modified the gold surface with (–COOH) groups to grow MOF thin films.[50] Furthermore, functionalizing the substrate with different functional groups, such as (–COOH) and (–OH), can provide different orientation of MOF crystals, which shows that LBL method is useful to obtain the desired orientation of MOF crystals.[49] Additionally, the prepared films are stable due to the strong binding of functional groups to the substrate. In terms of thickness, LBL method can synthesize films from few nanometers (20 to 40 nm) to few microns (1 to 2 μm) by controlling the number of deposition cycles, which is remarkable.[50] The ability of LBL method to synthesize ultrathin films is useful for separations.

1.3.2 Depositing pre-formed MOF crystals on the substrate

1.3.2.1 Dip coating

In dip coating (**Figure 1.6**),[51] a stable colloidal solution of MOF crystal is prepared and the substrate is dipped into the colloidal solution. Afterward, the substrate is withdrawn at a controlled rate during which MOF crystals get deposited on the substrate.

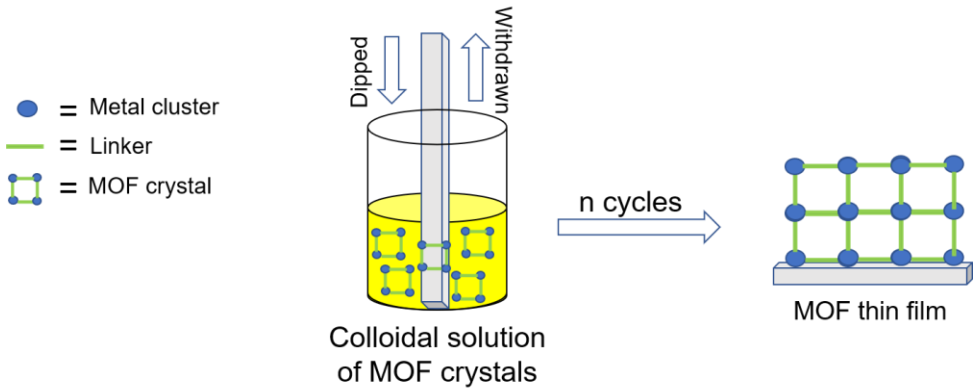

Figure 1.6. *Schematic illustration of making MOF thin films using dip coating. A substrate is repeatedly dipped into the MOF colloidal solution to synthesize MOF thin film.*

Although dip coating results in the formation of fully covered films, dip coating does not provide precise control over crystal orientation due to the presence of pre-formed crystals, which could get deposited randomly. In terms of thickness, dip coating can prepare films from few nanometers to few microns, and the thickness can be controlled by tuning the number of dip coating cycles and withdrawal rate.[52] However, the stability of films is questionable since particles adhere weakly to the substrate during dip coating.[53]

1.3.2.2 Electrophoretic deposition (EPD)

In EPD (**Figure 1.7**),[54] a suspension of MOF particles in prepared and two conductive substrates (one acts as a cathode and other one acts as an anode) are placed in the suspension. Then, an electric field is applied which migrate the charged MOF crystals towards the oppositely charged substrate and MOF particles get deposited on the substrate.

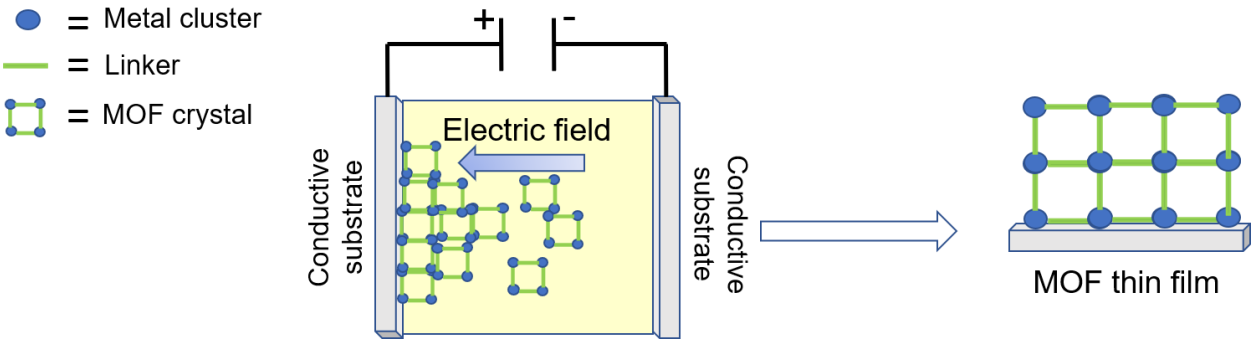

Figure 1.7. *Schematic illustration of making MOF thin films using electrophoretic deposition. Electric filed is applied to migrate MOF particle towards the conductive substrate to synthesize MOF thin film.*

Although EPD creates fully covered films with well intergrown crystals, the technique is limited to conductive substrate only.[54–56] Similar to dip coating, deposition of pre-formed MOF crystal results in random orientation of MOF crystals on the conductive substrate.[54] EPD generally provides micron level (1 to 10 μm) thick films, which can be controlled by varying the applied potential and deposition time. For example, in one study, researchers found that film thickness increased upon increasing the applied potential.[56] In terms of film stability, EPD renders good adhesion of MOF crystals to the substrate due to the electrostatic interactions between the MOF crystals and the conductive substrate.

1.3.3 Meniscus-guided coating to make MOF thin films

A meniscus-guided technique called solution shearing has been shown to create large-area thin films of polymers and organic semiconductors within minutes, with control over crystal structure and crystal orientation.[57–60] In solution shearing, a solution of interest is sandwiched between a moving blade and a heated substrate as depicted in **Figure 1.8**.[57] A meniscus forms between the blade and a substrate, and solvent starts evaporating from the meniscus. As the solvent evaporates from the meniscus, the solute concentration increases, which results in supersaturation. The supersaturation promotes the crystallization of solute molecules followed by deposition on the substrate. As the blade moves, it spreads crystals along the substrate and create a thin film. Solution shearing is a versatile technique and by tuning solution shearing

parameters, such as blade speed, substate temperature, solute concentration, and solvent, thin films properties can be controlled.[61]

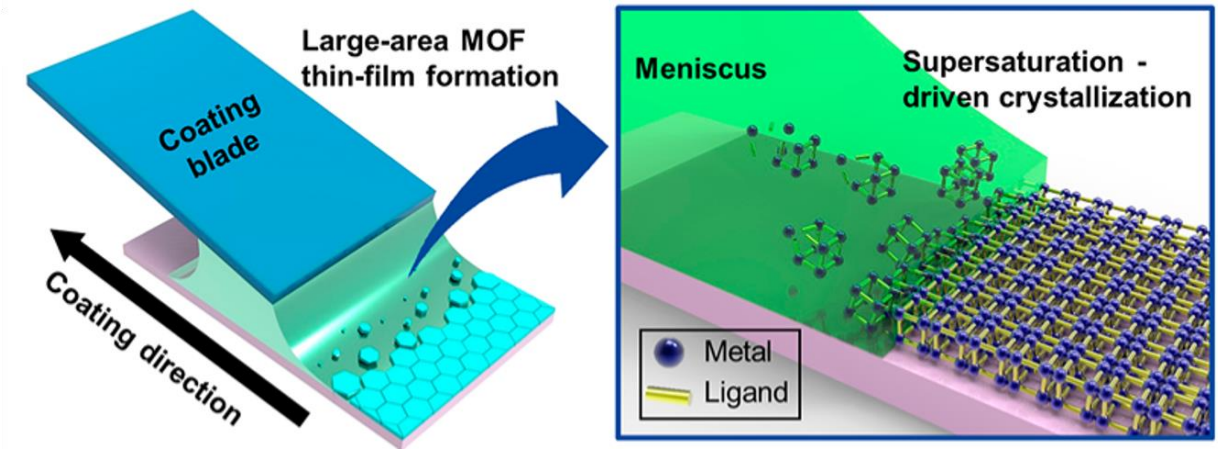

Figure 1.8. *Schematic illustration of making MOF thin films using solution shearing. Solvent evaporation from the meniscus initiate MOF crystallization and blade movement creates a MOF thin film.*[62] *Figure was reprinted with permission from ref. [62]. Copyright 2019 American Chemical Society.*

Two characteristic coating regimes generally exist in solution shearing – evaporative regime and Landau – Levich (LL) regime (**Figure 1.9**).[63] At lower blade speeds, evaporative regime exists, where the solvent evaporation and solute deposition occurs at a similar time scale, means the film is created as the blade is moving. In evaporative regime, the film thickness decreases with increasing blade speed. Conversely, at higher blade speeds, LL regime exists, where film deposition occurs faster than solvent evaporation. In LL regime, the solvent is dragged out from the meniscus due to strong viscous forces which results in the deposition of a liquid film and liquid film dries afterward to create a solid thin film. Unlike evaporative regime, the film thickness increases with blade speed in LL regime.

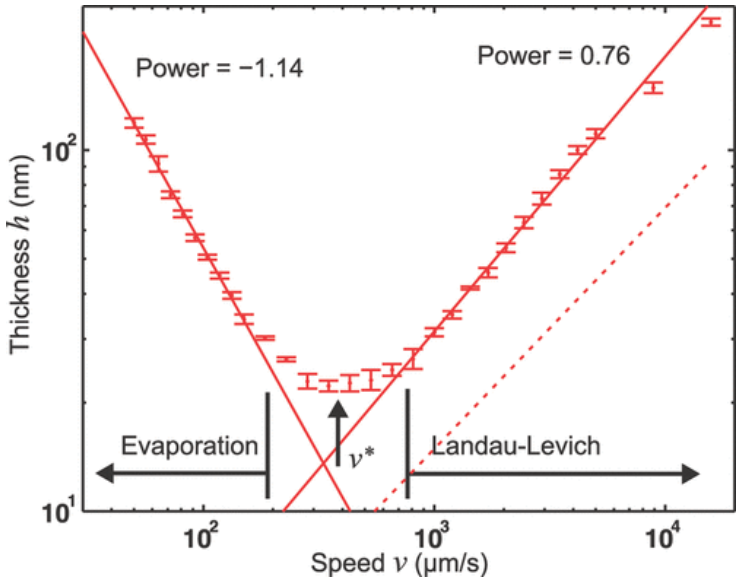

Figure 1.9. *Two regimes of solution shearing: Evaporation regime and Landau-Levich regime.[63] Figure was reprinted with permission from ref. [63]. Copyright 2009 American Chemical Society.*

Although solution shearing has been applied to various fields, it is relatively young in the MOF field. The first example of solution shearing to create MOF thin films was demonstrated by Park et al. in 2019.[62] Park et al. were able to create 40 cm^2 thin films within 12 seconds, showing that solution shearing is applicable to MOFs. They showed precise control over thin film properties by tuning the solution shearing parameters. For example, they created fully covered films at lower blade speeds and found that increasing blade speed reduced surface coverage. Furthermore, they found that both evaporative and LL regime exists and followed the same trends as described above. Additionally, they showed the tuning of crystal size and morphology by varying blade speed. In terms of film stability, the particles adhered strongly to the substrate and they fabricated films on a wide range of substrates. Solution shearing is relatively new to the MOF field but the above example showed that it can resolve the existing issues generally like scalability and rapid fabrication.[64]

In the next section, I will discuss the limitations of MOFs and how combining MOFs with polymers can overcome those limitations. Afterward, I will discuss the potential of polymer-MOF composites in various fields, and the existing knowledge gaps and challenges.

1.4 Polymer-MOF composites

Their extremely high specific surface area and tunable porosity make MOFs excellent candidates for biological applications.[16,65,66] Despite the significant advances in the MOF field, the brittle nature of MOFs still limits their biomedical applications. Poor dispersion and aggregation of MOF particles in the solution are responsible for poor biocompatibility of MOFs.[67] Since polymers are frequently studied in biomedical field,[68–71] MOFs have been combined with polymers to improve the biocompatibility of MOFs.[20,65,72–74] Over the last decade, many synthetic routes have been utilized to make polymer-MOF composites. There are mainly two ways to make polymer-MOF composites: (i) Adding polymers to pre-formed MOF particles (ex-situ method) and (ii) synthesizing MOF in the presence of polymer (in-situ method).

1.4.1 Ex-situ methods to make polymer-MOF composites

1.4.1.1 Coating MOF particles with polymers through non-covalent interactions

In this approach, MOF particles are coated with polymers or polymers are attached to MOF surface to make a core-shell like structure.[75] This can be achieved by using polymers, which interact with MOF components via non-covalent interactions (like electrostatic interactions or hydrogen bonds). For example, in one study, MOF particles were synthesized and polymers containing ionized carboxylic acid groups (COO^-) were attached to the surface due to the electrostatic interactions between (COO^-) and open metal sites of MOFs (**Figure 1.10a**).[76] The polymer attachment improved the dispersion and stability of MOF particles in the aqueous solution (**Figure 1.10b**). In another study, MOF particles were coated with sodium alginate (SA) by soaking MOF particles in SA solution. The carboxylic groups (–COOH) on alginate interacted with metal sites of MOFs through hydrogen binding. The SA coated MOF particles released drug molecules under physiological conditions, suggesting the applicability of MOF-polymer composites in drug delivery.

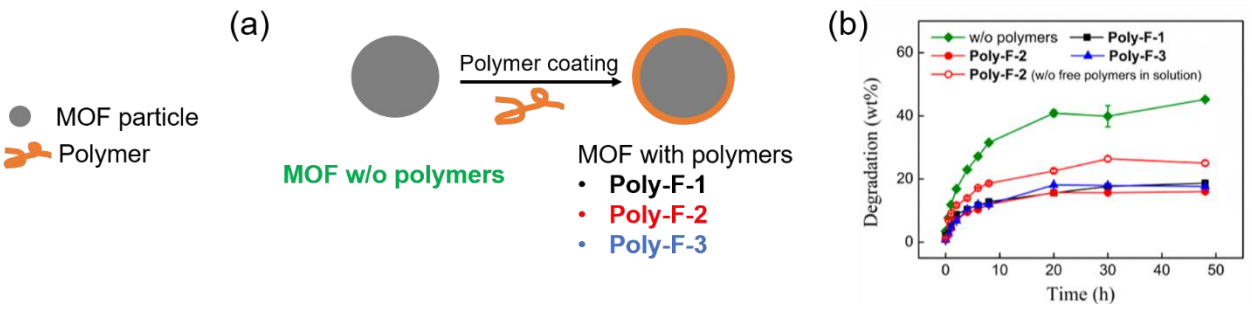

Figure 1.10. *(a) Schematic illustration of making polymer-MOF composite by coating polymers on the MOF surface.[76] (b) Degradation profile of MOF particle with and without the coating of polymers in an aqueous medium. Figure was reprinted with permission from ref. [76]. Copyright 2014 American Chemical Society.*

However, coating the MOF surface with polymers does not provide stable polymer-MOF composites due to the weak binding between polymers and MOFs. To improve the composite stability, polymers have been covalently attached to the MOF surface.

1.4.1.2 Coating MOF particles with polymers through covalent interactions

In this approach, polymers are attached to the MOF particles through covalent binding.[77] This is achieved by placing a functional group within MOF structure, which forms a covalent bond with polymers. In most cases, organic linker is functionalized with the desired group. Using this approach, in one study, MOF particles were synthesized possessing azide moieties (N_3) within the framework.[78] Then, poly(ethylene glycol) (PEG) containing propargylic groups (–C≡CH) reacted with the N_3 groups to form a covalent bond and PEG-coated MOF particles were obtained (**Figure 1.11**). The PEG-coated MOF showed no aggregation in phosphate buffered saline (PBS) (microscope image in **Figure 1.11**), indicating the excellent biocompatibility. Furthermore, the PEG-coated MOF released drug molecules faster at a pH 5.5 compared to 7.4 thus showing pH responsive behavior (**Figure 1.11**), which demonstrates the potential of PEG-coated MOF for therapeutic applications. Another approach is to covalently bind monomers to MOF structure and carry out polymerization to wrap polymers around MOF particles. For example, in one study, the monomers were polymerized at the MOF surface, which improved the dispersibility of MOF particles.[79]

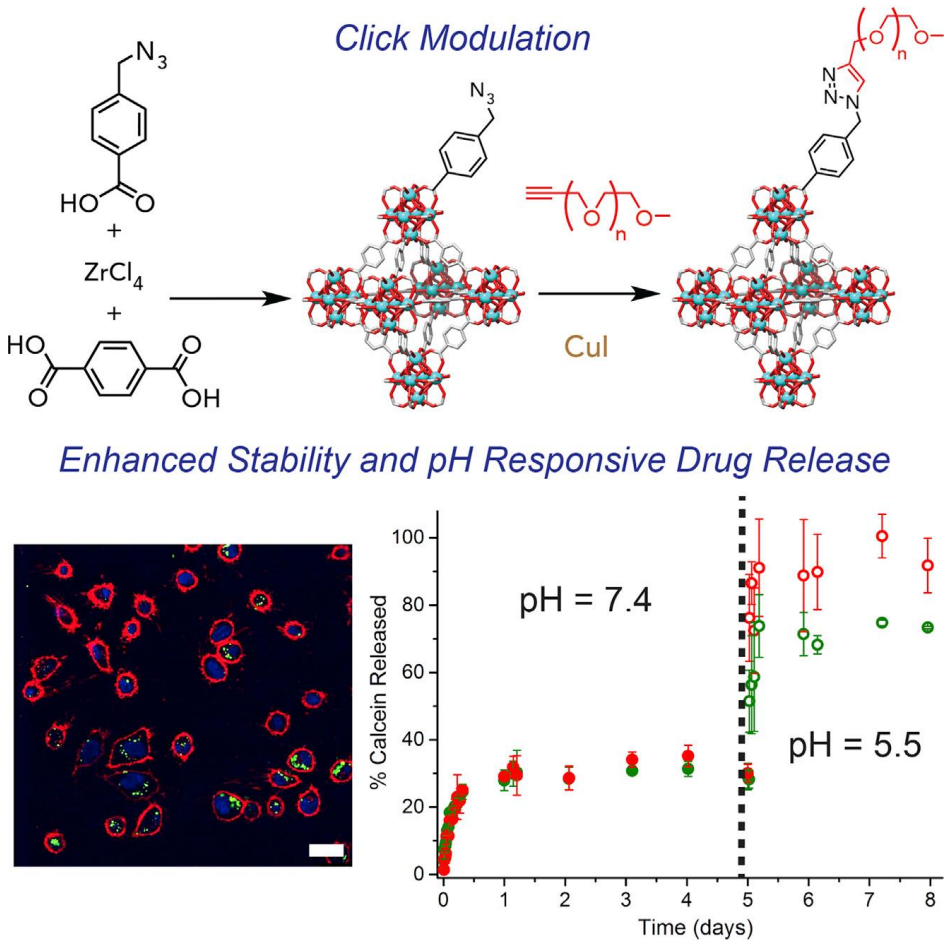

Figure 1.11. *Schematic illustration of making polymer-MOF composite by covalently adding a polymer to MOF particle using click chemistry.[78] The polymer-MOF composite showed enhanced stability in a buffer solution and slowly release drug molecules at various pH. Figure was reprinted with permission from ref. [78]. Copyright 2017 Elsevier.*

Although, covalent attachment of polymers to MOF improves the composite stability, the synthesis process is too complicated and time consuming. Functionalization of MOFs with a desired function group alone is a complicated process and attaching polymers make it even more tedious. Therefore, to reduce the time and complexity of polymer-MOF composite formation process, researches have utilized in situ methods,[80] where MOF particles are synthesized in the presence of polymers.

1.4.2 *In-situ* methods to make polymer-MOF composites

1.4.2.1 Using polymeric linkers to make polymer-MOF composites

Polymeric linkers are a combination of polymers and organic linkers in which organic linkers are placed on the backbone of polymers.[81–83] The Cohen group in 2015 introduced the concept of polymeric linkers to make MOFs and coined a term 'polyMOF' (**Figure 1.12**).[81] They used a one-pot method, where polymeric linkers are combined with metal clusters and polymers are incorporated within the MOF framework. By tuning the polymer chemistry and the space between organic linkers, the shape and size of MOF particles can be controlled.[81] Furthermore, incorporation of polymers in the framework improves the colloidal stability of MOF particles, which can be beneficial for processibility of MOF particles.[82]

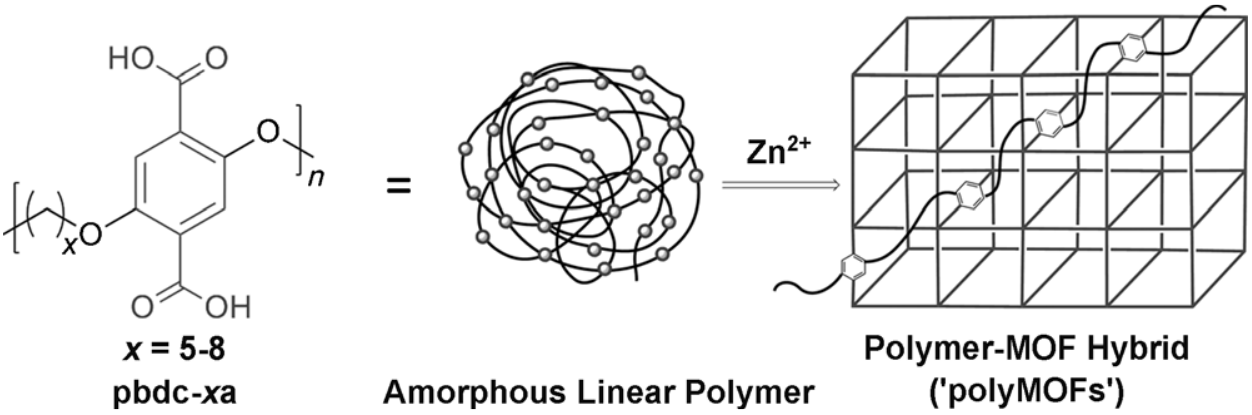

Figure 1.12. *Schematic illustration of making polyMOFs using polymeric linkers and metal clusters.[81] Figure was reprinted with permission from ref. [81]. Copyright 2015 Wiley-VCH.*

Although this method avoids unnecessary post-synthetic steps where polymers are added after MOF formation, there are some drawbacks. The spacing between organic linkers can inhibit MOF formation and finding the suitable spacing between organic linkers that facilitates MOF formation could be challenging.[81] Additionally, the incorporation of polymers into the MOF framework reduces specific surface area due to the space occupied by polymers, and may introduce defects into MOF structure.[82] Furthermore, it could be complicated to combine any

organic linker with any polymer. To avoid these drawbacks, polymers containing metal-binding functional groups have been used to make polymer-MOF composites.

1.4.2.2 Polymer-MOF composite formation from polymers containing metal-binding functional groups

In this process, polymers containing carboxylic acid (–COOH) groups, hydroxyl (–OH) groups, or amine ($–NH_2$) groups are utilized to make polymer-MOF composites.[84–86] These functional groups on polymers interact with metal cluster which facilitates the polymer incorporation in the framework. Polymer incorporation can be achieved in two ways: (i) a two-step process where metal cluster first react with polymers and then linker is added afterward, and (ii) a one-step process where metal clusters react with polymer and linker simultaneously.

1.4.2.2.1 Two-step process

In this process,[85–88] polymers are added to a solution of metal clusters and interactions between polymers and metal clusters cross-link polymer chains to create a polymer-metal gel. Afterward, organic linker is added to the polymer-metal gel and linker reacts with metal clusters to form MOF particles, resulting in a polymer-MOF composite gel. For example, in one study, alginate polymer is used, which contained (–COOH) groups and (–OH) groups, to create polymer-MOF composite gel.[85] First, they added alginate solution to metal ion (Cu^{+2}) solution which formed a gel due to interactions between alginate (–COOH) groups and metal ions (**Figure 1.13a**). Then, they transferred the gel to the trimesic acid solution and trimesic acid reacted with Cu^{+2} to form HKUST-1 MOF thus obtaining alginate-HKUST-1 composite gel (**Figure 1.13d**). The authors showed that the synthesis procedure could be generalized to multiple MOFs and fabricated alginate-MIL-100, alginate-ZIF-8, and alginate-ZIF-67 composite gels. The composite gels showed the excelled dye adsorption capabilities, which has implications for water remediation.

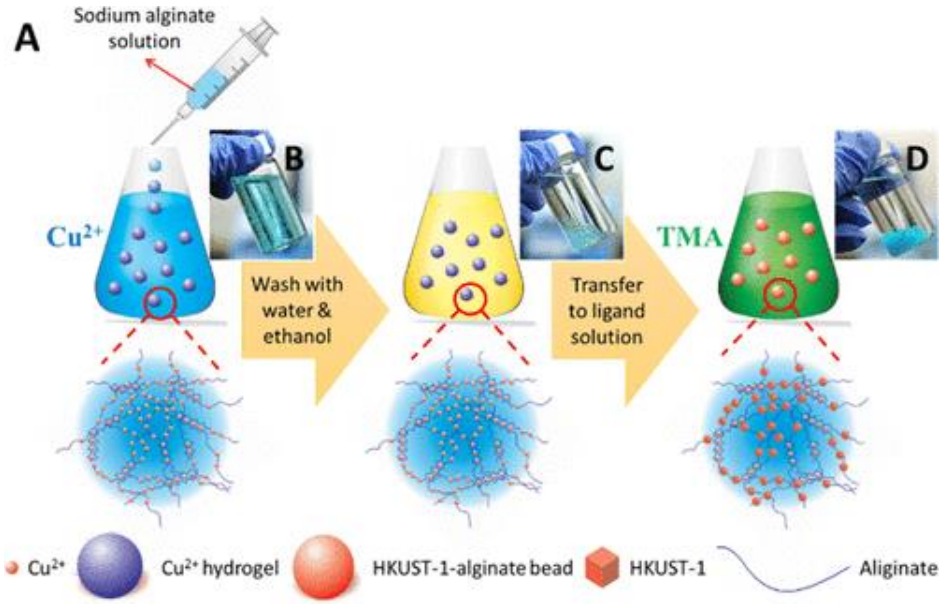

***Figure 1.13**. Schematic illustration of making polymer-MOF composite gel using a two-step process.[85] (A) Metal ions/clusters are added to an alginate solution to make alginate-metal hydrogel, which is shown in (B). (C) Alginate-metal hydrogel is washed with water and ethanol and (D) transferred to the linker solution to synthesize alginate-MOF hydrogel. Figure was reprinted with permission from ref. [85]. Copyright 2016 American Chemical Society*

Similarly, another study used alginate to synthesize alginate-MOF-808 composite gel and found that composite gel adsorbed an order of magnitude higher methylene blue (MB) compared to alginate-metal gel and MOF-808.[87] In another example, chitosan was used as polymer, which contained (–OH) groups and ($–NH_2$) groups.[89] The addition of metal clusters solution to the chitosan solution facilitated the formation of gel beads due to interactions between metal clusters and ($–NH_2$) groups of chitosan. The subsequent addition of organic linker to the gel beads promoted the formation of chitosan-MOF gel composite. The chitosan-MOF gel composites showed excellent tetracycline removal from water since excessive amount of tetracycline in human body can cause some allergies and toxicity.

1.4.2.2.2 One-step process

In this method, metal clusters react with polymers and organic linkers simultaneously, which promote the formation of MOF particles and gel network at the same time. In one study, alginate solution was added to a solution containing metal ions (Co^{+2}) and organic linker (2-

methylimidazole) resulting in a formation of alginate-ZIF-67 composite gel (**Figure 1.14**).[90] The authors also prepared the alginate-ZIF-67 composite gel using two-step process and found that one-step process produced more crystalline ZIF-67 within the composite compared to two-step process, indicating that one-step process is superior in preserving MOF crystallinity within the composite gel.

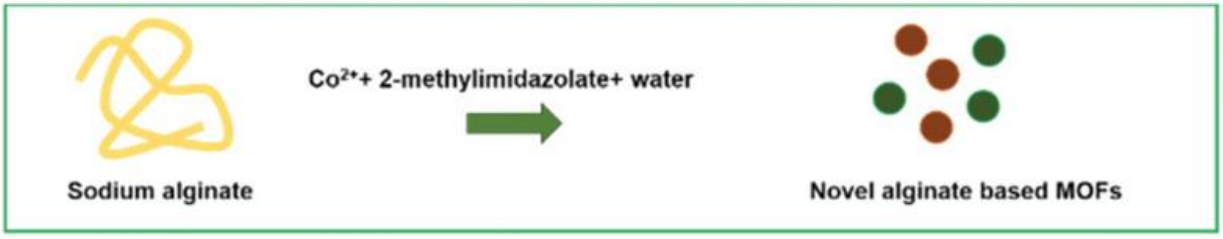

Figure 1.14. *Schematic illustration of making polymer-MOF composite hydrogel using a one-step process. Metal ions/clusters react simultaneously with polymers and linker to obtain polymer-MOF composite hydrigel.[90] Figure was reprinted with permission from ref. [90]. Copyright 2019 Royal Society of Chemistry.*

Amongst the synthesis routes discussed above to make polymer-MOF composites, utilization of polymers containing metal-binding functional groups is facile and avoids complicated syntheses. Specifically, a one-step method has been proven to create composites while not affecting MOF formation. Therefore, the second part of the thesis will focus on synthesizing polymer-MOF composites using a one-step process. I will address the challenges and existing knowledge gaps in the literature and discuss the implications of polymer-MOF composites in biomedical and environmental applications.

1.5 Summary of dissertation

Based on the presented background, this thesis will investigate the crystallization of MOFs in the presence of a substrate and polymers. We hope that better understanding of MOF crystallization will help in developing scalable processes to make MOF thin films and polymer-MOF composite gels. We first present a unique way to alter the orientation of an anisotropic MOF

on the substrate, which could improve the MOF performance in catalysis and separation. After that, we apply solution shearing to make large-area MOF thin films, which has the potential to synthesize MOF thin films at industrial scale. In the end, we present a one-step process to make polymer-MOF composite gels, which are useful for drug delivery. In the following sections, a brief summary of each section has been presented.

1.5.1 Controlling polymorphism and orientation of NU-901/NU-1000 metal-organic framework thin films

Chapter 2 will focus on improving the stability of MOF thin films through self-assembled monolayer (SAM) method. We hypothesize that terminating the surface with carboxylic acid group promote the formation of NU-901 and NU-1000 crystals on the substrate. We discuss the effect of modulators on polymorphic phases. We further understand the effect of nucleation density on crystal orientation to the substrate. We hypothesize that increasing the nucleation density of MOF crystal on the substrate inhibits crystal growth parallel to the substrate and crystals grow in the perpendicular direction. The ability to control crystal orientation by tuning nucleation density has implications in catalysis and separation.

1.5.2 Solution shearing of zirconium (Zr)-based metal-organic frameworks NU-901 and MOF-525 thin films for electrocatalytic reduction applications

Chapter 3 will discuss solution shearing technique to create MOF thin films. We explore the possibility of forming Zr-based MOF thin films by evaporating the solvent. We hypothesize that thin film properties (i.e., film thickness, MOF crystallinity, and surface coverage) can be tuned by varying solution shearing parameters, like, blade speed, substrate temperature, and precursor concentration. We further discuss the possibility of creating large-area MOF thin films using solution shearing. In the end, we discuss the utility of the thin films for electrocatalytic reduction of CO_2. The solution shearing process is similar to roll to roll coating and can be employed at industrial scale.

1.5.3 Understanding the effects of interactions between polymers and metal-organic framework (MOF) on polymer-MOF composite gel formation

Chapter 4 will explore the formation of polymer-MOF composite gels using polymers, which have metal-binding functional groups. We hypothesize that forming MOFs in the presence of these polymers will result in simultaneous formation of MOF and gel network, thus rendering polymer-MOF composite gel. We will vary the strength of interactions between polymers and metal clusters and study its effect on the formation/crystallinity of MOF within the gel compared to MOF formation in the absence of polymers. Additionally, we will test the utility of these composite gels for drug delivery.

1.5.4 Conclusion and future work

We will discuss the potential of the work discussed here in implementing MOFs in commercial applications. We will look at some of the possible future directions for each project.

1.6 References

(1) Furukawa, H.; Cordova, K. E.; O'Keeffe, M.; Yaghi, O. M. The Chemistry and Applications of Metal-Organic Frameworks. *Science.* **2013**, *341* (6149), 1230444.

(2) Ma, S.; Zhou, H. C. Gas Storage in Porous Metal-Organic Frameworks for Clean Energy Applications. *Chem. Commun.* **2010**, *46* (1), 44–53.

(3) Zhao, Z.; Ma, X.; Li, Z.; Lin, Y. S. Synthesis, Characterization and Gas Transport Properties of MOF-5 Membranes. *J. Memb. Sci.* **2011**, *382* (1–2), 82–90.

(4) Zhou, H.-C.; Long, J.R.; Yaghi. O.M. Introduction to Metal − Organic Frameworks. *Chem. Rev.* **2012**, *112* (2), 673–674.

(5) Kirchon, A.; Feng, L.; Drake, H. F.; Joseph, E. A.; Zhou, H. C. From Fundamentals to Applications: A Toolbox for Robust and Multifunctional MOF Materials. *Chem. Soc. Rev.* **2018**, *47* (23), 8611–8638.

(6) DeStefano, M. R.; Islamoglu, T.; Garibay, S. J.; Hupp, J. T.; Farha, O. K. Room-Temperature Synthesis of UiO-66 and Thermal Modulation of Densities of Defect Sites. *Chem. Mater.* **2017**, *29* (3), 1357–1361.

(7) Verma, P. K.; Huelsenbeck, L.; Nichols, A. W.; Islamoglu, T.; Heinrich, H.; Machan, C. W.; Giri, G. Controlling Polymorphism and Orientation of NU-901/NU-1000 Metal-Organic Framework Thin Films. *Chem. Mater.* **2020**, *32* (24), 10556–10565.

(8) Li, H.; Eddaoudi, M.; O'Keeffe, M.; Yaghi, O.M. Design and Synthesis of an Exceptionally Stable and Highly Porous Metal-Oragnic Framework. *Nature* **1999**, *402* (6759), 276–279.

(9) Yuan, S.; Feng, L.; Wang, K.; Pang, J.; Bosch, M.; Lollar, C.; Sun, Y.; Qin, J.; Yang, X.; Zhang, P.; Wang, Q.; Zou, L.; Zhang, Y.; Zhang, L.; Fang, Y.; Li, J.; Zhou, H. C. Stable Metal–Organic Frameworks: Design, Synthesis, and Applications. *Adv. Mater.* **2018**, *30* (37), 1–35.

(10) Li, H.; Wang, K.; Sun, Y.; Lollar, C. T.; Li, J.; Zhou, H. C. Recent Advances in Gas Storage and Separation Using Metal–Organic Frameworks. *Mater. Today* **2018**, *21* (2), 108–121.

(11) Mahmoud, E.; Ali, L.; Sayah, A. El; Alkhatib, S. A.; Abdulsalam, H.; Juma, M.; Al-Muhtaseb, A. H. Implementing Metal-Organic Frameworks for Natural Gas Storage. *Crystals* **2019**, *9* (8), 406.
(12) Fu, Z.; Xu, G. Crystalline, Highly Oriented MOF Thin Film: The Fabrication and Application. *Chem. Rec.* **2017**, *17* (5), 518–534.
(13) Kadhom, M.; Deng, B. Metal-Organic Frameworks (MOFs) in Water Filtration Membranes for Desalination and Other Applications. *Appl. Mater. Today* **2018**, *11*, 219–230.
(14) Ranocchiari, M.; Bokhoven, J. A. Van. Catalysis by Metal-Organic Frameworks: Fundamentals and Opportunities. *Phys. Chem. Chem. Phys.* **2011**, *13* (14), 6388–6396.
(15) Yang, D.; Gates, B. C. Catalysis by Metal Organic Frameworks: Perspective and Suggestions for Future Research. *ACS Catal.* **2019**, *9* (3), 1779–1798.
(16) Horcajada, P.; Serre, C.; Vallet-Regí, M.; Sebban, M.; Taulelle, F.; Férey, G. Metal–Organic Frameworks as Efficient Materials for Drug Delivery. *Angew. Chemie* **2006**, *118* (36), 6120–6124.
(17) Alezi, D.; Belmabkhout, Y.; Suyetin, M.; Bhatt, P. M.; Weseliński, L. J.; Solovyeva, V.; Adil, K.; Spanopoulos, I.; Trikalitis, P. N.; Emwas, A. H.; Eddaoudi, M. MOF Crystal Chemistry Paving the Way to Gas Storage Needs: Aluminum-Based Soc -MOF for CH_4, O_2, and CO_2 Storage. *J. Am. Chem. Soc.* **2015**, *137* (41), 13308–13318.
(18) Rosi, N. L.; Eckert, J.; Eddaoudi, M.; Vodak, D. T.; Kim, J.; O'Keeffe, M.; Yaghi, O. M. Hydrogen Storage in Microporous Metal-Organic Frameworks. *Science* **2003**, *300* (5622), 1127–1129.
(19) Lin, R. B.; Li, L.; Zhou, H. L.; Wu, H.; He, C.; Li, S.; Krishna, R.; Li, J.; Zhou, W.; Chen, B. Molecular Sieving of Ethylene from Ethane Using a Rigid Metal–Organic Framework. *Nat. Mater.* **2018**, *17* (12), 1128–1133.
(20) Sun, Y.; Zheng, L.; Yang, Y.; Qian, X.; Fu, T.; Li, X.; Yang, Z.; Yan, H.; Cui, C.; Tan, W. Metal–Organic Framework Nanocarriers for Drug Delivery in Biomedical Applications. *Nano-Micro Lett.* **2020**, *12* (1), 1–29.
(21) Chen, S.; Xu, X.; Gao, H.; Wang, J.; Li, A.; Zhang, X. Fine-Tuning the Metal Oxo Cluster Composition and Phase Structure of Ni/Ti Bimetallic MOFs for Efficient CO_2 Reduction. *J. Phys. Chem. C* **2021**, *125* (17), 9200–9209.
(22) Ding, R.; Zheng, W.; Yang, K.; Dai, Y.; Ruan, X.; Yan, X.; He, G. Amino-Functional ZIF-8 Nanocrystals by Microemulsion Based Mixed Linker Strategy and the Enhanced CO_2/N_2 Separation. *Sep. Purif. Technol.* **2020**, *236* (October 2019), 116209.
(23) Olorunyomi, J. F.; Geh, S. T.; Caruso, R. A.; Doherty, C. M. Metal-Organic Frameworks for Chemical Sensing Devices. *Mater. Horizons* **2021**, *8* (9), 2387–2419.
(24) Dutta, G.; Jana, A. K.; Natarajan, S. Chemical Fixation of CO_2 and Other Heterogeneous Catalytic Studies by Employing a Layered Cu-Porphyrin Prepared Through Single-Crystal to Single-Crystal Exchange of a Zn Analogue. *Chem. Asian J.* **2018**, *13* (1), 66–72.
(25) Gharib, M.; Esrafili, L.; Morsali, A.; Retailleau, P. Solvent-Assisted Ligand Exchange (SALE) for the Enhancement of Epoxide Ring-Opening Reaction Catalysis Based on Three Amide-Functionalized Metal-Organic Frameworks. *Dalt. Trans.* **2019**, *48* (24), 8803–8814.
(26) Guan, Y.; Li, Y.; Zhou, J.; Zhang, T.; Ding, J.; Xie, Z.; Wang, L. Defect Engineering of Nanoscale Hf-Based Metal-Organic Frameworks for Highly Efficient Iodine Capture. *Inorg. Chem.* **2021**, *60* (13), 9848–9856.
(27) Ali, S.; Zuhra, Z.; Abbas, Y.; Shu, Y.; Ahmad, M.; Wang, Z. Tailoring Defect Density in UiO-66 Frameworks for Enhanced Pb(II) Adsorption. *Langmuir* **2021**, *37* (46), 13602–13609.
(28) Vermoortele, F.; Bueken, B.; Le Bars, G.; Van De Voorde, B.; Vandichel, M.; Houthoofd, K.; Vimont, A.; Daturi, M.; Waroquier, M.; Van Speybroeck, V.; Kirschhock, C.; De Vos, D. E. Synthesis Modulation as a Tool to Increase the Catalytic Activity of Metal-Organic Frameworks: The Unique Case of UiO-66(Zr). *J. Am. Chem. Soc.* **2013**, *135* (31), 11465–11468.
(29) Ahrenholtz, S. R.; Epley, C. C.; Morris, A. J. Solvothermal Preparation of an Electrocatalytic Metalloporphyrin MOF Thin Film and Its Redox Hopping Charge-Transfer Mechanism. *J. Am. Chem. Soc.* **2014**, *136* (6), 2464–2472.
(30) Kung, C. W.; Audu, C. O.; Peters, A. W.; Noh, H.; Farha, O. K.; Hupp, J. T. Copper Nanoparticles Installed in Metal-Organic Framework Thin Films Are Electrocatalytically Competent for CO2 Reduction. *ACS Energy Lett.* **2017**, *2* (10), 2394–2401.
(31) Kim, K. J.; Lu, P.; Culp, J. T.; Ohodnicki, P. R. Metal-Organic Framework Thin Film Coated Optical Fiber Sensors: A Novel Waveguide-Based Chemical Sensing Platform. *ACS Sensors* **2018**, *3* (2), 386–394.

(32) Venna, S. R.; Carreon, M. A. Metal Organic Framework Membranes for Carbon Dioxide Separation. *Chem. Eng. Sci.* **2015**, *124*, 3–19.
(33) Wang, M.; Huang, H.; Ma, X.; Huang, C.; Peng, X. Copper Metal-Organic Framework Embedded Carboxymethyl Chitosan-g-Glutathione/Polyacrylamide Hydrogels for Killing Bacteria and Promoting Wound Healing. *Int. J. Biol. Macromol.* **2021**, *187*, 699–709.
(34) Bétard, A.; Fischer, R. A. Metal-Organic Framework Thin Films: From Fundamentals to Applications. *Chem. Rev.* **2012**, *112* (2), 1055–1083.
(35) Yuan, H.; Li, N.; Fan, W.; Cai, H.; Zhao, D. Metal-Organic Framework Based Gas Sensors. *Adv. Sci.* **2022**, *9* (6), 1–27.
(36) Koo, W.-T.; Jang, J.-S.; Kim, I.-D. Metal-Organic Frameworks for Chemiresistive Sensors. *Chem* **2019**, *5* (8), 1938–1963.
(37) Yoon, S. M.; Park, J. H.; Grzybowski, B. A. Large-Area, Freestanding MOF Films of Planar, Curvilinear, or Micropatterned Topographies. *Angew. Chem. Int. Ed.* **2017**, *56* (1), 127–132.
(38) Jung, S.; Huelsenbeck, L.; Hu, Q.; Robinson, S.; Giri, G. Conductive, Large-Area, and Continuous 7,7,8,8-Tetracyanoquinodimethane@HKUST-1 Thin Films Fabricated Using Solution Shearing. *ACS Appl. Mater. Interfaces* **2021**, *13* (8), 10202–10209.
(39) Velioglu, S.; Keskin, S. Simulation of H_2/CH_4 Mixture Permeation through MOF Membranes Using Non-Equilibrium Molecular Dynamics. *J. Mater. Chem. A* **2019**, *7* (5), 2301–2314.
(40) Gu, Z. G.; Zhang, J. Epitaxial Growth and Applications of Oriented Metal–Organic Framework Thin Films. *Coord. Chem. Rev.* **2019**, *378*, 513–532.
(41) Yang, G. L.; Jiang, X. L.; Xu, H.; Zhao, B. Applications of MOFs as Luminescent Sensors for Environmental Pollutants. *Small* **2021**, *17* (22), 1–19.
(42) Hod, I.; Sampson, M. D.; Deria, P.; Kubiak, C. P.; Farha, O. K.; Hupp, J. T. Fe-Porphyrin-Based Metal-Organic Framework Films as High-Surface Concentration, Heterogeneous Catalysts for Electrochemical Reduction of CO_2. *ACS Catal.* **2015**, *5* (11), 6302–6309.
(43) Miyamoto, M.; Kohmura, S.; Iwatsuka, H.; Oumi, Y.; Uemiya, S. In Situ Solvothermal Growth of Highly Oriented Zr-Based Metal Organic Framework UiO-66 Film with Monocrystalline Layer. *CrystEngComm* **2015**, *17* (18), 3422–3425.
(44) Zacher, D.; Baunemann, A.; Hermes, S.; Fischer, R. A. Deposition of Microcrystalline $[Cu_3(Btc)_2]$ and $[Zn_2(Bdc)_2(Dabco)]$ at Alumina and Silica Surfaces Modified with Patterned Self Assembled Organic Monolayers: Evidence of Surface Selective and Oriented Growth. *J. Mater. Chem.* **2007**, *17* (27), 2785–2792.
(45) McCarthy, M. C.; Varela-Guerrero, V.; Barnett, G. V.; Jeong, H. K. Synthesis of Zeolitic Imidazolate Framework Films and Membranes with Controlled Microstructures. *Langmuir* **2010**, *26* (18), 14636–14641.
(46) Brunckova, H.; Mudra, E.; Rocha, L.; Nassar, E.; Nascimento, W.; Kolev, H.; Kovalcikova, A.; Molcanova, Z.; Podobova, M.; Medvecky, L. Preparation and Characterization of Isostructural Lanthanide Eu/Gd/Tb Metal-Organic Framework Thin Films for Luminescent Applications. *Appl. Surf. Sci.* **2021**, *542*, 148731.
(47) Biemmi, E.; Scherb, C.; Bein, T. Oriented Growth of the Metal Organic Framework $Cu_3(BTC)_2(H_2O)_3 \cdot xH_2O$ Tunable with Functionalized Self-Assembled Monolayers. *J. Am. Chem. Soc.* **2007**, *129* (26), 8054–8055.
(48) Gassensmith, J. J.; Erne, P. M.; Paxton, W. F.; Valente, C.; Stoddart, J. F. Microcontact Click Printing for Templating Ultrathin Films of Metal - Organic Frameworks. *Langmuir* **2011**, *27* (4), 1341–1345.
(49) Shekhah, O.; Wang, H.; Zacher, D.; Fischer, R. A.; Wöll, C. Growth Mechanism of Metal-Organic Frameworks: Insights into the Nucleation by Employing a Step-by-Step Route. *Angew. Chem. Int. Ed.* **2009**, *48* (27), 5038–5041.
(50) Shekhah, O.; Wang, H.; Kowarik, S.; Schreiber, F.; Paulus, M.; Tolan, M.; Sternemann, C.; Evers, F.; Zacher, D.; Fischer, R.; Woll, C. Step-by-Step Route for the Synthesis of Metal Organic Frameworks. *J. Am. Chem. Soc.* **2007**, *129* (49), 15118–15119.
(51) Demessence, A.; Horcajada, P.; Serre, C.; Boissière, C.; Grosso, D.; Sanchez, C.; Férey, G. Elaboration and Properties of Hierarchically Structured Optical Thin Films of MIL-101(Cr). *Chem. Commun.* **2009**, *101* (46), 7149–7151.
(52) Demessence, A.; Boissière, C.; Grosso, D.; Horcajada, P.; Serre, C.; Férey, G.; Soler-Illia, G. J. A. A.; Sanchez, C. Adsorption Properties in High Optical Quality NanoZIF-8 Thin Films with Tunable

Thickness. *J. Mater. Chem.* **2010**, *20* (36), 7676–7681.
(53) Horcajada, P.; Serre, C.; Grosso, D.; Boissière, C.; Perruchas, S.; Sanchez, C.; Férey, G. Colloidal Route for Preparing Optical Thin Films of Nanoporous Metal-Organic Frameworks. *Adv. Mater.* **2009**, *21* (19), 1931–1935.
(54) Hod, I.; Bury, W.; Karlin, D.M.; Deria, P.; Kung, C.-W.; Katz, M.J.; So, M.; Klahr, B.; Jin, D.; Chung, Y.-W.; Odom, T.W.; Farha, O.K.; Hupp, J.T. Directed Growth of Electroactive Metal-Organic Framework Thin Films Using Electrophoretic Deposition. *Adv. Mater.* **2014**, *26*, 6295-6300.
(55) Han, H.; Yuan, X.; Zhang, Z.; Zhang, J. Preparation of a ZIF-67 Derived Thin Film Electrode via Electrophoretic Deposition for Efficient Electrocatalytic Oxidation of Vanillin. *Inorg. Chem.* **2019**, *58* (5), 3196–3202.
(56) Feng, J. F.; Yang, X.; Gao, S. Y.; Shi, J.; Cao, R. Facile and Rapid Growth of Nanostructured Ln-BTC Metal-Organic Framework Films by Electrophoretic Deposition for Explosives Sensing in Gas and Cr^{3+} Detection in Solution. *Langmuir* **2017**, *33* (50), 14238–14243.
(57) Chen, S.; Zhu, S.; Lin, Z.; Peng, J. Transforming Polymorphs via Meniscus-Assisted Solution-Shearing Conjugated Polymers for Organic Field-Effect Transistors. *ACS Nano* **2022**, *16* (7), 11194–11203.
(58) Giri, G.; Delongchamp, D. M.; Reinspach, J.; Fischer, D. A.; Richter, L. J.; Xu, J.; Benight, S.; Ayzner, A.; He, M.; Fang, L.; Xue, G.; Toney, M. F.; Bao, Z. Effect of Solution Shearing Method on Packing and Disorder of Organic Semiconductor Polymers. *Chem. Mater.* **2015**, *27* (7), 2350–2359.
(59) Worfolk, B. J.; Andrews, S. C.; Park, S.; Reinspach, J.; Liu, N.; Toney, M. F.; Mannsfeld, S. C. B.; Bao, Z. Ultrahigh Electrical Conductivity in Solution-Sheared Polymeric Transparent Films. *Proc. Natl. Acad. Sci. U. S. A.* **2015**, *112* (46), 14138–14143.
(60) Li, Z.; An, L.; Khuje, S.; Tan, J.; Hu, Y.; Huang, Y.; Petit, D.; Faghihi, D.; Yu, J.; Ren, S. Solution-Shearing of Dielectric Polymer with High Thermal Conductivity and Electric Insulation. *Sci. Adv.* **2021**, *7* (40), 1–8.
(61) Guthrie, S. M.; Smilgies, D. M.; Giri, G. Controlling Polymorphism in Pharmaceutical Compounds Using Solution Shearing. *Cryst. Growth Des.* **2018**, *18* (2), 602–606.
(62) Lee, J. C.; Kim, J. O.; Lee, H. J.; Shin, B.; Park, S. Meniscus-Guided Control of Supersaturation for the Crystallization of High Quality Metal Organic Framework Thin Films. *Chem. Mater.* **2019**, *31* (18), 7377–7385.
(63) Le Berre, M.; Chen, Y.; Baigl, D. From Convective Assembly to Landau - Levich Deposition of Multilayered Phospholipid Films of Controlled Thickness. *Langmuir* **2009**, *25* (5), 2554–2557.
(64) Kim, J. O.; Koo, W. T.; Kim, H.; Park, C.; Lee, T.; Hutomo, C. A.; Choi, S. Q.; Kim, D. S.; Kim, I. D.; Park, S. Large-Area Synthesis of Nanoscopic Catalyst-Decorated Conductive MOF Film Using Microfluidic-Based Solution Shearing. *Nat. Commun.* **2021**, *12* (1), 1–8.
(65) Lu, K.; Aung, T.; Guo, N.; Weichselbaum, R.; Lin, W. Nanoscale Metal–Organic Frameworks for Therapeutic, Imaging, and Sensing Applications. *Adv. Mater.* **2018**, *30* (37), 1–20.
(66) Abánades Lázaro, I.; Forgan, R. S. Application of Zirconium MOFs in Drug Delivery and Biomedicine. *Coord. Chem. Rev.* **2019**, *380*, 230–259.
(67) Sun, C. Y.; Qin, C.; Wang, X. L.; Su, Z. M. Metal-Organic Frameworks as Potential Drug Delivery Systems. *Expert Opin. Drug Deliv.* **2013**, *10* (1), 89–101.
(68) Annabi, N.; Nichol, J. W.; Zhong, X.; Ji, C.; Koshy, S.; Khademhosseini, A.; Dehghani, F. Controlling the Porosity and Microarchitecture of Hydrogels for Tissue Engineering. *Tissue Eng Part B Rev.* **2010**, *16* (4), 371–383.
(69) Sharpe, L. A.; Daily, A. M.; Horava, S. D.; Peppas, N. A. Therapeutic Applications of Hydrogels in Oral Drug Delivery. *Expert Opin. Drug Deliv.* **2014**, *11* (6), 901–915.
(70) Sornkamnerd, S.; Okajima, M. K.; Kaneko, T. Tough and Porous Hydrogels Prepared by Simple Lyophilization of LC Gels. *ACS Omega* **2017**, *2* (8), 5304–5314.
(71) Saghazadeh, S.; Rinoldi, C.; Schot, M.; Kashaf, S. S.; Sharifi, F.; Jalilian, E.; Nuutila, K.; Giatsidis, G.; Mostafalu, P.; Derakhshandeh, H.; Yue, K.; Swieszkowski, W.; Memic, A.; Tamayol, A.; Khademhosseini, A. Drug Delivery Systems and Materials for Wound Healing Applications. *Adv. Drug Deliv. Rev.* **2018**, *127*, 138–166.
(72) Zhang, Z.; Nguyen, H. T. H.; Miller, S. A.; Ploskonka, A. M.; Decoste, J. B.; Cohen, S. M. Polymer-Metal-Organic Frameworks (PolyMOFs) as Water Tolerant Materials for Selective Carbon Dioxide Separations. *J. Am. Chem. Soc.* **2016**, *138* (3), 920–925.

(73) Li, Y.; Zheng, Y.; Lai, X.; Chu, Y.; Chen, Y. Biocompatible Surface Modification of Nano-Scale Zeolitic Imidazolate Frameworks for Enhanced Drug Delivery. *RSC Adv.* **2018**, *8* (42), 23623–23628.
(74) Wu, Q.; Niu, M.; Chen, X.; Tan, L.; Fu, C.; Ren, X.; Ren, J.; Li, L.; Xu, K.; Zhong, H.; Meng, X. Biocompatible and Biodegradable Zeolitic Imidazolate Framework/Polydopamine Nanocarriers for Dual Stimulus Triggered Tumor Thermo-Chemotherapy. *Biomaterials* **2018**, *162*, 132–143.
(75) Gupta, V.; Mohiyuddin, S.; Sachdev, A.; Soni, P. K.; Gopinath, P.; Tyagi, S. PEG Functionalized Zirconium Dicarboxylate MOFs for Docetaxel Drug Delivery in Vitro. *J. Drug Deliv. Sci. Technol.* **2019**, *52*, 846–855.
(76) Liu, S.; Zhai, L.; Li, C.; Li, Y.; Guo, X.; Zhao, Y.; Wu, C. Exploring and Exploiting Dynamic Noncovalent Chemistry for Effective Surface Modification of Nanoscale Metal-Organic Frameworks. *ACS Appl. Mater. Interfaces* **2014**, *6* (8), 5404–5412.
(77) Yang, S.; Karve, V. V.; Justin, A.; Kochetygov, I.; Espín, J.; Asgari, M.; Trukhina, O.; Sun, D. T.; Peng, L.; Queen, W. L. Enhancing MOF Performance through the Introduction of Polymer Guests. *Coord. Chem. Rev.* **2021**, *427*, 213525.
(78) Abánades Lázaro, I.; Haddad, S.; Sacca, S.; Orellana-Tavra, C.; Fairen-Jimenez, D.; Forgan, R. S. Selective Surface PEGylation of UiO-66 Nanoparticles for Enhanced Stability, Cell Uptake, and pH-Responsive Drug Delivery. *Chem* **2017**, *2* (4), 561–578.
(79) Xie, K.; Fu, Q.; He, Y.; Kim, J.; Goh, S. J.; Nam, E.; Qiao, G. G.; Webley, P. A. Synthesis of Well Dispersed Polymer Grafted Metal-Organic Framework Nanoparticles. *Chem. Commun.* **2015**, *51* (85), 15566–15569.
(80) Garai, A.; Shepherd, W.; Huo, J.; Bradshaw, D. Biomineral-Inspired Growth of Metal-Organic Frameworks in Gelatin Hydrogel Matrices. *J. Mater. Chem. B* **2013**, *1* (30), 3678–3684.
(81) Zhang, Z.; Nguyen, H. T. H.; Miller, S. A.; Cohen, S. M. PolyMOFs: A Class of Interconvertible Polymer-Metal-Organic-Framework Hybrid Materials. *Angew. Chem. Int. Ed.* **2015**, *54* (21), 6152–6157.
(82) Gu, Y.; Huang, M.; Zhang, W.; Pearson, M. A.; Johnson, J. A. PolyMOF Nanoparticles: Dual Roles of a Multivalent PolyMOF Ligand in Size Control and Surface Functionalization. *Angew. Chemie* **2019**, *131* (46), 16829–16834.
(83) Ayala, S.; Zhang, Z.; Cohen, S. M. Hierarchical Structure and Porosity in UiO-66 PolyMOFs. *Chem. Commun.* **2017**, *53* (21), 3058–3061.
(84) Maan, O.; Song, P.; Chen, N.; Lu, Q. An In Situ Procedure for the Preparation of Zeolitic Imidazolate Framework-8 Polyacrylamide Hydrogel for Adsorption of Aqueous Pollutants. *Adv. Mater. Interfaces* **2019**, *6* (10), 1–9.
(85) Zhu, H.; Zhang, Q.; Zhu, S. Alginate Hydrogel: A Shapeable and Versatile Platform for in Situ Preparation of Metal-Organic Framework-Polymer Composites. *ACS Appl. Mater. Interfaces* **2016**, *8* (27), 17395–17401.
(86) Mahmoud, M. E.; Mohamed, A. K. Novel Derived Pectin Hydrogel from Mandarin Peel Based Metal-Organic Frameworks Composite for Enhanced Cr(Vl) and Pb(II) Ions Removal. *Int. J. Biol. Macromol.* **2020**, *164*, 920–931.
(87) Klein, S. E.; Sosa, J. D.; Castonguay, A. C.; Flores, W. I.; Zarzar, L. D.; Liu, Y. Green Synthesis of Zr-Based Metal-Organic Framework Hydrogel Composites and Their Enhanced Adsorptive Properties. *Inorg. Chem. Front.* **2020**, *7* (24), 4813–4821.
(88) Allegretto, J. A.; Giussi, J. M.; Moya, S. E.; Azzaroni, O.; Rafti, M. Synthesis and Characterization of Thermoresponsive ZIF-8@PNIPAm-: Co-MAA Microgel Composites with Enhanced Performance as an Adsorption/Release Platform. *RSC Adv.* **2020**, *10* (5), 2453–2461.
(89) Zhao, R.; Ma, T.; Zhao, S.; Rong, H.; Tian, Y.; Zhu, G. Uniform and Stable Immobilization of Metal-Organic Frameworks into Chitosan Matrix for Enhanced Tetracycline Removal from Water. *Chem. Eng. J.* **2020**, *382* (June 2019), 122893.
(90) Zhuang, Y.; Kong, Y.; Wang, X.; Shi, B. Novel One Step Preparation of a 3D Alginate Based MOF Hydrogel for Water Treatment. *New J. Chem.* **2019**, *43* (19), 7202–7208.

Chapter 2 Controlling Polymorphism and Orientation of NU-901/NU-1000 Metal–Organic Framework Thin Films Using Solvothermal Method

This chapter is published as:

Verma P. K.; Huelsenbeck, L.; Nichols, A. W.; Islamoglu, T.; Heinrich, H.; Machan, C. W.; Giri, G. Controlling Polymorphism and Orientation of NU-901/NU-1000 Metal-Organic Framework Thin Films. *Chem. Mater.* **2020**, 32 (24), 10556-10565.

The permission is received from American Chemical Society to use this paper as a Chapter in my thesis.

2.1 Abstract

NU-1000, a zirconium (Zr)-based MOF, is a promising candidate for heterogeneous catalysis, gas storage, electrocatalysis and drug-delivery applications due to its large pore size and mesoporous structure. However, the synthesis of NU-1000 may produce another polymorph NU-901, which has smaller average pore size and pore volume than NU-1000. Similarly, the presence of NU-1000 as a phase impurity in NU-901 crystallites is undesired. Although phase-pure NU-901 and NU-1000 have been successfully synthesized in bulk, multiple applications such as electrocatalysis and separation membranes require the formation of thin films. In this chapter, we utilize self-assembled monolayers and crystal engineering to control the polymorphism and orientation of NU-901/NU-1000 thin films. We report the fabrication of thin films of NU-901 and NU-1000 via a solvothermal method by functionalizing the substrate with carboxylic acid (–COOH) tail groups. This synthesis produces phase-pure hexagonal rod-shaped NU-1000 crystals and nearly phase-pure prolate-shaped NU-901 crystal as revealed by scanning-electron microscope (SEM), powder X-ray diffraction (PXRD), and nitrogen adsorption isotherm analyses. Furthermore, we control the orientation of NU-1000 crystallites on the FTO substrate by controlling the nucleation density of the MOFs on the substrate. We hypothesize that heating the functionalized substrate in a Zr-oxo cluster solution preceding solvothermal synthesis results in the coordination of Zr-oxo clusters to the (–COOH) groups of the substrate, which promotes a

higher nucleation density of NU-1000 on the substrate, resulting in the perpendicular growth of NU-1000 during crystal formation.

2.2 Introduction

Metal-organic frameworks (MOFs) are porous crystalline materials comprised of metal ions or metal ion clusters coordinated to organic linkers. MOFs have been synthesized with different pore sizes and exceptionally high specific surface areas,[1] making them a promising candidate for a wide range of applications, such as catalysis,[2] gas separation,[3] and sensing.[4] Of particular interest are MOFs containing hexazirconium (Zr_6) clusters due to their excellent thermal, chemical, and mechanical stabilities which stem from strong and numerous Zr-oxo coordination bonds.[5-8] The remarkable stability of Zr-based MOFs is ideal for electrocatalysis,[9,10] catalysis in aqueous and organic solvents,[11,12] and high temperature applications.[13,14] Since many applications require the formation of MOFs as thin films, constructing films of Zr-based MOFs is highly desired.

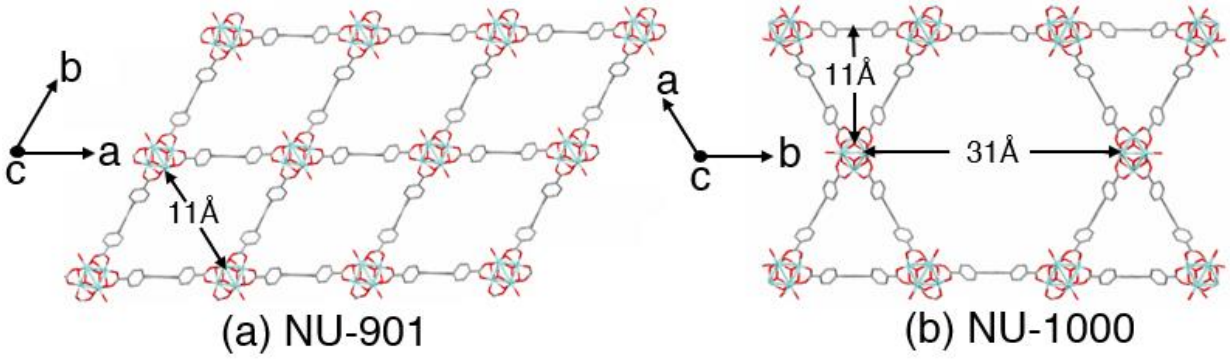

Figure 2.1. *Schematic representation of (a) NU-901 and (b) NU-1000 showing different pore sizes and crystallographic axes. Zr, O, and C atoms have been represented in blue, red, and gray respectively. H atoms have been omitted for clarity. Figures are generated using Mercury.[59] Reprinted with permission from ref. [60]. Copyright 2020 American Chemical Society.*

NU-1000, in particular, is a MOF with a large potential for thin-film applications. NU-1000 is constructed by coordinating Zr_6 [$Zr_6(\mu_3\text{-}OH)_4(\mu_3\text{-}O)_4(OH)_4(OH_2)_4$] nodes with tetratopic linker (H_4TBAPy, 1,3,6,8-tetrakis(p-benzoic acid)pyrene), and is a highly porous Zr-based MOF which contains 31 Å hexagonal pores and 11 Å triangular pores.[15] The mesoporous structure of NU-

1000 enables its use as a support material to create high surface area catalysts.[16-25] Furthermore, the 31 Å-wide mesopores of NU-1000 promotes the diffusion of large molecules (i.e. enzymes, proteins, drugs) inside NU-1000 for target applications.[26-28] However, NU-1000 displays a true polymorph known as NU-901, which is composed of the same stoichiometric ratio of Zr_6 nodes and H_4TBAPy linkers (**Figure 2.1a, b**). NU-901 possesses 11 Å-wide diamond-shaped micropores, allowing its use for gas adsorption.[29] The presence of multiple polymorphs in one sample affects the diffusion of gases and molecules as each polymorph possesses a distinct pore size, which can impact downstream applications.[30]

To optimize the formation of each polymorph for specific applications, phase-pure syntheses of NU-901 and NU-1000 have been accomplished. NU-901 has been synthesized using benzoic acid or 4-aminobenzoic acid as modulators.[29,31,32] Computational work has suggested that utilizing the modified version (substituting carbon-2 and carbon-7 of pyrene with bulky groups) of the H_4TBAPy linker,[33] could promote the phase-pure synthesis of the NU-1000 polymorph; experimentally, this has been demonstrated by using a longer modulator,[34] or a co-modulator,[28] to promote phase-pure synthesis. Thin films of NU-901 and NU-1000 have been fabricated by employing solvothermal growth (in-situ method) and electrophoretic deposition (ex-situ method).[9,10,31,35-39]

Controlling the orientation of anisotropic MOFs like NU-1000 is desirable because of the potential applications in optics,[40] adsorption,[41] and electrocatalysis.[42] The crystal orientation of NU-901 and NU-1000 has been controlled by adsorbing the organic linkers on the substrate before solvothermal growth.[31,42] However, the adsorption does not form covalent bonds between the linker and the substrate, which might yield weak adhesion of MOF nanoparticles to the substrate. Hence, a more suitable method is required to fabricate NU-901 and NU-1000 thin films and grow NU-901 and NU-1000 with different orientations, ideally on a wide variety of substrates.

Self-assembled monolayers (SAMs) can be utilized to control the crystal nucleation and growth kinetics of MOFs. For example, the nucleation and growth of MOF-5 was initiated by terminating a Au (111) surface with carboxyl (–COOH) groups.[43] Furthermore, thin films of HKUST-1 were obtained by terminating the substrate with carboxyl (–COOH) and hydroxyl (–OH) groups.[44,45] SAMs allow the flexibility in terminating the substrate surfaces with different functional groups. Previous reports have shown that selected SAM tail groups can enhance heterogeneous nucleation and growth of MOF thin films while anchoring them to the surface.[43,46] SAM-functionalization not only enhances the adhesion between MOF and the substrate by facilitating chemical bonding, but also allows orientation control of MOFs through changing surface interactions by changing the functional group ,[45] or by adjusting the density of functional groups.[47]

For our current work, the substrate of interest is fluorine-doped tin oxide (FTO), due to its utility in electrocatalysis. Similar metal oxides, such as indium tin oxide (ITO) have been modified using several phosphonic acids as SAMs.[48] In particular, 16-phosphonohexadecanoic acid (16-PHDA) (**Figure A2.1)** forms robust monolayers on the ITO surface via adsorption of phosphono groups to the surface hydroxyl (–OH) moieties of the ITO, resulting in a COOH-modified ITO surface.[48] Because the FTO surface also possesses surface hydroxyl groups, 16-PHDA was used to terminate FTO with (–COOH) groups to mimic the functionality of the H_4TBAPy linker (**Figure A2.1**). Additionally, a HKUST-1 thin film has been synthesized on the alumina substrate by terminating the surface with 16-PHDA.[49] We hypothesize that the availability of the same functional (–COOH) group on the surface as the linker will facilitate the coordination of Zr-oxo clusters to the surface groups,[43]; the subsequent attachment of the H_4TBAPy linkers and Zr-oxo clusters will result in a stronger attachment of the NU-901 or NU-1000 crystals on the FTO substrate.

Here, we report the syntheses of uniform thin films of nearly phase-pure NU-901 and phase-pure NU-1000 on FTO substrates modified by 16-PHDA (**Figure 2.2**). The thin film of 1000 crystals was monitored as a function of time and revealed no interconversion between the two

polymorphs. Furthermore, NU-1000 crystallites with two different orientations, where 1D hexagonal pores are parallel to the FTO substrate in one orientation (**Figure 2.2b**, parallel orientation) and perpendicular to the FTO substrate in the other orientation (**Figure 2.2c**, perpendicular orientation), were grown by controlling the nucleation density of the NU-1000 crystals on the substrate. The perpendicular growth of NU-1000 crystallites was promoted by heating the (–COOH) functionalized FTO substrate in a Zr-oxo cluster solution before solvothermal synthesis. We propose that the coordination of Zr-oxo clusters to the surface-bound carboxylic acid groups facilitates the growth of the MOF in a perpendicular direction to the FTO surface during crystal formation, due to a larger nucleation rate of NU-1000 crystals on the substrate. The ability to synthesize NU-1000 with different orientations provides an avenue to study the effect of NU-1000 orientation in multiple applications, such as catalysis, drug release, and separation.[41,42] In addition, we show that the orientation of NU-901 can also be controlled using the same technique, indicating that nucleation-based control of MOF orientation may be generalizable to multiple MOFs.

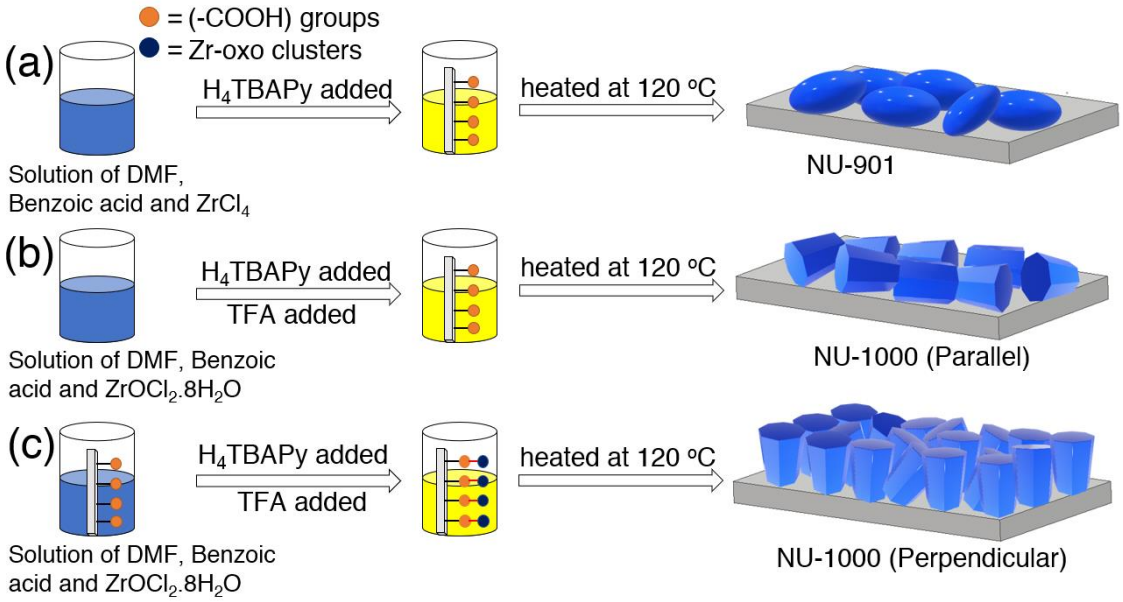

Figure 2.2. *Solvothermal synthesis procedures to obtain films of (a) NU-901, (b) NU-1000 with parallel orientation, and (c) NU-1000 with perpendicular orientation. Precursors are N,N-dimethyl-formamide (DMF), zirconium (IV) chloride ($ZrCl_4$), zirconyl chloride octahydrate ($ZrOCl_2.8H_2O$), benzoic acid (BA), 1,3,6,8- tetrakis (p-benzoic acid) pyrene (H_4TBAPy), and trifluoroacetic acid (TFA). Reprinted with permission from ref. [60]. Copyright 2020 American Chemical Society.*

2.3 Experimental Section

Materials and reagents. Fluorine-doped tin oxide (FTO) coated glass slides (7 Ω/sq, 10 cm x 10 cm x 0.23 cm), N,N-dimethyl formamide (DMF, 99.8%), 4-ethoxycarbonylphenylboronic acid (95%), trifluoroacetic acid (TFA, 99%), 4-aminobenzoic acid (99%), zirconium (IV) acetylacetonate ($Zr(acac)_4$, 97%), chloroform (99%), dioxane (99%), dichloromethane (99.8%), 16-phosphonohexadecanoic acid (97%), 1,3,6,8-tetrabromopyrene (97%), potassium phosphate tribasic (98%), potassium hydroxide (90%), and tetrakis(triphenylphosphine)palladium(0) (99%) were purchased from Sigma-Aldrich Inc. Methanol (99.9%), acetone (99.7%), benzoic acid (99.5%), and hydrogen chloride (HCl, 36.5 to 38%) were purchased from Thermo Fisher Chemical. Zirconium (IV) chloride ($ZrCl_4$, 99.5%) and zirconyl chloride octahydrate ($ZrOCl_2.8H_2O$, 99.9%) were purchased from Alfa Aesar Inc. All chemicals were used as received without further purification.

1,3,6,8-tetrakis (p-benzoic acid) pyrene (H_4TBAPy) Synthesis. H_4TBAPy linker was synthesized following previously published procedure.[15]

Pre-treatment of the FTO substrates. As received FTO glass was cut into small substrates (3 cm x 1 cm). The substrates were washed in deionized (DI) water (10 min), acetone (10 min), and methanol (20 min) using a bath sonication sequentially. After cleaning, the FTO substrates were rinsed with DI water and dried under an air stream. The cleaned FTO substrates were stored for further usage.

Preparation of self-assembled monolayers (SAMs). The process of the SAM formation on indium tin oxide (ITO) surface has been reported previously,[48] and the schematic has been shown in **Figure A2.1**. 5 mM solution of 16-PHDA in methanol was prepared and cleaned FTO substrates were immersed in the solution for 24 hours with FTO side facing upward to ensure the adsorption of 16-PHDA molecules on FTO surface. Afterward, the substrates were rinsed with methanol to remove weakly adsorbed molecules and annealed at 160 ºC for 24 hours inside the

glovebox to facilitate strong covalent bonding between the 16-PHDA molecules and FTO surface. In the end, the substrates were rinsed with DI water and dried under an air stream. All SAM modified FTO substrates were immediately utilized for NU-901/NU-1000 film synthesis.

NU-901 film synthesis procedure. Concentrations and synthesis conditions were adapted from ref. [31]. In a 20 mL glass vial, $ZrCl_4$ (35 mg, 0.15 mmol) and benzoic acid (1.35 g, 11.1 mmol) were dissolved in DMF (8 mL) and sonicated until a clear solution was obtained. The clear solution was placed inside a forced convection oven at 80 ºC for 2 hours. Then, the solution was cooled to room temperature and H_4TBAPy (20 mg, 0.03 mmol) was added. The mixture was sonicated for 20 minutes, which resulted in a yellow suspension. The functionalized FTO substrate was placed at an angle inside the yellow suspension with the FTO side facing upward. Afterward, the vial was placed inside the forced convection oven at 120 ºC for 24 hours. After 24 hours of reaction, the vial was cooled to room temperature and the substrate was taken out carefully. Then, the substrate was soaked in DMF for 24 hours followed by soaking in chloroform for 24 hours. In the end, the substrate was heated at 120 ºC for 24 hours at ambient pressure and stored for further characterization.

NU-1000 film synthesis procedure. Concentrations and synthesis conditions were adapted from ref. [28]. In a 20 mL glass vial, $ZrOCl_2.8H_2O$ (98 mg, 0.30 mmol) and benzoic acid (2.00 g, 16.4 mmol) were dissolved in DMF (8 mL) and sonicated until a clear solution was obtained. The clear solution was placed inside a forced convection oven at 100 ºC for 1 hour. After cooling the solution to room temperature, H_4TBAPy (40 mg, 0.06 mmol) and TFA (0.040 mL, 0.52 mmol) were added. The mixture was sonicated for 10 minutes, which resulted in a yellow suspension. The functionalized FTO substrate was placed at an angle inside the yellow suspension with the FTO side facing upward. After that, the vial was placed inside the forced convection oven at 120 ºC for 24 hours. After 24 hours of reaction, the vial was cooled to room temperature and the substrate was taken out carefully. Then, the substrate was soaked in DMF

for 24 hours followed by soaking in chloroform for 24 hours. Subsequently, the substrate was heated at 120 ºC for 24 hours at ambient pressure and stored for further characterization.

Experimental procedure for the time resolved study of NU-1000 film formation. Eight substrates of similar sizes (~ 1 cm x 1 cm) were cut from the FTO glass. The substrates were cleaned and functionalized according to the previously mentioned procedures. In a 100 mL glass vial, $ZrOCl_2.8H_2O$ (294 mg, 0.907 mmol) and benzoic acid (6.00 g, 49.2 mmol) were dissolved in DMF (24 mL) and sonicated until a clear solution was obtained. The clear solution was placed inside a forced convection oven at 100 ºC for 1 hour. After cooling the solution to room temperature, H_4TBAPy (120 mg, 0.18 mmol) and TFA (0.120 mL, 1.56 mmol) were added. The mixture was sonicated for 10 minutes, which resulted in a yellow suspension. Then, eight 20 mL glass vials were filled with 3 mL of yellow suspension. After that, the eight FTO substrates were put inside the vials with the FTO side facing upwards. All eight vials were kept inside the forced convection oven at 120 ºC simultaneously. Afterward, the vials were taken out at the intervals of 30 min, 1 h, 2 h, 3 h, 5 h, 8 h, 13 h, and 21 h. The substrates were soaked in DMF for 24 hours followed by the soaking in chloroform for 24 hours. In the end, the substrates were heated at 120 ºC for 24 hours at ambient pressure and stored for further characterization.

NU-1000 film synthesis with parallel orientation. Concentrations and synthesis conditions were adapted from ref. [28]. In a 20 mL glass vial, $ZrOCl_2.8H_2O$ (73.5 mg, 0.225 mmol) and benzoic acid (1.50 g, 12.3 mmol) were dissolved in DMF (6 mL) and sonicated until a clear solution was obtained. The clear solution was placed inside a forced convection oven at 100 ºC for 1 hour. After cooling the solution to room temperature, H_4TBAPy (20 mg, 0.03 mmol) and TFA (0.030 mL, 0.39 mmol) were added. The mixture was sonicated for 10 minutes, which resulted in a yellow suspension. The functionalized FTO substrate was placed perpendicular to the bottom surface of the vial using a PTFE holder inside the yellow suspension. After that, the vial was placed inside the forced convection oven at 120 ºC for 24 hours. After cooling the vial to the room temperature, the substrate was taken out and soaked in DMF for 24 hours followed by soaking in

chloroform for 24 hours. In the end, the substrate was heated at 120 ºC for 24 hours at ambient pressure and stored for further characterization.

NU-1000 film synthesis with perpendicular orientation. Concentrations and synthesis conditions were adapted from ref. [28]. In a 20 mL glass vial, $ZrOCl_2.8H_2O$ (73.5 mg, 0.225 mmol) and benzoic acid (1.50 g, 12.3 mmol) were dissolved in DMF (6 mL) and sonicated until a clear solution was obtained. The functionalized FTO was placed perpendicular to the bottom surface of the vial using a PTFE holder inside the clear solution and heated at 100 ºC for 1 hour inside a forced convection oven. After cooling the solution to room temperature, substrate was taken out and H_4TBAPy (20 mg, 0.03 mmol) and TFA (0.030 mL, 0.39 mmol) were added. The mixture was sonicated for 10 minutes, which resulted in a yellow suspension. The pre-heated FTO substrate (in a Zr-oxo cluster solution) was placed perpendicular to the bottom surface of the vial inside the yellow suspension. After that, the vial was placed inside the forced convection oven at 120 ºC for 24 hours. After cooling the vial to the room temperature, the substrate was taken out and soaked in DMF for 24 hours followed by soaking in chloroform for 24 hours. In the end, the substrate was heated at 120 ºC for 24 hours and stored for further characterization.

NU-901 film synthesis with parallel orientation: Concentrations and synthesis conditions were adapted from ref. [29]. In a 20 mL glass vial, $Zr(acac)_4$ (97 mg, 0.20 mmol) and 4-aminobenzoic acid (3.02 g, 22.0 mmol) were dissolved in DMF (8 mL) and sonicated until a clear solution was obtained. The clear solution was placed inside a forced convection oven at 80 ºC for 1 hour. After cooling the solution to room temperature, H_4TBAPy (20 mg, 0.03 mmol) was added. The mixture was sonicated for 10 minutes, which resulted in a yellow suspension. The functionalized FTO substrate was placed perpendicular to the bottom surface of the vial using a PTFE holder inside the yellow suspension. After that, the vial was placed inside the forced convection oven at 100 ºC for 24 hours. After cooling the vial to the room temperature, the substrate was taken out and soaked in DMF for 24 hours followed by soaking in chloroform for 24

hours. In the end, the substrate was heated at 120 ºC for 24 hours at ambient pressure and stored for further characterization.

NU-901 film synthesis with perpendicular orientation: Concentrations and synthesis conditions were adapted from ref. [29]. In a 20 mL glass vial, $Zr(acac)_4$ (97 mg, 0.20 mmol) and 4-aminobenzoic acid (3.02 g, 22.0 mmol) were dissolved in DMF (8 mL) and sonicated until a clear solution was obtained. The functionalized FTO was placed perpendicular to the bottom surface of the vial using a PTFE holder inside the clear solution and heated at 80 ºC for 20 hours inside a forced convection oven. After cooling the solution to room temperature, substrate was taken out and H_4TBAPy (20 mg, 0.03 mmol) was added. The mixture was sonicated for 10 minutes, which resulted in a yellow suspension. The pre-heated FTO substrate (in a Zr-oxo cluster solution) was placed perpendicular to the bottom surface of the vial inside the yellow suspension. After that, the vial was placed inside the forced convection oven at 100 ºC for 24 hours. After cooling the vial to the room temperature, the substrate was taken out and soaked in DMF for 24 hours followed by soaking in chloroform for 24 hours. In the end, the substrate was heated at 120 ºC for 24 hours at ambient pressure and stored for further characterization.

2.4 Result and discussion

Initially, clean FTO substrate was used to fabricate thin films of NU-901 and NU-1000. However, no formation of MOF nanoparticles was observed on the clean FTO substrate, and homogeneous nucleation in the solution occurred instead. Previous studies have shown that the adsorption of H_4TBAPy linkers on the FTO surface before synthesis facilitates the formation of NU-901 and NU-1000 crystals on the FTO.[9,31] The formation of NU-901 and NU-1000 was achieved by introducing a temperature gradient inside the vial using a gravity convection oven.[9,31] We attempted to replicate the synthesis using a forced convection oven but could not achieve the conditions conducive for the formation of NU-901 and NU-1000. Therefore, we functionalized the

FTO with (–COOH) groups to promote the formation of the NU-901 and NU-1000 crystals on the FTO surface.

The chemical composition of clean and SAM-modified FTO surfaces was analyzed using X-ray photoelectron spectroscopy (XPS) (**Figure 2.3**). The presence of tin (Sn) and oxygen (O) is expected on the clean FTO while the carbon (C) peak appears due to surface contamination during sample preparation. On the other hand, the SAM-modified FTO surface shows the attenuation of Sn peaks and amplification of O and C peaks, which are consistent with the adsorption of 16-PHDA molecules on the FTO surface. Additionally, the SAM-modified FTO surface has a phosphorous (P) peak which can be specifically attributed to the presence of 16-PHDA molecules. **Table A2.2** demonstrates the atomic percentage determined from the XPS spectra of the clean and SAM-modified FTO surfaces. Carbon composition rose significantly after the SAM-modification indicative of the long carbon chain in 16-PHDA. Therefore, the XPS analysis supports the successful modification of the FTO surface with 16-PHDA.

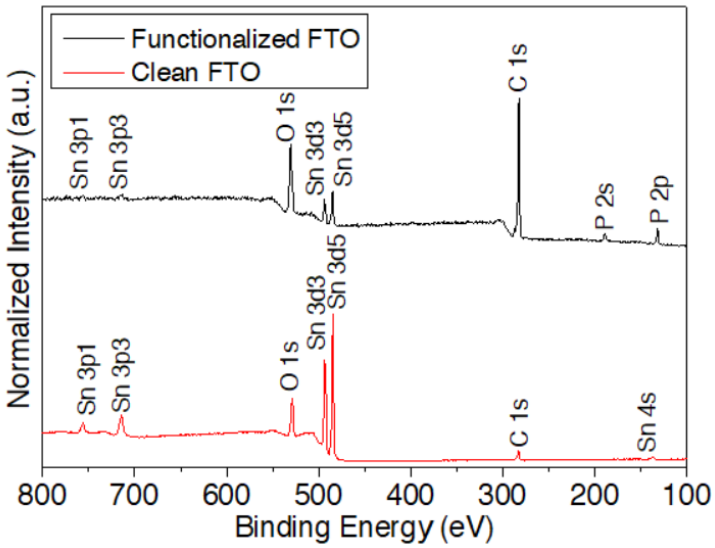

Figure 2.3. *XPS spectra of the clean (red) and 16-PHDA functionalized FTO (black). Each pattern is normalized to the most intense reflection. The presence of phosphorous atoms shows that the SAM modification is successful. Reprinted with permission from ref. [60]. Copyright 2020 American Chemical Society.*

When the SAM-modified FTO substrate was utilized in the synthesis of NU-901 (**Figure 2.2a**) and NU-1000 (**Figure 2.2b**) films, a yellow film formed on the FTO surface for both NU-901 and NU-1000 (**Figure A2.2**). Using a scanning electron microscope (SEM) (**Figure 2.4**), we observe that the NU-901 film is composed of prolate-shaped micro rods. The length of the major axis varies from 3 μm to 9 μm while the minor axis varies from 0.5 μm to 3 μm. Yang et al. reported the solvothermal synthesis of NU-901 thin film on the TiO_2 substrate containing 1 μm -10 μm long crystals of similar morphologies.[35] On the other hand, the NU-1000 film consists of hexagonal-shaped rods. The length of these hexagonal rods ranges from 3 μm to 10 μm while the width of the tip varies from 1 μm to 3 μm. Previous studies have demonstrated that the solvothermal growth of NU-1000 produced 1 μm-3 μm long hexagonal crystals.[9,42] Furthermore, all images display the continuous and complete film coverage of NU-901 and NU-1000 on the FTO substrate. The weight of the MOF on the FTO is estimated to be 0.60 ± 0.19 mg/cm^2 (**Table A2.1**).

The adhesion of the NU-901 and NU-1000 thin films was tested. Briefly, adhesive tape was attached to the FTO substrate and then peeled off (**Figure A2.3**, **A2.4**). NU-901 film showed exceptional adhesion to the FTO, whereas for NU-1000 loosely bound crystals were removed during the peeling process. Nonetheless, the NU-1000 film on the FTO surface is still uniform as seen through electron microscopy (**Figure A2.4e**), which shows that most of the crystals remain strongly attached to the FTO. Overall, the scotch tape study confirms the strong adhesion of the NU-901 and NU-1000 crystals to the FTO.

Although the mechanism of thin-film formation is still unclear, we hypothesize that the formation is likely to begin with the coordination of Zr-oxo clusters to the surface carboxylic acid groups (–COOH) followed by the coordination of H_4TBAPy linkers and Zr-oxo clusters.[43,45] To explore the chemical interaction between the MOF film and surface (–COOH) groups, the NU-1000 film (parallel) was sonicated for three minutes and analyzed using XPS (**Figure A2.5**). The sharp fluorine peak in both patterns is indicative of the coordination of the TFA molecules to the Zr-oxo clusters since the XPS of the clean FTO substrate does not show a fluorine peak (**Figure**

2.3). Sonication removes most of the MOF particles from the surface (**Figure A2.6**) which gives rise to tin peaks. Additionally, the relatively low amount of phosphorous (from the SAM) compared to other elements explains the absence of phosphorous peak. This experiment suggests that the coordination bond between the Zr-oxo clusters and the surface (–COOH) groups or the covalent bond between the FTO and the 16-PHDA molecules breaks during sonication, resulting in the detachment of the MOF from the surface.[50,51] In-situ Fourier-transform infrared spectroscopy (FTIR) and calorimetry techniques could be employed to gain further insights about the chemical interaction between MOF particles and surface (–COOH) groups in future studies.[52,53]

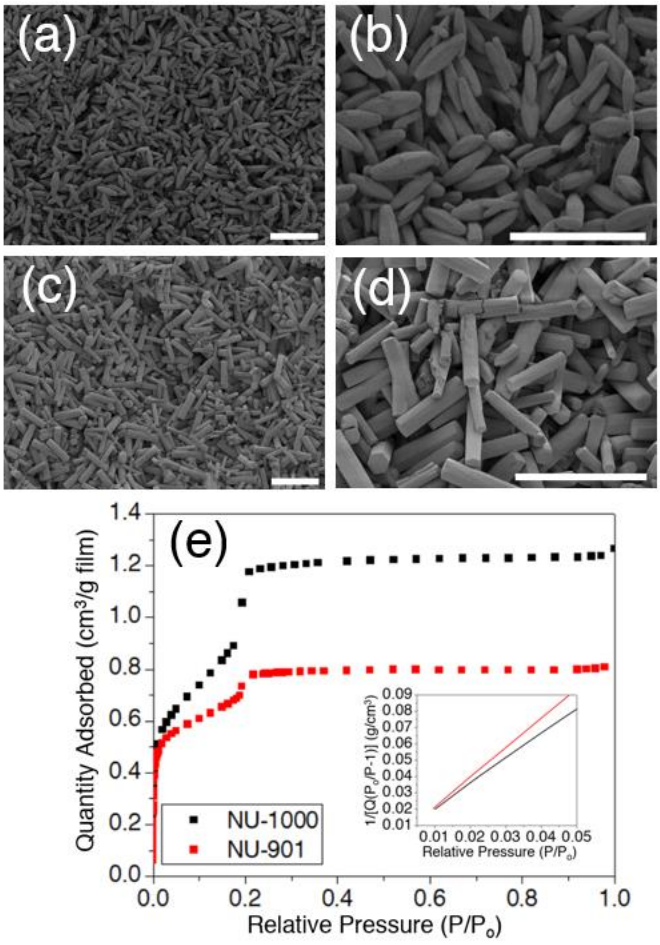

Figure 2.4. *SEM images of NU-901 thin film on the FTO at (a) low magnification (b) high magnification. SEM images of NU-1000 thin film on the FTO at (c) low magnification and (d) high magnification. Scale bar represents 20 μm in each image. (e) Nitrogen adsorption isotherm of the NU-901 and NU-1000 thin films on the FTO and the inset shows the liner plot for BET specific surface area calculation. Total weight (FTO and MOF) has been considered for nitrogen isotherm measurements. Reprinted with permission from ref. [60]. Copyright 2020 American Chemical Society.*

Nitrogen adsorption isotherms of NU-901 and NU-1000 films on FTO were collected to confirm the porosity and calculate the specific surface area of MOFs. The steep uptake at low pressure region is due to the micropores (type I isotherm) while the second sharp uptake in the isotherm near P/P_o of 0.2 can be attributed to the presence of mesopores (type IV isotherm).[54] However, since the NU-901 structure contains only micropores (11 Å) only a type I isotherm is expected for the corresponding thin film. Nonetheless, the NU-901 film shows a blend of type I and type IV isotherms (**Figure 2.4e**) which could be due to the presence of NU-1000 as an impurity in NU-901 crystallites, or due to missing node defects. However, Kung et al.,[31] achieved the phase-pure NU-901 thin film utilizing the same procedure outlined in the experimental section except they used a gravity convection oven. Nonetheless, other researchers have synthesized NU-901 crystallites containing NU-1000 as a phase impurity or missing node defects in the bulk.[29,55] Conversely, NU-1000 structure possesses micropores (11 Å) as well as mesopores (30 Å); therefore, a combination of type I and IV isotherms is anticipated for a NU-1000 thin film.[54] **Figure 2.4e** shows that the NU-1000 film isotherm is a combination of type I and type IV isotherms. From the linear regions ($0.01 \leq P/P_o \leq 0.05$), the calculated Brunauer-Emmett-Teller (BET) specific surface area of NU-901 and NU-1000 thin films are 1328 m^2/g and 1459 m^2/g respectively, which are lower than the reported powder samples.[28] The lower BET specific surface area of the films could be due to the presence of benzoic acid coordinated to Zr-oxo clusters. The adsorption isotherms were recorded with the substrate which resulted in a higher overall mass of the sample and hence very low nitrogen uptake were observed.

The pore size distributions of the NU-901 and NU-1000 thin films have been represented in **Figure A2.7**. NU-901 crystals possess 11 Å wide micropores inherent to its microporous structure and 25 Å wide mesopores because of NU-1000 as a phase impurity or missing node defects. On the other hand, NU-1000 crystals contain 13 Å wide micropores and 25 Å wide mesopores which is expected. The micropore width for both NU-901 and NU-1000 is comparable to the literature values.[28,29] However, the mesopores are smaller than the reported values possibly

due to the presence of modulators coordinated to the nodes. Other researchers have performed a HCl washing step to remove coordinated modulators before N_2 isotherm measurement which resulted in larger mesopores (30 Å).[28,29]

The crystallinity of the NU-901 and NU-1000 films were analyzed using out of plane powder X-ray diffraction (PXRD). **Figure 2.5a** represents a comparison of PXRD patterns of NU-901 and NU-1000 thin films with simulated NU-901 and NU-1000 PXRD patterns. As shown in **Figure 2.5a**, experimental patterns agree well with the simulated PXRD patterns which confirms the formation of NU-901 and NU-1000 crystals on the FTO. Furthermore, NU-901 crystals exhibit orientation along at least two different directions on the FTO as evidenced by the peaks at q = 0.37 $Å^{-1}$ and 0.54 $Å^{-1}$ which correspond to the diffraction from the (100) and $(1\bar{1}1)$ planes respectively. The presence of a peak at q = 0.19 $Å^{-1}$ in the experimental NU-901 pattern (marked by *) suggests that NU-1000 may be present as an impurity in NU-901. Conversely, peaks at q = 0.18 $Å^{-1}$ and 0.37 $Å^{-1}$ in the experimental NU-1000 PXRD pattern correspond to diffraction from the (100) and (200) planes, respectively, which suggests the preferential orientation of NU-1000 crystals along the [100] direction on the plane of the substrate.

The growth of NU-901 crystals along two different directions on functionalized FTO can be explained by looking at the supercell of NU-901 (**Figure 2.5b, c**). The (100) and the $(1\bar{1}1)$ planes cut through multiple Zr_6 nodes. As we expect the nodes to preferentially bind to the SAM, it is likely that these crystal planes are stabilized during crystal growth. This explains why NU-901 shows two preferred orientations on the FTO substrate. The preferential growth of NU-1000 crystals can be explained by observing the supercell of the NU-1000 MOF (**Figure 2.5d).** The (100) and (200) planes cutting through the supercell contain all the Zr_6 nodes. Since the coordination sites and linkers are partially oriented along [100] direction, the orientation of crystals along [100] or [200] direction can be anticipated due to alignment of the Zr_6 nodes on the SAM modified FTO substrate.

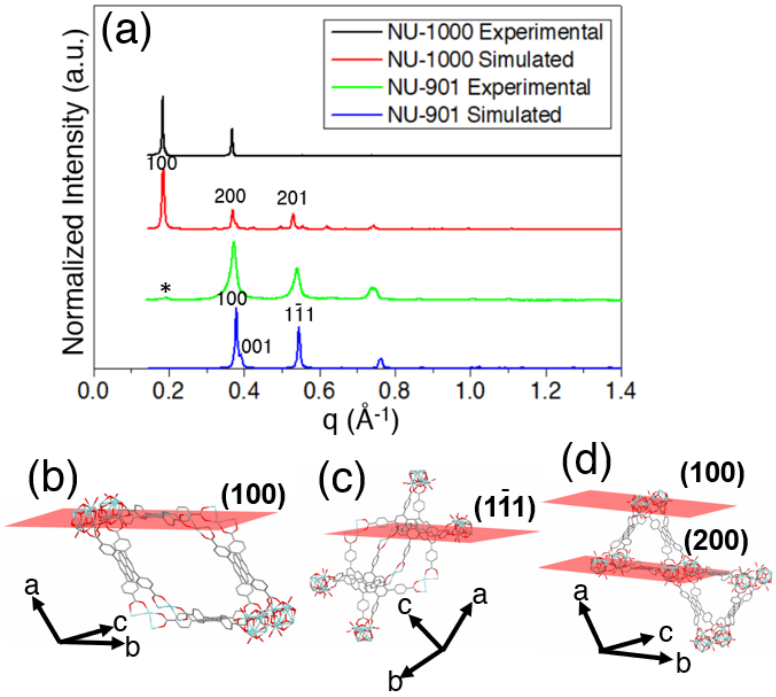

Figure 2.5. *(a) PXRD patterns of NU-901 and NU-1000 thin films on the FTO. The patterns are compared to simulated powder references. Each pattern is normalized to most intense reflection. The asterisk (*) represents the (100) peak of NU-1000 in NU-901 experimental pattern. (b) (100) and (c) (1$\bar{1}$1) planes cutting through the supercell of NU-901. (d) (100) and (200) planes cutting through the supercell of NU-1000. C, O and Zr atoms have been represented in grey, red and blue respectively. Hydrogen atoms have been omitted for clarity. Reprinted with permission from ref. [60]. Copyright 2020 American Chemical Society.*

To study the nucleation and growth of crystals, different synthesis times were investigated for the NU-1000 thin films. Films were characterized using SEM (**Figure 2.6b-i**) and XRD (**Figure 2.6j**). **Figure 2.6b** shows the formation of hexagonal rods within 10 minutes on the FTO substrate. Additionally, **Figure 2.6b** demonstrates the crystal formation occurs directly on the FTO surface which indicates heterogeneous nucleation. Furthermore, the nucleation continues after 10 min as observed by a greater number of crystals in **Figure 2.6c**, and **Figure 2.6d**. The crystals at longer synthesis times (8h, 13h, 21h) appear to be larger than the crystals at a shorter synthesis period (10 min, 30 min, 1h) which reveals that over the course of hours, the system shifts into crystal growth mode (**Figure A2.8**). The morphology of the NU-1000 crystals does not change with time. Therefore, it can be assumed that the phase transformation of NU-1000 to NU-901 does not take place during the synthesis. **Figure 2.6j** illustrates that all PXRD patterns are in good agreement with the simulated NU-1000 PXRD pattern.

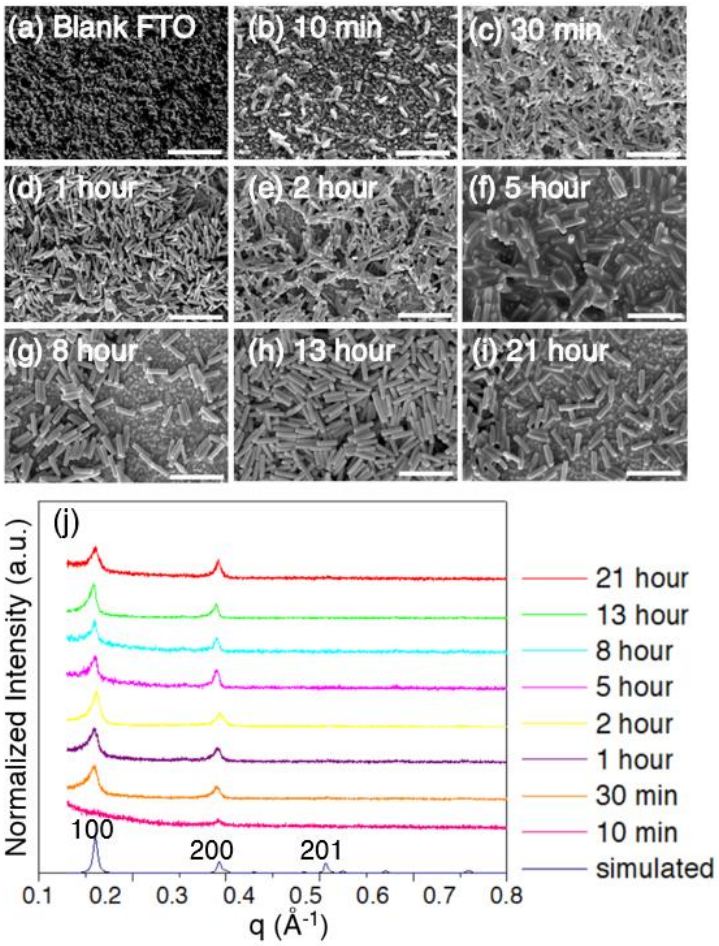

Figure 2.6. *SEM images of the (a) blank FTO and (b)-(i) NU-1000 thin film at different synthesis times. Scale bar represents 2 μm for each image. (j) PXRD patterns of NU-1000 film on FTO at different synthesis times. Each pattern is normalized to most intense reflection. Reprinted with permission from ref. [60]. Copyright 2020 American Chemical Society.*

We have also demonstrated that the orientation of NU-1000 on the FTO substrate can be controlled through the use of a SAM. In other reports, it has been shown that a high density of nucleation on the substrate surface can cause nanorods to be oriented perpendicular to the substrate.[56,57] Similarly, Liu et al. demonstrate the perpendicular orientation of ZIF-7 crystals on the alumina substrate during solvothermal growth due to the enhanced heterogeneous nucleation.[58] During crystal growth, a high density of nuclei on a surface limits nuclei growth parallel to the substrate because of the spatial hindrance provided by other nuclei. So, the growth

of nuclei is possible only in the upward direction. We hypothesize that the nucleation density of

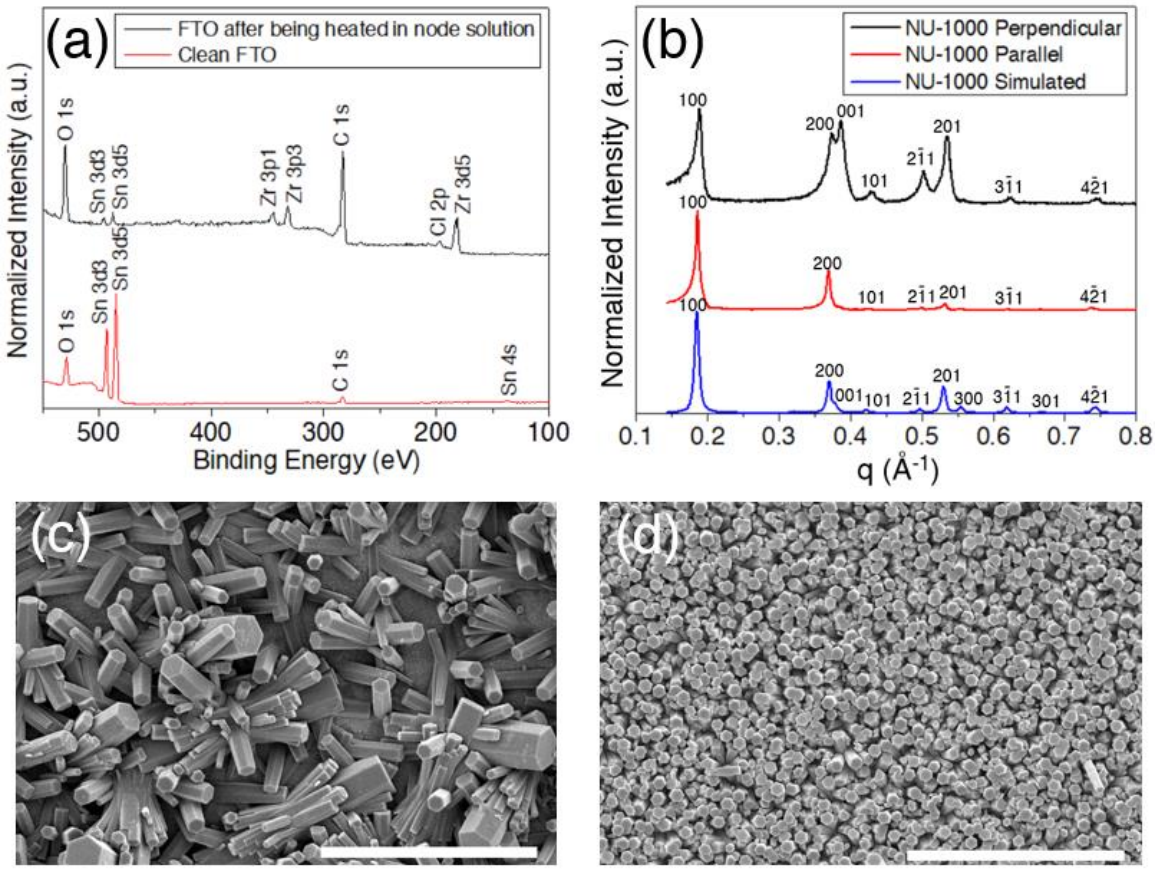

Figure 2.7. *(a) XPS spectra of the SAM functionalized FTO after being heated in the node solution. (b) PXRD patterns of the NU-1000 film on the FTO with parallel and perpendicular orientation. (c) Parallel and (d) perpendicular orientation of NU-1000 crystals on the FTO. Each pattern is normalized to most intense reflection in (a) and (b). Scale bar represents 20 μm in (c) and (d). Reprinted with permission from ref. [60]. Copyright 2020 American Chemical Society.*

the NU-1000 MOF can be controlled by increasing the density of Zr-oxo clusters on the functionalized FTO. Since 16-PHDA forms a dense layer of carboxyl group (–COOH) on the ITO surface,[48] it can be assumed that functionalized FTO also has a dense carboxyl group (–COOH) layer on the surface. As an alternative synthetic approach to that described above, pre-soaking the SAM-modified FTO substrate in the Zr-oxo cluster solution prior to solvothermal synthesis allows for a high density of Zr-oxo clusters to form on the substrate, resulting in a high nucleation density of NU-1000. This high nucleation density of NU-1000 leads to the growth of the long axis perpendicular to the FTO surface (**Figure 2.2c**), while lower number of nucleation sites can

facilitate the growth of NU-1000 crystals with the long axis lying parallel to the substrate (**Figure 2.2b**). Similarly, solvothermal synthesis with only the SAM-modified FTO and without presoaking in Zr-oxo clusters solution results in lower nucleation density of NU-1000. Therefore, the synthesis results in hexagonal rods lying (parallel orientation) on the surface with the hexagonal face perpendicular to the FTO substrate.

The presence of Zr-oxo clusters on the functionalized FTO after being heated in the Zr-oxo cluster solution for an hour was confirmed using XPS. **Figure 2.7a** compares the XPS spectra of clean and pre-heated functionalized FTO. The attenuation of Sn peaks, and amplification of O and C peaks are expected as explained earlier. The presence of zirconium (Zr) peak indicates that Zr-oxo clusters are formed in the node precursor solution and coordinated with the surface-immobilized (–COOH) groups.

NU-1000 films were then synthesized by heating the pre-treated FTO (in a Zr-oxo cluster solution) using the process as depicted in **Figure 2.2c**. Orientation of the films was characterized using SEM (**Figure 2.7c, d**). **Figure 2.7c** corresponds to the NU-1000 film obtained without presoaking the functionalized FTO in the Zr-oxo cluster solution, while Figure 7d represents the film synthesized on the FTO substrate presoaked in the Zr-oxo cluster solution. **Figure 2.7c** demonstrates that the long axis of the crystals is either parallel or inclined at an angle to the substrate (parallel orientation) while **Figure 2.7d** shows only the hexagonal faces of the crystals confirming that the long axis of the crystals is perpendicular to the substrate (perpendicular orientation). Additionally, the images reveal the excellent coverage of the film. The SEM data was further supported by PXRD analysis (**Figure 2.7b**). The PXRD pattern of the parallel orientation film (red) shows (100) and (200) peaks which confirms that (100) plane is parallel to the substrate; therefore, long axis of the crystals is parallel to the substrate. Conversely, the perpendicular orientation film's PXRD pattern (black) shows the (001) peak in addition to the (100) and (200) peaks confirming the hexagonal face is parallel to the substrate; hence, the long axis of the crystals is perpendicular to the substrate. Additionally, the intensities of (100) and (001) peaks in

parallel and perpendicular NU-1000 PXRD patterns are different. As a comparison, the intensity ratio of (001)/(100) peaks for parallel, perpendicular, and simulated NU-1000 PXRD patterns have been presented in **Table A2.3**. The ratio for the NU-1000 film with perpendicular orientation is higher than that of the isotropic ratio obtained from the powder simulation pattern, indicating anisotropic and perpendicular orientation. Conversely, the NU-1000 film with parallel orientation has a lower ratio than expected for an isotropic sample. The (001) peak of NU-1000 pattern (q ~ 0.388 $Å^{-1}$) overlaps with the (001) peak of NU-901 pattern (q ~ 0.39 $Å^{-1}$). However, Islamoglu el al. demonstrated that the addition of TFA suppressed the formation of NU-901.[28] Thus, the (001) appears due to the change in crystal orientation rather than phase impurity. Additionally, NU-901 thin films can be synthesized with parallel and perpendicular orientations using the same procedure (**Figure A2.9**, **A2.10**).

Goswami et al.,[42] have already shown the orientation control of NU-1000 on FTO using two different approaches. They achieved the parallel orientation of NU-1000 by depositing the pre-made NU-1000 crystals using electrophoretic deposition and obtained perpendicularly oriented NU-1000 crystals employing solvothermal synthesis. Unlike their approach, we controlled the orientation using only the solvothermal method. Additionally, they utilized the adsorption of H_4TBAPy linkers on the FTO to promote perpendicular growth, while we made use of the Zr-oxo clusters. Furthermore, our film consists of highly oriented NU-1000 crystals in the perpendicular direction as evident by a strong (001) peak in **Figure 2.7b**. One advantage of our method is its applicability to other anisotropic MOFs such as ZIF-L and MIL-88.

2.5 Conclusions

In summary, we demonstrated the successful synthesis of NU-901 and NU-1000 thin films on the FTO surface via a solvothermal method. NU-1000 thin films were fabricated by employing TFA as a co-modulator, which inhibited the formation of NU-901. Interestingly, NU-901 crystals are oriented along two different ([100] and [$1\bar{1}1$]) directions whereas NU-1000 crystals are

preferentially oriented along the [100] direction. The time-dependence growth study of NU-1000 film reveals the crystal formation on the surface within 10 min in addition to the nucleation and growth of crystals with time. We promoted the perpendicular growth of NU-1000 crystallites by coordinating the Zr-oxo clusters to the functionalized FTO before the film synthesis. Although we hypothesize that the availability of a dense layer of Zr-oxo clusters before the crystal formation is responsible for the perpendicular orientation of NU-1000, more in-depth analysis is required to prove the hypothesis. For instance, controlling the density of (–COOH) groups on the FTO surface followed by NU-1000 film synthesis could provide meaningful insights about the process. Additionally, a relationship between the crystal orientation and (–COOH) group density could be established to realize the specific orientation of NU-1000 for target applications. The method developed to alter the orientation of NU-1000 may pave the way for controlling the orientation of other anisotropic MOFs, which has implications in catalysis, separation, and drug delivery.

2.6 Appendix

MOF Weight on the FTO: FTO substrates were weighed before and after thin-film synthesis to determine the MOF weight on the FTO substrates. **Table S1** represents the experimental data for multiple thin films.

Table A2.1. Experimental data of MOF weight calculation for multiple MOF thin films. Reprinted with permission from ref. [60]. Copyright 2020 American Chemical Society.

FTO weight before (g)	FTO weight after (g)	MOF weight (mg)	MOF weight per unit area (mg/cm^2)
1.8219	1.8227	0.8	0.35
1.755	1.7561	1.1	0.48
1.7792	1.7805	1.3	0.76
1.7448	1.7463	1.5	0.88
1.7437	1.7446	0.9	0.53

Characterization Techniques

X-ray Photoelectron Spectroscopy (XPS): XPS spectra of clean and functionalized FTO were collected using PHI Versaprobe III XPS instrument equipped with monochromatic Al k-α X-rays (1486.6 eV) to probe sample surface. Survey scans from 800 eV to 100 eV were collected with a pass energy of 226 eV and a step size of 1.5 eV.

Scanning Electron Microscope (SEM): Images of the samples were obtained using a FEI quanta 650 field-emission secondary electron microscope. The samples were prepared by coating a 12Å layer of Au/Pd using Gatan 682 Precision Etching and Polishing System (PECS). The accelerating voltage of the primary beam was kept between 1 kV to 5 kV. All the sample were analyzed using spot size less than 4.

Powder X-ray Diffraction (PXRD): Diffraction patterns of NU-901 and NU-1000 thin film on FTO were collected using Empyrean multipurpose X-ray diffractometer. The source for X-rays consists of an X-ray tube with line focus Cu-anode (λ = 1.54 Å) and scattered waves from the samples are detected using GaliPIX3D detector. The source was operated at 45 kV and 40 mA and intensities from 2θ = 2º to 20º were recorded.

Brunauer, Emmett, and Teller (BET): BET specific surface area of the films was measured from nitrogen adsorption isotherm carried out on a Micromeritics ASAP2020 Surface Area and Porosity Analyzer. The substrate was broken into small pieces to accommodate the films in the analysis tube. Films were degassed at 120 ºC for 16 h under vacuum before the analysis. Data points from P/P_o = 0.01 to 0.05 were used to calculate the surface area. Pore size distribution of thin films were calculated using DFT model provided by MicroActive software (Micromeritics).

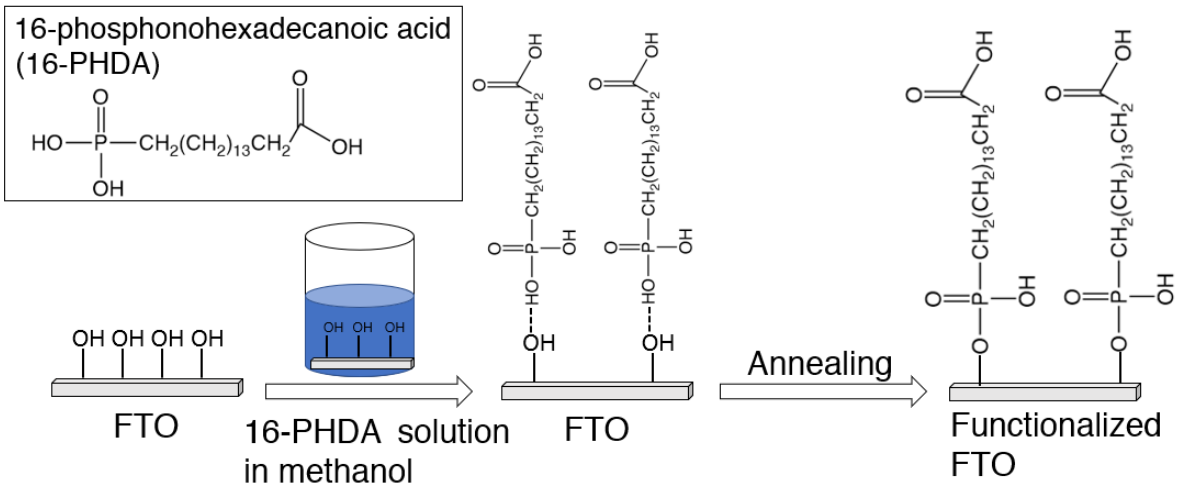

Figure A2.1. *Process of 16-phosphonohexadecanoic acid (16-PHDA) self-assembled monolayers formation on FTO surface. Reprinted with permission from ref. [60]. Copyright 2020 American Chemical Society.*

Table A2.2. **Atomic percentage of the clean and SAM functionalized FTO surface. Reprinted with permission from ref. [60]. Copyright 2020 American Chemical Society.**

Substrate	Sn 3d5 (%)	O 1s (%)	C 1s (%)	P 2p (%)
Clean FTO	33.6	41.3	25	0
functionalized FTO	2.0	23.5	68.2	6.3

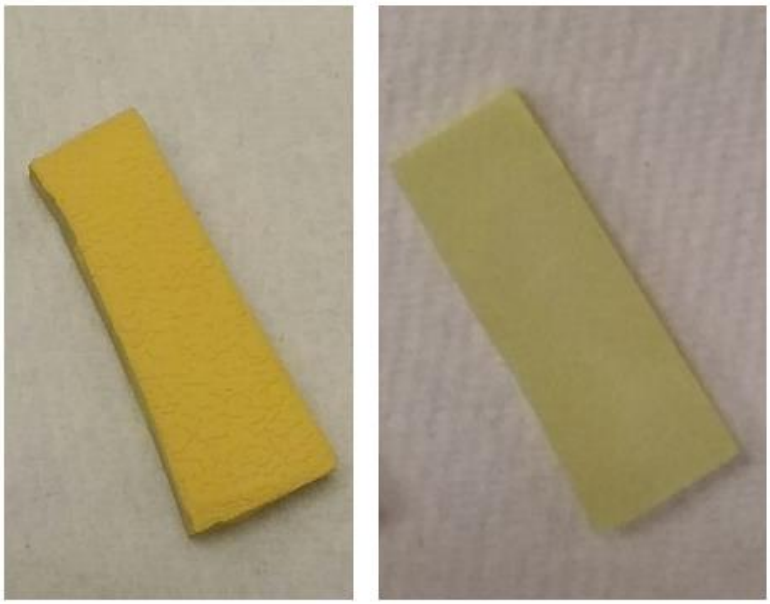

(a) NU-901 Film (b) NU-1000 Film

Figure A2.2. *Photo of (a) NU-901 thin film and (b) NU-1000 thin film on the FTO substrate. Reprinted with permission from ref. [60]. Copyright 2020 American Chemical Society.*

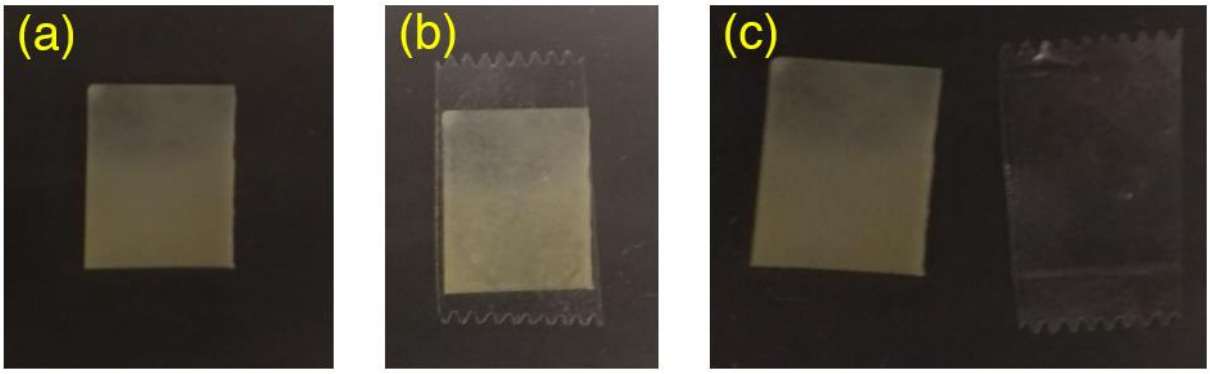

Figure A2.3. *Scotch tape adhesion testing of NU-901 thin film. Photo of (a) NU-901 thin film, (b) scotch tape attached to the film, and (c) NU-901 thin film after scotch tape being peeled off from the substrate. No transfer is observed by visual inspection. Reprinted with permission from ref. [60]. Copyright 2020 American Chemical Society.*

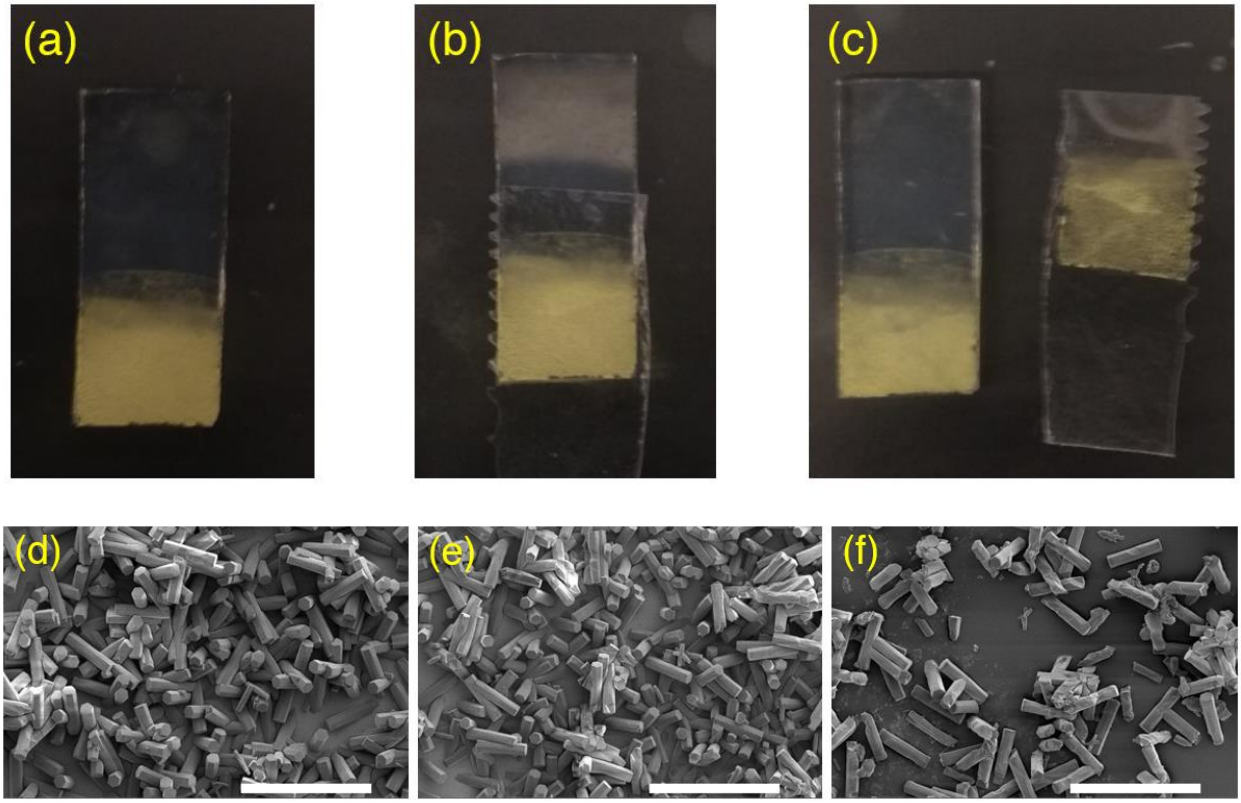

Figure A2.4. *Scotch tape adhesion testing of NU-1000 thin film. Photo of (a) NU-1000 thin film, (b) scotch tape attached to the film, (c) NU-1000 thin film after scotch tape being peeled off, (d) SEM of the NU-1000 thin film shown in (a), (e) SEM of the NU-1000 thin film shown in (c), and (f) SEM of the scotch tape shown in (c). Loosely bound particles transfer off the surface on the tape but film coverage remains largely intact after the peel test. The scale bar represents 50 μm. Reprinted with permission from ref. [60]. Copyright 2020 American Chemical Society.*

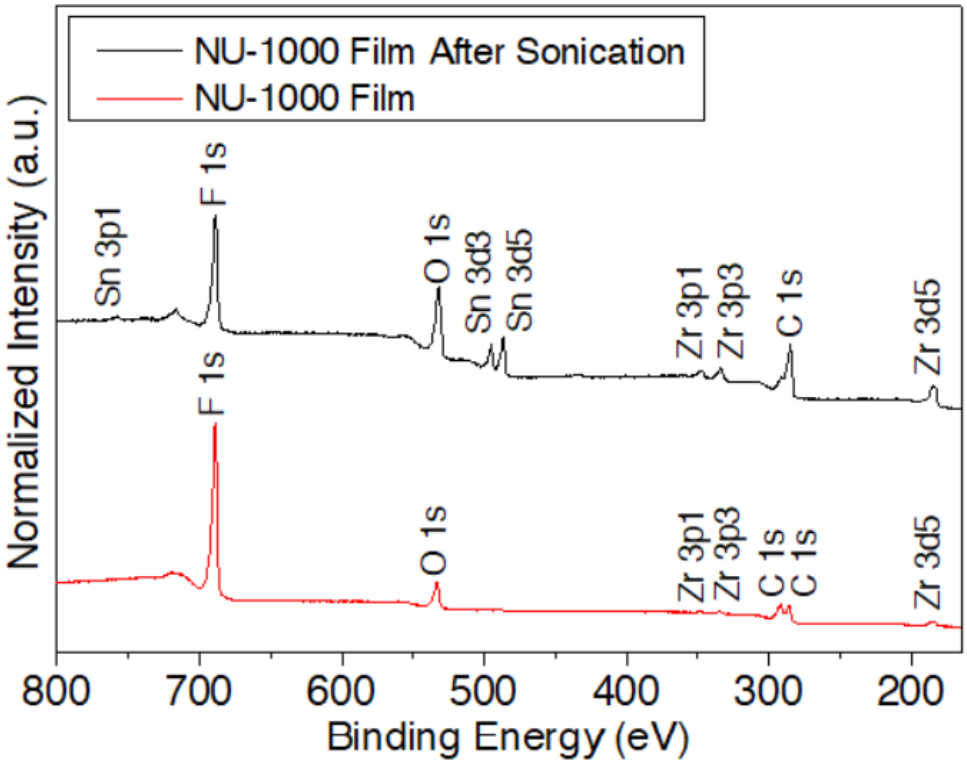

Figure A2.5. *XPS of NU-1000 thin film (red) and NU-1000 film after being sonicated for three minutes (black). Reprinted with permission from ref. [60]. Copyright 2020 American Chemical Society.*

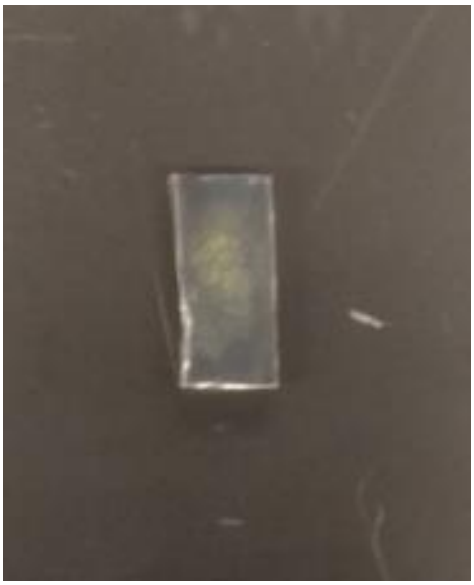

Figure A2.6. *Photo of NU-1000 thin film after being sonicated for three minutes. Reprinted with permission from ref. [60]. Copyright 2020 American Chemical Society.*

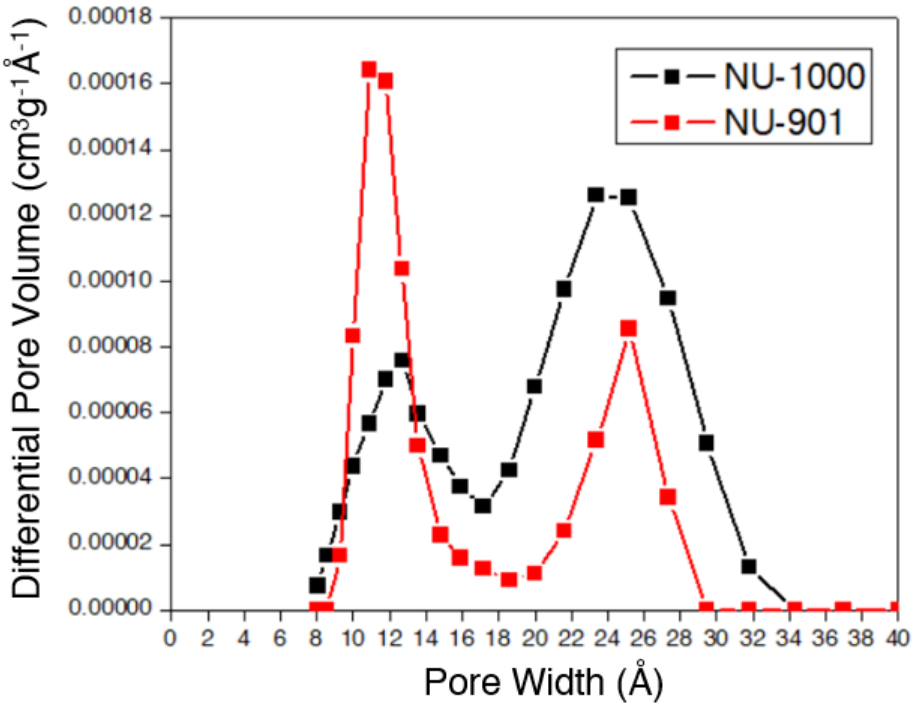

Figure A2.7. *Pore size distributions of NU-901 (red) and NU-1000 (black) thin films. Reprinted with permission from ref. [60]. Copyright 2020 American Chemical Society.*

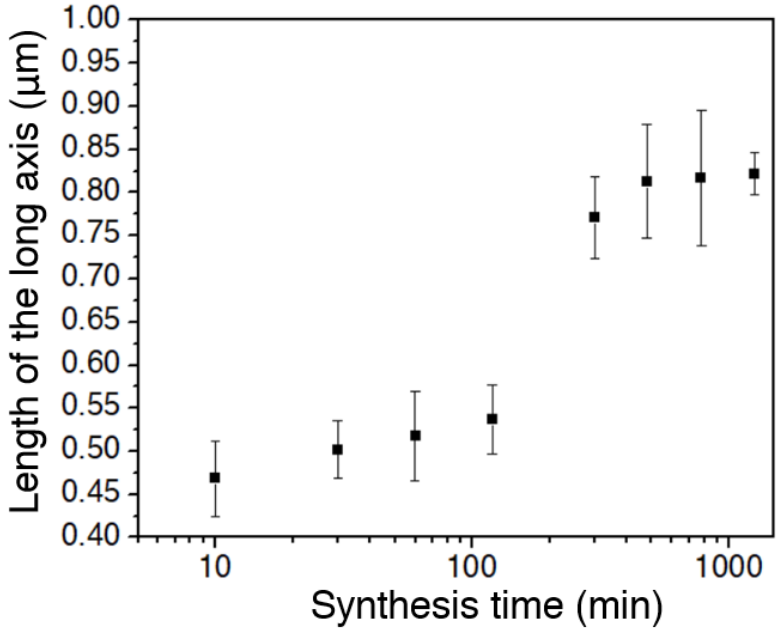

Figure A2.8. *Growth of NU-1000 crystal with time. Crystal growth becomes negligible after 8 hours indicating the consumption of almost all of the reactants within 8 hours. X-axis is in Log scale. Reprinted with permission from ref. [60]. Copyright 2020 American Chemical Society.*

Table A2.3. **Intensity ratio of (001)/(100) peaks for parallelly oriented NU-1000 crystals, perpendicularly oriented NU-1000 crystals, and simulated NU-1000 pattern. Reprinted with permission from ref. [60]. Copyright 2020 American Chemical Society.**

	NU-1000 Parallel	NU-1000 Perpendicular	NU-1000 Simulated
Intensity ratio of (001)/(100) peaks	0.05	0.89	0.10

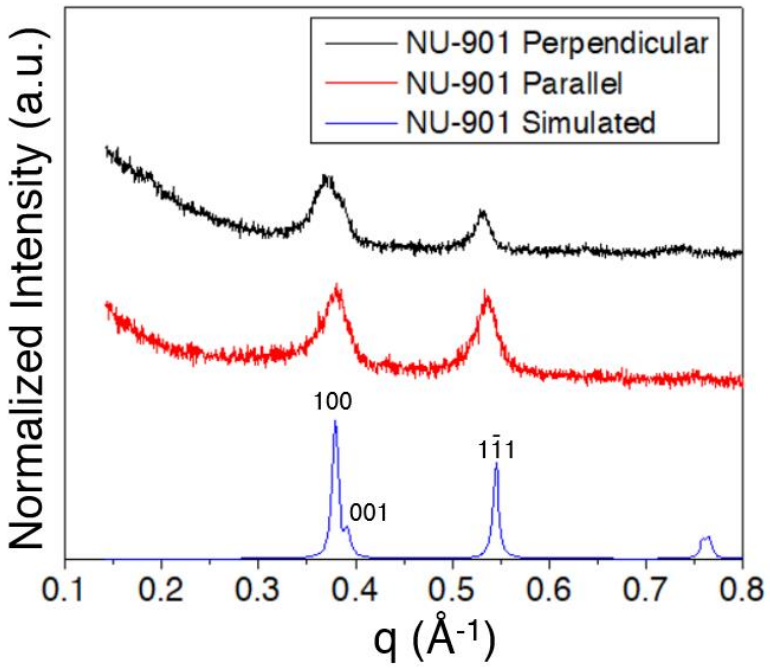

Figure A2.9. *PXRD patterns of the NU-901 film on the FTO with parallel and perpendicular orientation. Each pattern is normalized to most intense reflection. Reprinted with permission from ref. [60]. Copyright 2020 American Chemical Society.*

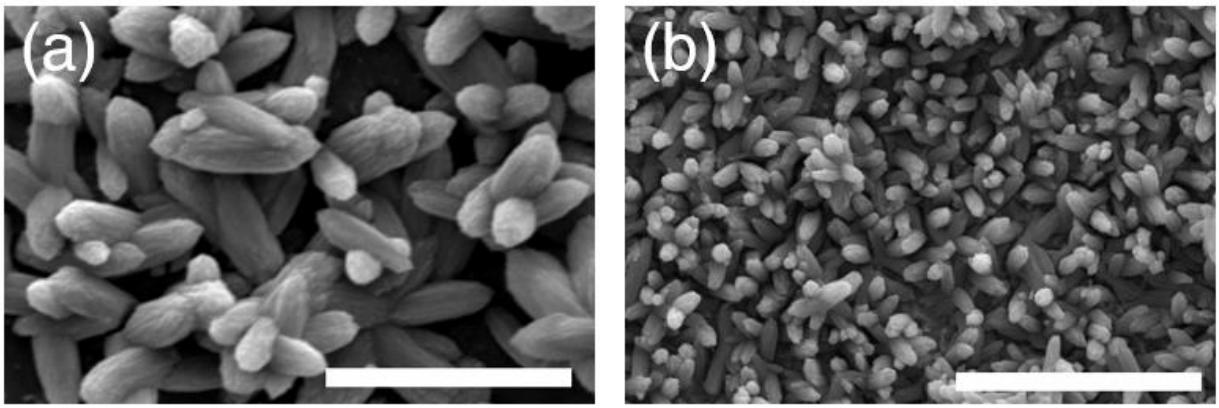

Figure A2.10. *SEM images of (a) parallel and (b) perpendicular oriented NU-901 crystal thin films on the FTO substrate. The scale bar represents 4 μm in each image. Reprinted with permission from ref. [60]. Copyright 2020 American Chemical Society.*

2.7 References

1. Furukawa, H.; Cordova, K. E.; O'Keeffe, M.; Yaghi, O. M. The chemistry and applications of metal-organic frameworks. *Science.* **2013**, 341 (6149), 1230444.
2. Herbst, A.; Khutia, A.; Janiak, C. Brønsted instead of lewis acidity in functionalized MIL-101Cr MOFs for efficient heterogeneous (nano-MOF) catalysis in the condensation reaction of aldehydes with alcohols. *Inorg. Chem.* **2014**, 53 (14), 7319−7333.
3. Lin, R.-B.; Xiang, S.; Xing, H.; Zhou, W.; Chen, B. Exploration of porous metal-organic frameworks for gas separation and purification. *Coord. Chem. Rev.* **2019**, 378, 87–103.
4. Zhang, Y.; Yuan, S.; Day, G.; Wang, X.; Yang, X.; Zhou, H.-C. Luminescent sensors based on metal-organic frameworks. *Coord. Chem. Rev.* **2018**, 354, 28-45.
5. Howarth, A. J.; Liu, Y.; Li, P.; Li, Z.; Wang, T. C.; Hupp, J. T.; Farha, O. K. Chemical, thermal and mechanical stabilities of metal− organic frameworks. *Nat. Rev. Mater.* **2016**, 1, 15018.
6. Faccioli, F.; Bauer, M.; Pedron, D.; Soraru, A.; Carraro, M.;` Gross, S. Hydrolytic stability and hydrogen peroxide activation of zirconium-based oxoclusters. *Eur. J. Inorg. Chem.* **2015**, 2015 (2), 210− 225.
7. Wong, Y. L.; Yee, K. K.; Hou, Y. L.; Li, J.; Wang, Z.; Zeller, M.; Hunter, A. D.; Xu, Z. Single-crystalline UiO-67-type porous network stable to boiling water, solvent loss, and oxidation. *Inorg. Chem.* **2018**, 57 (11), 6198−6201.
8. Wang, B.; Yang, Q.; Guo, C.; Sun, Y.; Xie, L.; Li, J. Stable Zr(IV)-based metal-organic frameworks with predesigned functionalized ligands for highly selective detection of Fe(III) ions in water. *ACS Appl. Mater. Interfaces* **2017**, 9 (11), 10286−10295.
9. Kung, C. W.; Mondloch, J. E.; Wang, T. C.; Bury, W.; Hoffeditz, W.; Klahr, B. M.; Klet, R. C.; Pellin, M. J.; Farha, O. K.; Hupp, J. T. Metal-organic framework thin films as platforms for atomic layer deposition of cobalt ions to enable electrocatalytic water oxidation. *ACS Appl. Mater. Interfaces* **2015**, 7 (51), 28223−28230.
10. Kung, C.-W.; Audu, C. O.; Peters, A. W.; Noh, H.; Farha, O. K.; Hupp, J. T. Copper nanoparticle installed in metal-organic framework thin films are electrocatalytically competent for CO_2 reduction. *ACS Energy Lett.* **2017**, 2 (10), 2394–2401.
11. Wang, Z.; Liu, H.; Wang, S.; Rao, Z.; Yang, Y. A luminescent terbium-succinate MOF thin film fabricated by electrodeposition for sensing of Cu^{2+} in aqueous environment. *Sens. Actuators B* **2015**, 220, 779−787.
12. Yu, Y.; Wang, Y.; Xu, H.; Lu, J.; Wang, H.; Li, D.; Dou, J.; Li, Y.; Wang, S. Dual-responsive luminescent sensors based on two Cd-MOFs: rare enhancement toward acac and quenching toward $Cr_2O_7^{2-}$. CrystEngComm **2020**, 22, 3759-3767.
13. Li, W.-J.; Liu, J.; Sun, Z.-H.; Liu, T.-F.; Lü, J.; Gao, S.-Y.; He, C.; Cao, R.; Luo, J.-H. Integration of metal-organic frameworks into an electrochemical dielectric thin film for electronic applications. *Nat. Commun.* **2016**, 7, 11830−11837.

14. Ramos-Fernandez, E. V.; Garcia-Domingos, M.; Juan-Alcaniz, J.; Gascon, J.; Kapteijn, F. MOFs meet monoliths: Hierarchical structuring metal organic framework catalysts *Appl. Catal., A* **2011**, 391, 261-267.
15. Wang, T. C.; Vermeulen, N. A.; Kim, I. S.; Martinson, A. B. F.; Stoddart, J. F.; Hupp, J. T.; Farha, O. K. Scalable synthesis and post-modification of a mesoporous metal-organic framework called NU-1000. *Nat. Protoc.* **2016**, 11, 149−162.
16. Thompson, A. B.; Pahls, D. R.; Bernales, V.; Gallington, L. C.; Malonzo, C. D.; Webber, T.; Tereniak, S. J.; Wang, T. C.; Desai, S. P.; Li, Z.; Kim, I. S.; Gagliardi, L.; Penn, R. L.; Chapman, K. W.; Stein, A.; Farha, O. K.; Hupp, J. T.; Martinson, A. B. F.; Lu, C. C. Installing heterobimetallic cobalt-aluminum single sites on a metal organic framework support. *Chem. Mater.* **2016**, 28 (18), 6753−6762.
17. Rimoldi, M.; Bernales, V.; Borycz, J.; Vjunov, A.; Gallington, L. C.; Platero-Prats, A. E.; Kim, I. S.; Fulton, J. L.; Martinson, A. B. F.; Lercher, J. A.; Chapman, K. W.; Cramer, C. J.; Gagliardi, L.; Hupp, J. T.; Farha, O. K. Atomic layer deposition in a metal−organic framework: Synthesis, characterization, and performance of a solid acid. *Chem. Mater.* **2017**, 29 (3), 1058−1068.
18. Li, Z.; Schweitzer, N. M.; League, A. B.; Bernales, V.; Peters, A. W.; Getsoian, A. B.; Wang, T. C.; Miller, J. T.; Vjunov, A.; Fulton, J. L.; Lercher, J. A.; Cramer, C. J.; Gagliardi, L.; Hupp, J. T.; Farha, O. K. Sintering-resistant single-site nickel catalyst supported by metal-organic framework. *J. Am. Chem. Soc.* **2016**, 138 (6), 1977−1982.
19. Peters, A. W.; Li, Z.; Farha, O. K.; Hupp, J. T. Atomically precise growth of catalytically active cobalt sulfide on flat surfaces and within a metal−organic framework via atomic layer deposition. *ACS Nano* **2015**, 9 (8), 8484−8490.
20. Desai, S. P.; Malonzo, C.; Webber, T.; Duan, J.; Thompson, A. B.; Tereniak, S. J.; DeStefano, M. R.; Buru, C. T.; Li, Z.; Penn, R. L.; Farha, O.; Hupp, J. T.; Stein, A.; Lu, C. Assembly of dicobalt and cobalt-aluminum oxide clusters on metal−organic framework and nanocast silica supports. *Faraday Discuss.* **2017**, 201, 287−302.
21. Atilgan, A.; Islamoglu, T.; Howarth, A. J.; Hupp, J. T.; Farha, O. K. Detoxification of a sulfur mustard simulant using a BODIPY-functionalized zirconium-based metal-organic framework. *ACS Appl. Mater. Interfaces* **2017**, 9 (29), 24555−24560.
22. Desai, S. P.; Ye, J.; Zheng, J.; Ferrandon, M. S.; Webber, T. E.; Platero-Prats, A. E.; Duan, J.; Garcia-Holley, P.; Camaioni, D. M.; Chapman, K. W.; Delferro, M.; Farha, O. K.; Fulton, J. L.; Gagliardi, L.; Lercher, J. A.; Penn, R. L.; Stein, A.; Lu, C. C. Well-defined rhodium-gallium catalytic sites in a metal-organic framework: promoter-controlled selectivity in alkyne semihydrogenation to E-alkenes. *J. Am. Chem. Soc.* **2018**, 140 (45), 15309−15318.
23. Peters, A. W.; Otake, K.; Platero-Prats, A. E.; Li, Z.; Destefano, M. R.; Chapman, K. W.; Farha, O. K.; Hupp, J. T. Site-directed synthesis of cobalt oxide clusters in a metal-organic framework. *ACS Appl. Mater. Interfaces* **2018**, 10 (17), 15073−15078.
24. Ahn, S.; Nauert, S. L.; Buru, C. T.; Rimoldi, M.; Choi, H.; Schweitzer, N. M.; Hupp, J. T.; Farha, O. K.; Notestein, J. M. Pushing the limits on metal-organic frameworks as a catalyst support: NU- 1000 supported tungsten catalysts for o-xylene isomerization and disproportionation. *J. Am. Chem. Soc.* **2018**, 140 (27), 8535−8543.
25. Goetjen, T. A.; Zhang, X.; Liu, J.; Hupp, J. T.; Farha, O. K. Metal-organic framework supported single site chromium (III) catalyst for ethylene oligomerization at low pressure and temperature. *ACS Sustainable Chem. Eng.* **2019**, 7 (2), 2553−2557.
26. Teplensky, M. H.; Fantham, M.; Li, P.; Wang, T. C.; Mehta, J. P.; Young, L. J.; Moghadam, P. Z.; Hupp, J. T.; Farha, O. K.; Kaminski, C. F.; Fairen-Jimenez. D. Temperature treatment of highly porous zirconium-containing metal-organic frameworks extends drug delivery release. *J. Am. Chem. Soc.* **2017**, 139 (22), 7522−7532.
27. P. Li, J. A. Modica, A. J. Howarth, E. Vargas, P. Z. Moghadam, R. Q. Snurr, M. Mrksich, J. T. Hupp and O. K. Farha, Toward design rules for enzyme immobilization in hierarchical mesoporous metal-organic frameworks. *Chem.* **2016**, 1 (1), 154–169.
28. Islamoglu, T.; Otake, K.-C.; Li, P.; Buru, C. T.; Peters, A. W.; Akpinar, I.; Garibay, S. J.; Farha, O. K. Revisiting the structural homogeneity of NU-1000, a Zr-based metal-organic framework. *CrystEngComm* **2018**, 20 (39), 5913-5918.

29. Garibay, S. J.; Iordanov, I.; Islamoglu, T.; DeCoste, J. B.; Farha, O. K. Synthesis and functionalization of phase-pure NU-901 for enhanced CO_2 adsorption: The influence of a zirconium salt and modulator on the topology and phase purity. *CrystEngComm* **2018**, 20 (44), 7066– 7070.
30. Taddei, M. When defects turn into virtues: The curious case of zirconium-based metal-organic frameworks. *Coord. Chem. Rev.* **2017**, 343, 1−24.
31. Kung, C.-W.; Wang, T. C.; Mondloch, J. E.; Fairen-Jimenez, D.; Gardner, D. M.; Bury, W.; Klingsporn, J. M.; Barnes, J. C.; Van Duyne, R.; Stoddart, J. F.; Wasielewski, M. R.; Farha, O. K.; Hupp, J. T. Metal-organic frameworks thin films composed of free-standing acicular nanorods exhibiting reversible electrochromism. *Chem. Mater.* **2013**, 25 (24), 5012-5017.
32. Deria, P.; Yu, J. R.; Smith, T.; Balaraman, R. P. Ground-state versus excited-state interchromophoric interaction: Topology dependent excimer contribution in metal-organic framework photophysics. *J. Am. Chem. Soc.* **2017**, 139 (16), 5973−5983.
33. Liu, W.-G.; Truhlar, D. G. Computational linker design for highly crystalline metal–organic framework NU-1000. *Chem. Mater.* **2017**, 29 (19), 8073–8081.
34. Webber, T. E.; Liu, W.-G.; Desai, S. P.; Lu, C. C.; Truhlar, D. G.; Penn, R. L. Role of a modulator in the synthesis of phase-pure NU-1000. *ACS Appl. Mater. Interfaces* **2017**, 9 (45), 39342−39346.
35. Yang, H.; Fei, H. A generic and facile strategy to fabricate metal-organic framework films on TiO_2 substrates for photocatalysis. *Dalton Trans.* **2017**, 46 (9), 2751-2755.
36. Hod, I.; Bury, W.; Karlin, D. M.; Deria, P.; Kung, C.-W.; Katz, M. J.; So, M.; Klahr, B.; Jin, D.; Chung, Y.-W.; Odom, T. W.; Farha, O. K.; Hupp, J. T. Directed growth of electroactive metal-organic framework thin films using electrophoretic deposition. *Adv. Mater.* **2014**, 26 (36), 6295−6300.
37. Hod, I.; Bury, W.; Gardner, D. M.; Deria, P.; Roznyatovskiy, V.; Wasielewski, M. R.; Farha, O. K.; Hupp, J. T. Bias-switchable permselectivity and redox catalytic activity of a ferrocene-functionalized, thin film metal-organic framework compound. *J. Phys. Chem. Lett.* **2015**, 6 (4), 586−591.
38. Hod, I.; Farha, O. K.; Hupp, J. T. Modulating the rate of charge transport in a metal-organic framework thin film using host:guest chemistry. *Chem. Commun.* **2016**, 52 (8), 1705-1708.
39. Buru, C. T.; Majewski, M. B.; Howarth, A. J.; Lavroff, R. H.; Kung, C.-W.; Peters, A. W.; Goswami, S.; Farha, O. K. Improving the efficiency of mustard gas simulant detoxification by tuning the singlet oxygen quantum yield in metal−organic frameworks and their corresponding thin films. *ACS Appl. Mater. Interfaces* **2018**, 10 (28), 23802−23806.
40. Falcaro, P.; Okada, K.; Hara, T.; Ikigaki, K.; Tokudome, Y.; Thornton, A. W.; Hill, A. J.; Williams, T.; Doonan, C.; Takahashi, M. Centimetre-scale micropore alignment in oriented polycrystalline metal-organic framework films via heteroepitaxial growth. *Nat. Mater.* **2017**, 16 (3), 342−348.
41. Yoon, S. M.; Park, J. H.; Grzybowski, B. A. Large-area, freestanding MOF films of planar, curvilinear, or micropatterned topographies. *Angew. Chem., Int. Ed.* **2017**, 56 (1), 127−132.
42. Goswami, S.; Hod, I.; Duan, J. D.; Kung, C.-W.; Rimoldi, M.; Malliakas, C. D.; Palmer, R. H.; Farha, O. K.; Hupp, J. T. Anisotropic redox conductivity within a metal−organic framework. *J. Am. Chem. Soc.* **2019**, 141 (44), 17696−17702.
43. Hermes, S.; Schroder, F.; Chelmowski, R.; Woll, C.; Fisher, R.A. Selective nucleation and growth of metal-organic framework thin films on Patterned COOH/CF3-terminated self-assembled monolayers on Au (111). *J. Am. Chem. Soc.* **2005**, 127 (40), 13744–13745.
44. Zacher, D.; Baunemann, A.; Hermes, S.; Fischer, R. A. Deposition of microcrystalline $[Cu_3(btc)_2]$ and $[Zn_2(bdc)_2(dabco)]$ at alumina and silica surfaces modified with patterned self assembled organic monolayers: Evidence of surface selective and oriented growth. *J. Mater. Chem.* **2007**, 17 (27), 2785-2792.
45. Biemmi, E.; Scherb, C.; Bein, T. Oriented growth of the metal organic framework $Cu_3(BTC)_2(H_2O)_3 \cdot xH_2O$ tunable with functionalized self-assembled monolayers *J. Am. Chem. Soc.* **2007**, 129 (26), 8054-8055.
46. Zhuang, J. L.; Friedel, J.; Terfort, A. The oriented and patterned growth of fluorescent metal-organic frameworks onto functionalized surfaces. *Beilstein J. Nanotechnol.* **2012**, 3, 570–578.
47. Liu, J.; Shekhah, O.; Stammer, X.; Arslan, H. K.; Liu, B.; Schü pbach, B.; Terfort, A.; Wöll, C. Deposition of metal–organic frameworks by liquid-phase epitaxy: The influence of substrate functional group density on film orientation. *Materials* **2012**, 5 (9), 1581–1592.

48. Chen, X.; Luais, E.; Darwish, N.; Ciampi, S.; Thordarson, P.; Gooding, J. J. Studies on the effect of solvents on self-assembled monolayers formed from organophosphonic acids on indium tin oxide. *Langmuir* **2012**, 28 (25), 9487−9495.
49. Vello, T.P.; Strauss, M.; Costa, C.A.R.; Correa, C.C.; Bufon, C.C.B. Deterministic control of surface mounted metal-organic control growth orientation on metallic and insulating surfaces. *Phys. Chem. Chem. Phys.* **2020**, 22 (10), 5839-5846.
50. Paulusse, J. M. J.; Sijbesma, R. P. Ultrasound in polymer chemistry: revival of an established technique. *J. Polym. Sci. A* **2006**, 44 (19), 5445–5453.
51. Mas-Balleste´, R.; Castillo, O.; Miguel, P. J. S.; Olea, D.; Go´mezHerrero, J.; Zamora, F. Towards molecular wires based on metal-organic frameworks. *Eur. J. Inorg. Chem.* **2009**, 2885-2896.
52. Yang, H. C.; Dermody, D. L.; Xu, C.; Ricco, A. J.; Crooks, R. M. Molecular interactions between organized, surface-confined monolayers and vapor-phase probe molecules. 8. Reactions between acid-terminated self-assembled monolayers and vapor-phase bases. *Langmuir* **1996**, 12 (3), 726-735.
53. Li, G.; Sun, H.; Xu, H.; Guo, X.; Wu, D. Probing the energetics of molecule−material interactions at interfaces and in nanopores. *J. Phys. Chem. C* **2017**, 121 (47), 26141−26154.
54. Ambroz, F.; Macdonald, T. J.; Martis, V.; Parkin, I. P. Evaluation of the BET theory for the characterization of meso and microporous MOFs. *Small Methods* **2018**, 2 (11), 1800173.
55. Noh, H.; Kung, C.-W.; Islamoglu, T.; Peters, A. W.; Liao, Y.; Li, P.; Garibay, S. J.; Zhang, X.; DeStefano, M. R.; Hupp, J. T.; Farha, O. K. Room temperature synthesis of an 8-connected Zr-based metal–organic framework for top-down nanoparticle encapsulation. *Chem. Mater.* **2018**, 30 (7), 2193-2197.
56. Jradi, K.; Bistac, S.; Schmitt, M.; Schmatulla, A.; Reiter, G. Enhancing nucleation and controlling crystal orientation by rubbing/scratching the surface of a thin polymer film. *Eur. Phys. J. E: Soft Matter Biol. Phys.* **2009**, 29, 383−389.
57. Tripathi, N.; Islam, S. S. A new approach for orientation-controlled growth of CNTs: an in-depth analysis on the role of oxygen plasma treatment to catalysts. *Appl. Nanosci.* **2017**, 7, 125−129.
58. Liu, Y.; Matsuda, R.; Kusaka, S.; Hori, A.; Ma, Y.; Kitagawa, S. Insights into inorganic buffer layer-assisted in situ fabrication of MOF films with controlled microstructure. *CrystEngComm* **2018**, 20 (43), 6995-7000.
59. Macrae, C. F.; Sovago, I.; Cottrell, S. J.; Galek, P. T. A.; McCabe, P.; Pidcock, E.; Platings, M.; Shields, G. P.; Stevens, J. S.; Towler, M.; Wood, P. A. Mercury 4.0: from visualization to analysis, design and prediction. *J. Appl. Crystallogr.* **2020**, *226*-235.
60. Verma P. K.; Huelsenbeck, L.; Nichols, A. W.; Islamoglu, T.; Heinrich, H.; Machan, C. W.; Giri, G. Controlling Polymorphism and Orientation of NU-901/NU-1000 Metal-Organic Framework Thin Films. *Chem. Mater.* **2020**, 32 (24), 10556-10565.

Chapter 3 Solution Shearing of Zirconium (Zr)-based Metal–Organic Frameworks NU-901 and MOF-525 Thin Films for Electrocatalytic Reduction Applications

3.1 Abstract

Solution shearing, a meniscus-guided coating process, can create large-area metal–organic framework (MOF) thin films rapidly, which can lead to the formation of uniform membranes for separations, or thin films for sensing and catalysis applications. Although previous work has shown that solution shearing can render MOF thin films, the examples have been limited to a few prototypical systems, such as HKUST-1, Cu-HHTP, and UiO-66. Here, we expand on the applicability of solution shearing by making large-area (~5 cm^2) thin films of NU-901, a zirconium (Zr)-based MOF. We study how the NU-901 thin film properties (i.e., crystallinity, surface coverage, and thickness) can be controlled as a function of substrate temperature and linker concentration. High surface coverage of NU-901 thin films (>90%) is achieved on a glass substrate for all conditions after one blade pass, while the crystallinity of NU-901 crystals increases with temperature, and decreases with linker concentration. On the other hand, the adjusted thickness of NU-901 films increases with both increasing temperature and linker concentration. We also extend the solution shearing technique to synthesize MOF-525 thin films on a transparent conductive oxide, which are useful for electrocatalysis. We show that Fe-metalated MOF-525 films can reduce CO_2 to CO, which has implications for CO_2 capture and utilization. The demonstration of thin film formation of NU-901 and MOF-525 using solution shearing on a wide range of substrates will be highly useful for implementing these MOFs in sensing and catalytic applications.

3.2 Introduction

Metal–organic frameworks (MOFs) are porous crystalline materials consisting of inorganic metal ions/clusters coordinated with organic linkers to form 3D structures with high specific surface area and tunable porosity.[1-6] Due to their tunable chemical composition, morphology, and porosity, MOFs have shown great potential in gas storage,[4,5] separation,[6–9] catalysis,[10,11] and sensing.[12–14] To enable these applications, the formation of MOF crystals as thin films on a support is of critical importance.[15–17] For instance, growing MOF crystals on a porous support is a prerequisite for membrane separation,[8,18,19] and growing MOF crystals on a conductive substrate,[20,21] is necessary for electrocatalysis. To implement MOF thin films in large scale applications, the synthesis process should be facile, low-cost, and easily scalable.[22]

There are various techniques to synthesize MOF thin films, including solvothermal growth,[23–25] layer-by-layer (LBL) growth,[17,26–28] and electrophoretic deposition,[29–31] among others. However, these techniques require hours or days to synthesize MOF thin films, and have limitations in terms of film uniformity and propensity to form cracks,[32] which is not feasible for commercial applications. Recently, solution shearing, a meniscus-guided coating technique, has been employed to grow large-area MOF thin films within minutes.[33–38] The facile fabrication technique and scalability make solution shearing well-suited for large-scale manufacturing applications.[39] Solution shearing utilizes solvent evaporation to induce the crystallization of MOFs. During solution shearing, the MOF precursor solution is sandwiched between a moving blade and a heated substrate (**Figure 3.1a**). A meniscus forms between the blade and the substrate, and heating promotes solvent evaporation from the meniscus leading to supersaturation and crystallization, and the blade movement allows for uniform MOF crystal formation on the substrate.[33] By controlling solution shearing parameters (e.g., substrate temperature, metal and linker concentration, solvent, and blade speed), thin film properties (crystallinity, thickness, crystal size, morphology, and surface coverage) can be precisely tuned.[33,35,36] Park et al. demonstrated the formation of large-area HKUST-1 MOF thin films using solution shearing with remarkable

control over crystal packing, film thickness, and crystal morphology.[33]. Furthermore, Giri et al. synthesized thin films of UiO-66, demonstrating the capabilities of solution shearing to deposit MOFs with complex metal clusters, such as the zirconium (Zr)-based MOFs.[35] However, only a handful of MOFs have been synthesized using solution shearing to prepare MOF thin films. To the best of our knowledge, no study has shown the formation of large pore Zr-based MOFs containing tetratopic linkers, such as the NU series of MOFs,[40,41] and PCN series of MOFs,[42,43] using solution shearing.

Herein, we employ NU-901 (**Figure 3.1b**), a Zr-based MOF consisting of Zr-oxo clusters and 4,4',4'',4'''-(pyrene-1,3,6,8-tetrayl) tetra benzoic acid (H_4TBAPy) linker.[40] We fabricated NU-901 thin films on glass substrates using solution shearing within 15 to 20 minutes over an area of 1 cm^2. We study the effects of temperature and organic linker concentration on the NU-901 thin film properties. We find that increasing the temperature enhances the coherence length of NU-901 crystals from 6.2 nm to 12.1 nm, indicating crystallinity increases with temperature. On the other hand, increasing the linker concentration decreases the coherence length of NU-901 crystals from 14.9 nm to 6.1 nm, suggesting crystallinity decreases with linker concentration. Additionally, we were able to create NU-901 films with thicknesses ranging from 500 nm to 3.5 microns by controlling the temperature and linker concentration. We furthermore expand the capability of solution shearing by preparing thin films of MOF-525 (**Figure 3.1c**), which is composed of Zr-oxo clusters and 4,4′,4″,4‴-(porphine-5,10,15,20-tetrayl) tetrakis(benzoic acid) (TCPP) linker.[44] The resultant MOF-525 films can be metalated with Fe, and these metalated films demonstrate comparable activity for the electrocatalytic reduction of CO_2 to the films prepared by Hod et al.,[44] using electrophoretic deposition. Overall, this study motivates the formation of tetratopic Zr-based MOF thin films using solution shearing for electrochemical applications.

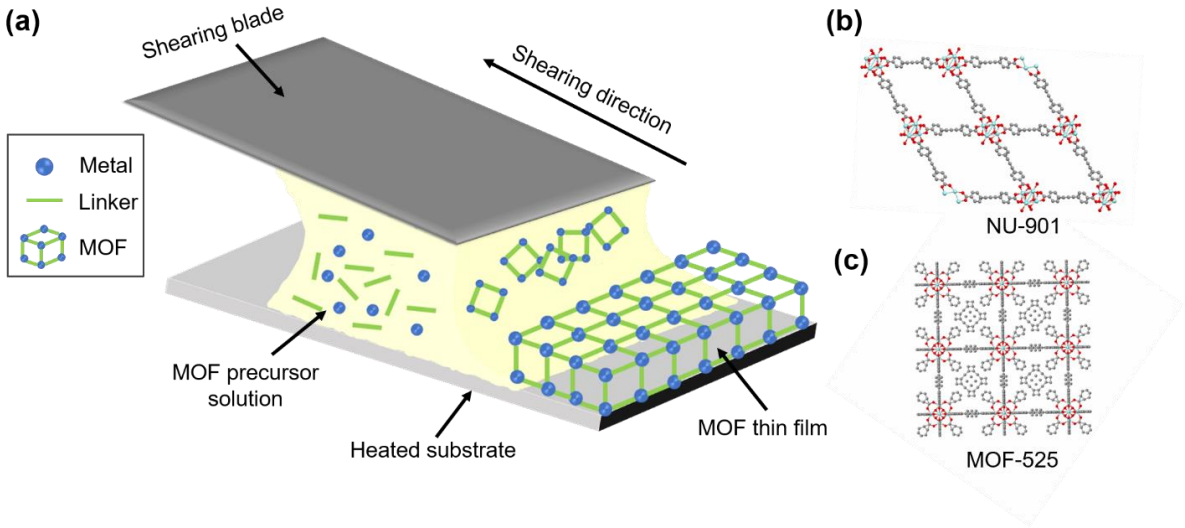

Figure 3.1. *(a) Schematic illustration of the solution shearing method used to synthesize large-area MOF thin films. The MOF precursor solution is injected between a moving blade and a heated substrate, and solvent evaporation induces MOF crystallization resulting in a MOF thin film. Crystal structures of (b) NU-901 and (c) MOF-525 MOFs. (Zr, O, and C have been represented in blue, red, and grey, respectively). Crystal structures were generated using Mercury.*[45]

3.3 Experimental Section

Materials

Indium tin oxide (ITO) coated glass slides (70-100 Ω/sq, 7.50 cm X 2.50 cm X 0.11 cm), zirconyl chloride octahydrate ($ZrOCl_2 \cdot 8H_2O$, 98%), formic acid (≥96%), dimethyl sulfoxide (DMSO, 99.9%), 4,4′,4″,4‴-(porphine-5,10,15,20-tetrayl)tetrakis(benzoic acid) (TCPP, dye content 75%), 4-ethoxycarbonylphenylboronic acid (95%), dioxane (99%), 1,3,6,8-tetrabromopyrene (97%), potassium phosphate tribasic (98%), tetrakis-(triphenylphosphine)palladium(0) (99%), potassium hydroxide (90%), chloroform (99%), dichloromethane (99.8%), trichloro(octadecyl)silane (OTS, ≥90%), and iron(III) chloride ($FeCl_3$, 97%) were purchased from Sigma-Aldrich and used as obtained. Methanol (99.9%), acetone (99.7%), hydrogen chloride (HCl, 36.5−38%), toluene (≥99.5%), isopropyl alcohol (IPA, ≥99.5%), and glass substrates (7.50 cm X 2.50 cm X 0.10 cm) were purchased from Fischer Scientific and used as obtained. Silicon wafers with a 285 nm silicon dioxide layer were purchased from University Wafer and used after cleaning. For all electrochemical experiments, HPLC-grade acetonitrile was obtained as anhydrous and air-free

from a PPT Glass Contour Solvent Purification System. Gas cylinders were obtained from Praxair (Ar as 5.0; CO_2 as 4.0). The electrolyte, tetrabutylammonium hexafluorophosphate ($TBAPF_6$), was obtained from AmBeed (97%) and recrystallized from ethanol prior to use. Ferrocene was obtained from TCI (>98%).

4,4',4'',4'''-(pyrene-1,3,6,8-tetrayl)tetra benzoic acid (H_4TBAPy) synthesis. H_4TBAPy synthesis procedure was adapted from a previous study.[20]

Substrate Preparation

Glass and ITO substrates were cut into small substrates (1.5 cm x 1 cm). The substrates were washed in acetone for 5 minutes using a bath sonication and dried at room temperature. The cleaned substrates were used for film deposition.

Blade fabrication

The method was adapted from the previous study.[35] Briefly, silicon wafer (10 cm x 10 cm) was cut into a small size (5 cm x 7 cm), and cleaned with toluene, acetone, IPA using a bath sonication and dried with air. The clean wafer was put into a UV/ozone cleaner for 15 min and transferred immediately to a 0.1 wt% OTS solution in toluene. The OTS solution was kept stirring at 50 °C for 16 h. Then, the wafer was dried at room temperature and sonicated in acetone for 5 min. Afterward, the hydrophobicity of the wafer was confirmed using deionized (DI) water and wafer was used as a coating blade.

NU-901 precursor synthesis

$ZrOCl_2 \cdot 8H_2O$ (24.5 mg) and formic acid (151 μL) were added to DMSO (2 mL) in a 20 mL glass vial and sonicated for 10 minutes. Afterward, the vial was heated at 100 °C for 1 h, and then the vial was cooled to room temperature. H_4TBAPy (10.0 mg) was added to this vial, followed by sonication for 10 minutes. The obtained precursor solution was used for solution shearing.

MOF-525 precursor synthesis

$ZrOCl_2 \cdot 8H_2O$ (24.5 mg) and formic acid (151 μL) were added to DMSO (2 mL) in a 20 mL glass vial and sonicated for 10 minutes. Afterward, the vial was heated at 100 °C for 1 h, and then the vial was cooled to room temperature. TCPP (24.0 mg) was added to this vial, followed by sonication for 10 minutes. The obtained precursor solution was used for solution shearing.

Synthesis of NU-901 and MOF-525 films

NU-901 and MOF-525 films were synthesized using a meniscus guided coating called solution shearing. The shearing blade was put on top of the substrate and the MOF precursor solution (~40 μL) was injected between a moving blade and a heated substrate. As the blade moved along the substrate, synthesis of MOF crystals occurred and MOF films were obtained.

NU-901 films were synthesized at two different temperatures (140 °C and 160 °C) and three different H_4TBAPy concentrations (3.4 mM, 6.8 mM, and 13.6 mM). The $ZrOCl_2 \cdot 8H_2O$ concentration was kept at 35.4 mM for all conditions.

MOF-525 films were synthesized at two different temperatures (160 °C and 180 °C). The $ZrOCl_2 \cdot 8H_2O$ concentration and TCPP concentration were kept at 35.4 mM and 14.1 mM, respectively.

Post-metalation of MOF-525 films

The metalation procedure was adapted from the previous study.[44] Briefly, $FeCl_3$ (10 mg) was dissolved in DMF (10 mL) in a 20 mL glass vial. The as synthesized MOF-525 film was immersed into the vial. The, the closed vial was heated at 80 °C for 24 h. Afterward, the vial was cooled to room temperature and the film was taken out from the vial. The film was washed with DMF and acetone for several times, and dried at 80 °C overnight.

Cyclic Voltammetry (CV)

All electroanalytical experiments were performed using a Metrohm Autolab PGSTAT302N potentiostat. The prepared MOF-525 samples on ITO glass served as the working electrodes. A leak-free non-aqueous silver/silver chloride pseudoreference electrodes were obtained from eDAQ, stored in a 3.4 M potassium chloride in the dark prior to use. Glassy carbon rods (⌀= 3 mm) were used as the counter electrodes. All CV experiments were performed in a scintillation vial (20 mL volume) as a single-chamber cell fitted with a modified cap with ports for all electrodes and a sparging needle. $TBAPF_6$ was purified by recrystallization from ethanol and dried in a vacuum oven before being stored in a desiccator. All data were referenced to an internal ferrocene standard (ferricenium/ferrocene (Fc^+/Fc) reduction potential under stated conditions). Ferrocene was purified by sublimation prior to use. All voltammograms were corrected for empirically determined internal resistance during data collection.

Controlled Potential Electrolysis (CPE)

CPE experiments were performed in a glass Pine Research Instrumentation H-cell with two compartments separated by a glass frit. A 75 mL stock solution of acetonitrile with 1.0 M $TBAPF_6$ was prepared for each bulk electrolysis experiment. Approximately 26 mL of the stock solution was added to each half of the H-cell. One side of the H-cell contained the ITO glass working electrode and 1.0 M trifluoroethanol. The other side of the H-cell contained approximately 0.075 M ferrocene as a sacrificial reductant along with a graphite rod counter electrode and a Ag/AgCl pseudoreference electrode. The electrolysis experiment was referenced by taking a CV of the ferrocene-containing solution. The H-cell was sealed with two septa that were connected by a piece of PTFE tubing which aided to maintain equal pressure between each half of the cell during the electrolysis. Before starting the electrolysis experiment, both sides of the H-cell were sparged with CO_2 for 20 minutes and the sealed cell was allowed to equilibrate for at least 1 hour.

The resistance between the two halves of the H-cell was measured using the *i*-interrupt procedure available in the NOVA software provided by Metrohm.

CPE Product Analysis

During CPE experiments, 1 mL GC injections of the headspace were periodically taken for the detection and quantification of any gaseous products produced. Note: in all cases the thin films did not produce sufficient gaseous products for quantification. After each CPE experiment, the total volume of solution was measured. The total volume of the sealed H-cell was also measured to account for the total headspace volume for accurate quantification of gaseous products. A calibration curve for CO and H_2 was used to quantify gaseous products produced during electrolysis experiments in the same manner as we previously reported.[55]

Analysis of gas phase products was done by sampling electrolysis headspace through syringe injections into an Agilent 7890B GC equipped with a specialty gas split column 5 Å mol sieve/Porabond Q column (15 m length; 0.320 mm diameter; 25.0 μm film) and thermal conductivity detector with He as a carrier gas. A calibration curve for CO and H_2 was made in the H-cell with an experimental setup containing identical volumes of MeCN with 1.0 M $TBAPF_6$ to those used during electrolysis. Known volumes of CO and H_2 were injected into the cell with stirring and 1 mL injections of the headspace were taken for GC injection after equilibration. The limit of detection (LOD) and limit of quantification (LOQ) for CO and H_2 in the GC were determined from nine consecutive injections at the lowest observable concentrations of each gaseous product respectively. The LOD was determined to be 3.83×10^{-6} moles and 4.47×10^{-6} moles for CO and H_2 respectively while the LOQ was determined to be 1.16×10^{-5} moles for CO and 1.35×10^{-5} moles for H_2.

Characterization

Grazing incidence X-ray diffraction (GIXD):

GIXD experiments were carried out at beamline 11-3 in Stanford Synchrotron Radiation Lightsource at SLAC National Accelerator Laboratory with a fixed beam energy (12.7 keV). The two-dimensional (2D) diffraction patterns were recorded using Rayonix MX225 CCD area detector with a sample-to-detector distance of 316 mm. Fast Azimuthal Integration (pyFAI) using python was performed to obtain 1D diffraction patterns from 2D GIXD images.

Powder X-ray diffraction (PXRD):

PXRD patterns were collected using Empyrean multipurpose X-ray diffractometer. X-rays were generated using an X-ray tube with line focus Cu-anode (λ = 1.54 Å) at 45 kV and 40 mA, and 1D patterns were recorded using GaliPIX3D detector.

Scanning electron microscopy (SEM):

SEM images were collected using a FEI quanta 650 field-emission secondary electron microscope. Before imaging, samples were coated with a layer of Au/Pd using a Cressington Sputter Coater. Primary beam's accelerating voltage was kept between 10 kV and 15 kV and samples were collected with a spot size of less than 5.

Energy dispersive X-ray spectroscopy (EDS):

EDS mapping and line scan data were collected using the same FEI quanta 650 field-emission secondary electron microscope. Before data collection, samples were coated with a layer of Au/Pd using a Cressington Sputter Coater. Primary beam's accelerating voltage was kept at 15 kV and samples were collected with a spot size of 4.5.

Profilometer

The thickness of each film was measured using a Bruker DektakXT Stylus Profilometer. Before measuring, a narrow passage of material was removed from the middle of a film using a razor blade, exposing the bare substrate. Using a scan speed of 10 μ/s with a stylus force of 1 mg, a length of 600 μm of film and 400 μm of bare substrate was measured. As the stylus moves across the sample the average height difference between the top of the film and the bottom of the substrate was measured.

3.4 Results and Discussion

Table 3.1. Solution shearing parameters used to make NU-901 thin films and their effects on thin film properties (for all conditions, solvent is DMSO, $ZrOCl_2.8H_2O$ concentration is 35.4 mM, formic acid concentration is 1.9 M and blade speed is 0.03 mm/s)

H_4TBAPy linker concentration (mM)	Temperature (°C)	Coverage	Thickness (μm)	Adjusted thickness (μm)	Coherence length (nm)
6.8	140	0.99	0.47±0.07	0.47±0.07	6.2
6.8	160	0.90	1.66±0.21	1.50±0.19	12.1
3.4	160	0.98	0.49±0.05	0.48±0.05	14.9
13.6	160	0.94	3.71±0.86	3.49±0.81	6.1

To determine the temperature at which solvent evaporation results in NU-901 crystal formation, we drop casted the NU-901 precursor solution on a glass substrate at different

temperatures (140 °C and 160 °C), where rapid DMSO evaporation results in enhanced supersaturation, and therefore forms NU-901 thin films within minutes. The drop casted samples were analyzed using powder X-ray diffraction (PXRD) (**Figure 3.2a**), which showed the formation of NU-901 crystals at both temperatures. We characterized the film morphology using scanning electron microcopy (SEM), which revealed the formation of spherical-shaped crystals (**Figure 3.2b, c**).

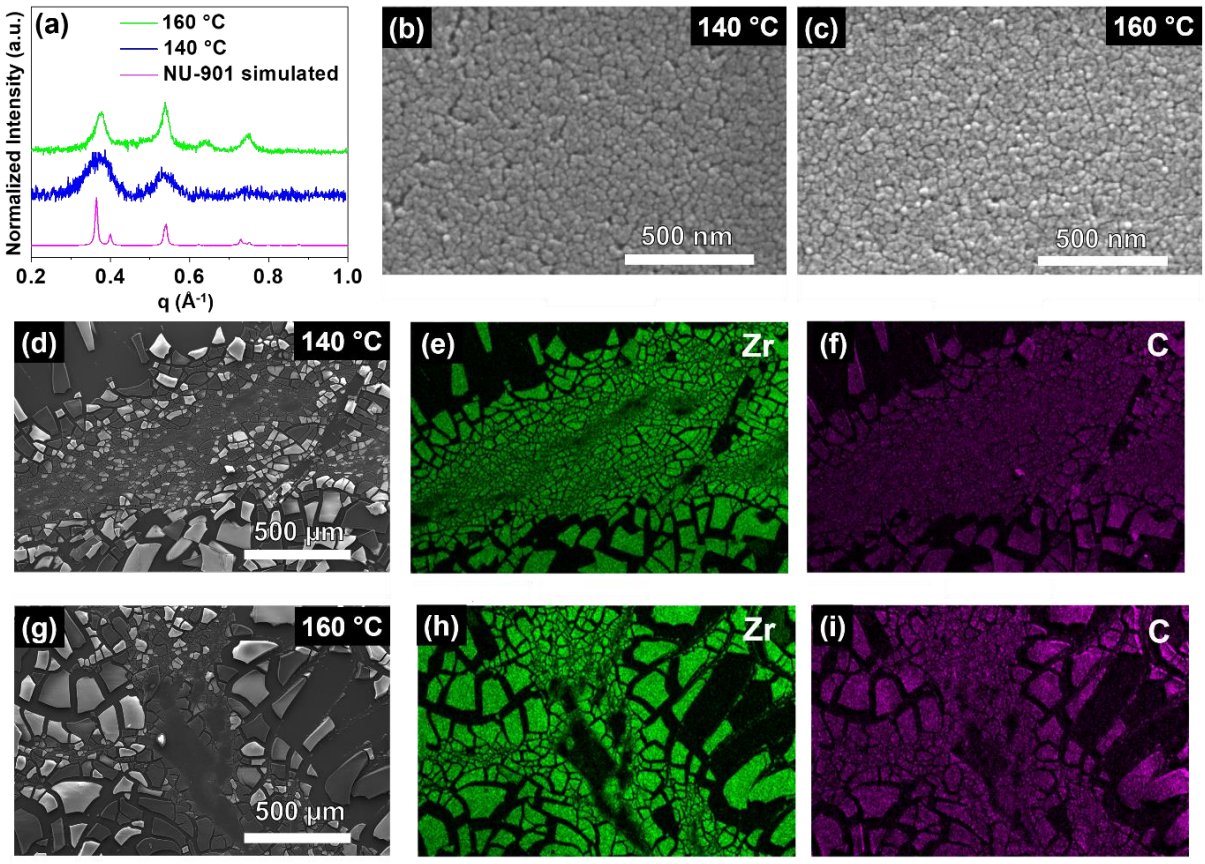

Figure 3.2. *(a) Powder X-ray diffraction (PXRD) patterns of NU-901 films drop casted at different temperatures. Scanning electron microscopy (SEM) images of NU-901 films drop casted at (b) 140 °C and (c) 160 °C. (d) Low magnification SEM image of the NU-901 film drop casted at 140 °C and the corresponding elemental mapping of (e) zirconium (Zr) and (f) carbon (C). (g) Low magnification SEM image of the NU-901 films drop casted at 160 °C and the corresponding elemental mapping of (h) Zr and (i) C. (For all conditions, solvent is DMSO, $ZrOCl_2 \cdot 8H_2O$ concentration is 35.4 mM, H_4TBAPy concentration is 6.8 mM, and formic acid concentration is 1.9 M)*

Similar morphologies have been reported for MOFs where fast crystallization is induced, due to rapid nucleation.[46,47] However, SEM images of the drop casted films (**Figure 3.2d, g**)

suggest a poor film coverage as indicated by the energy dispersive X-ray spectroscopy (EDS) mapping of Zr (**Figure 3.2e, h**) and C (**Figure 3.2f, i**). Indeed, film coverages of 0.59 and 0.58 of the NU-901 crystals are obtained from the films drop casted at 140 °C and 160 °C, respectively. The optical images of the drop casted films (**Figure A3.1, A3.2**) further corroborate the poor film coverage. Therefore, we proceeded with solution shearing to make films with higher coverage.

3.4.1 Solution shearing of NU-901

Briefly, the NU-901 precursor solution is injected between a moving blade and a heated substrate (**Figure 3.1a)** and DMSO evaporation from the meniscus induces supersaturation which facilitates a reaction between Zr-oxo clusters and H_4TBAPy linker to form NU-901. The blade movement spreads NU-901 crystals across the glass substrate to generate a thin film.

To determine the effect of temperature on relevant thin film properties (crystallinity, surface coverage, and thickness), we prepared NU-901 thin films at 140 °C and 160 °C while keeping all other parameters constant as represented in **Table 3.1**. NU-901 crystal formation was confirmed using grazing incidence X-ray diffraction (GIXD). The 2D GIXD patterns (**Figure 3.3a, b**) show the main diffraction peaks at 0.37 $Å^{-1}$ and 0.54 $Å^{-1}$, which correspond to scattering from the (100) and $(1\bar{1}1)$ planes of the NU-901 crystal, showing that NU-901 crystal formation occurs at both temperatures. We integrated the GIXD diffraction peaks to obtain the corresponding 1D intensity curves (**Figure A3.3**). Afterward, we used 1D intensity curves to calculate the coherence length of the NU-901 crystals using the Scherrer equation,[48] where higher coherence length implies higher crystallinity. We find that the crystallinity of the NU-901 crystals increases when the solution shearing temperature is increased from 140 °C to 160 °C (**Table 3.1)**. Farha et al. have shown that the mobility of linker molecules increases with temperature and reduces crystal defects, thus enhancing crystallinity.[49] Similar observations have been reported for UiO-66 and HKUST-1 thin films synthesized using solution shearing.[34,35]

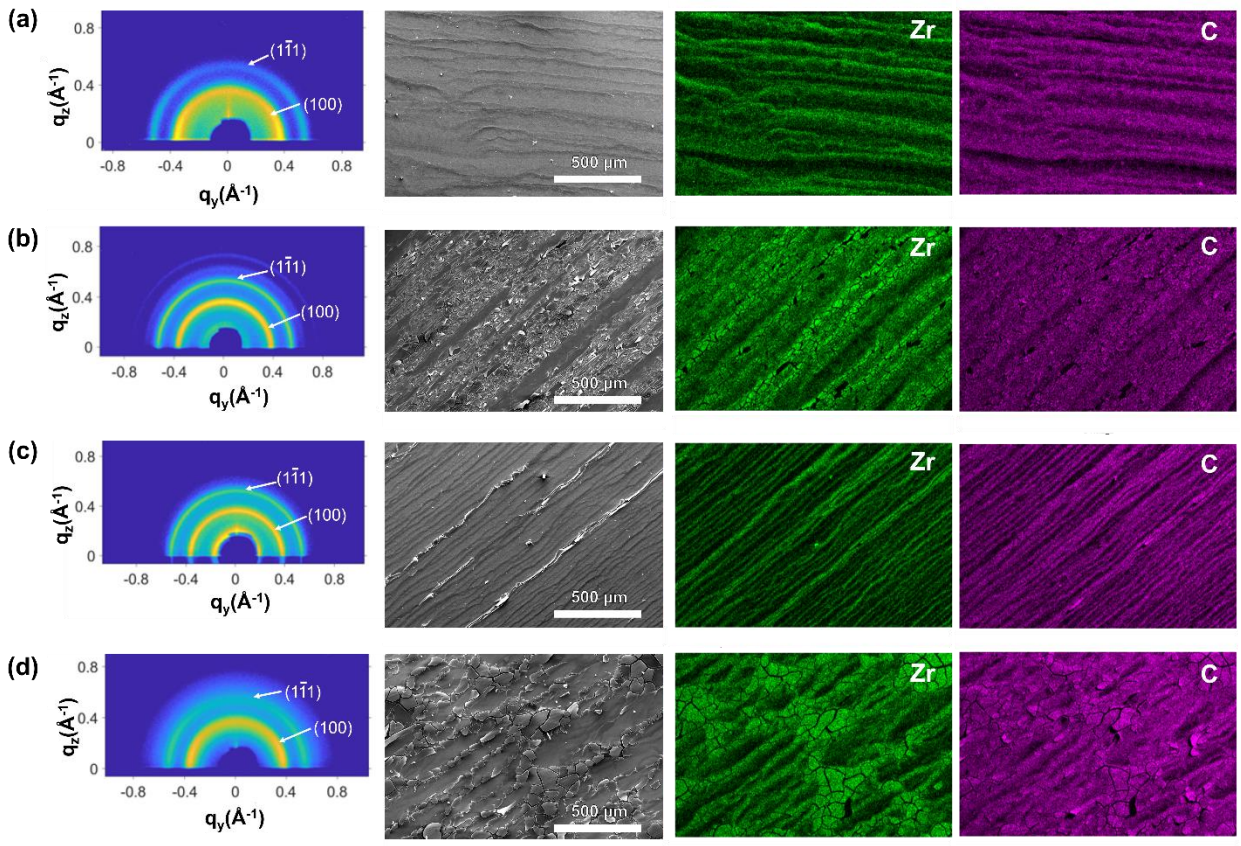

Figure 3.3. *From left to right: 2D grazing incidence X-ray diffraction image showing scattering from NU-901 crystal planes, low magnification SEM image, Zr elemental mapping of the corresponding SEM image, C elemental mapping of the corresponding SEM image of NU-901 films synthesized at (a) 140 °C, 6.8 mM H_4TBAPy, (b) 160 °C, 6.8 mM H_4TBAPy, (c) 160 °C, 3.4 mM H_4TBAPy, and (d) 160 °C, 13.6 mM H_4TBAPy. (For all conditions, solvent is DMSO, $ZrOCl_2$•$8H_2O$ concentration is 35.4 mM, formic acid concentration is 1.9 M, and blade speed is 0.03 mm/s)*

We analyzed the variation in surface coverage and film thickness with temperature using SEM and profilometry, respectively. High-magnification SEM images of the NU-901 films synthesized at 140 °C (**Figure A3.4**) and 160 °C (**Figure A3.5**), suggest the formation of small spherical-shaped crystals at both temperatures. Low magnification SEM images (**Figure 3.3a, b**) show the distribution of Zr and C almost everywhere, indicating excellent surface coverage by NU-901 particles. In fact, the surface coverages of the films are 0.99 and 0.90 synthesized at 140 °C and 160 °C, respectively (**Table 3.1**), demonstrating that we can create films possessing high MOF coverage, which is required for their optimal performance in separation, sensing, and catalysis.[19,44,50]

To study the amount of MOF deposited during solution shearing, we used adjusted thickness defined as a product of surface coverage and film thickness. The adjusted thickness increases with temperature (**Table 3.1**), suggesting the formation of the higher amount of MOF with elevated temperature. We propose that increasing the temperature increases the solvent evaporation rate and enhances the supersaturation of the MOF precursors, resulting in increased MOF crystallization.[35] Importantly, this method is amenable to the large-area (~5 cm^2) fabrication of a NU-901 thin film (**Figure A3.6**), demonstrating the capability of using solution shearing to make large-area MOF thin films, which could be useful for their implementation in various devices.

Since strong adhesion of MOF crystals to the substrate is required for applications under harsh conditions such as use in solutions, at high temperatures, or under strong acidic and basic environments,[20,51] we tested the adhesion of NU-901 crystals to the substrate (**Figure A3.7**). Briefly, scotch tape was attached to the NU-901 film (**Figure A3.7b**) and then peeled off (**Figure A3.7c**).[40] After the tape is removed, the surface coverage decreases from 0.90 to 0.73, showing that loosely bound particles are removed during peeling. Nonetheless, the film shows high (> 0.70) coverage after the adhesion testing, and therefore most particles are strongly attached to the substrate when formed using solution shearing.

3.4.2 Effect of linker concentration

Since it has been shown that metal concentration has minimal effects on the UiO-66 (a Zr-based MOF) crystallization relative to linker concentration,[52] we focused here on the studying the effect of linker concentration on NU-901 thin film properties. We prepared NU-901 thin films at three different linker concentrations (3.4 mM, 6.8 mM, and 13.6 mM) while keeping $ZrOCl_2 \cdot 8H_2O$ concentration at 35.4 mM. The 2D GIXD patterns of the films with different linker concentrations (**Figure 3.3b-d**) exhibit the main diffraction peaks of NU-901 at 0.37 $Å^{-1}$ and 0.54 $Å^{-1}$, which is further corroborated by 1D intensity curves (**Figure A3.8**). Decreasing the linker

concentration from 6.8 mM to 3.4 mM reduces the adjusted thickness from 1.50 μm to 0.48 μm (**Table 3.1**), suggesting that a lower amount of MOF is being deposited because there are fewer linker molecules available to form NU-901 crystals. Additionally, decreasing the linker concentration has minimal effects on the crystallinity of NU-901: the coherence length slightly increases from 12.1 nm to 14.9 nm (**Table 3.1**). The high-magnification SEM image (**Figure A3.9**) indicates the formation of spherical-shaped crystals at 3.4 mM H_4TBAPy and the low-magnification SEM image (**Figure 3.3c**) demonstrates excellent surface coverage (0.98).

On the other hand, increasing the linker concentration from 6.8 mM to 13.6 mM increases the adjusted thickness from 1.50 μm to 3.49 μm, suggesting an increase in MOF formation. However, increasing the linker concentration reduces the crystallinity of NU-901 crystals as shown by the decrease in the coherence length (**Table 3.1**). We suggest that the rapid nucleation and growth of NU-901 crystals upon increasing the linker concentration promotes the formation of defect-rich crystals. Similarly, NU-1000 crystallinity decreased upon increasing the linker concentration as reported by Penn et al.[53] Imaging at high magnification by SEM (**Figure A3.10**) reveals the formation of spherical-shaped crystals, and imaging at low magnification SEM (**Figure 3.3d**) demonstrates excellent film coverage (0.94).

3.4.3 Solution shearing of MOF-525

To show the generalizability of this solution shearing method towards the synthesis of other Zr-based MOFs, we decided to fabricate MOF-525 films on indium tin oxide (ITO) coated glass substrates due to their applicability for electrocatalysis.[44,54] The solution shearing of MOF-525 precursor solution at 140 °C yielded no MOF formation as the GIXD pattern showed no characteristic peaks of MOF-525 (**Figure A3.11**) and SEM images showed no particle-like morphology (**Figure A3.12**). To promote MOF formation, we increased the temperature from 140 °C to 160 °C. At 160 °C, crystallization of MOF-525 occurred as demonstrated by a powder X-ray

diffraction (PXRD) pattern (**Figure A3.13**) but the film coverage was too low for electrocatalysis (**Figure A3.14**). Therefore, we further increased the temperature to 180 °C to increase the solvent evaporation rate and supersaturation, thus enhancing the MOF-525 formation and film coverage.

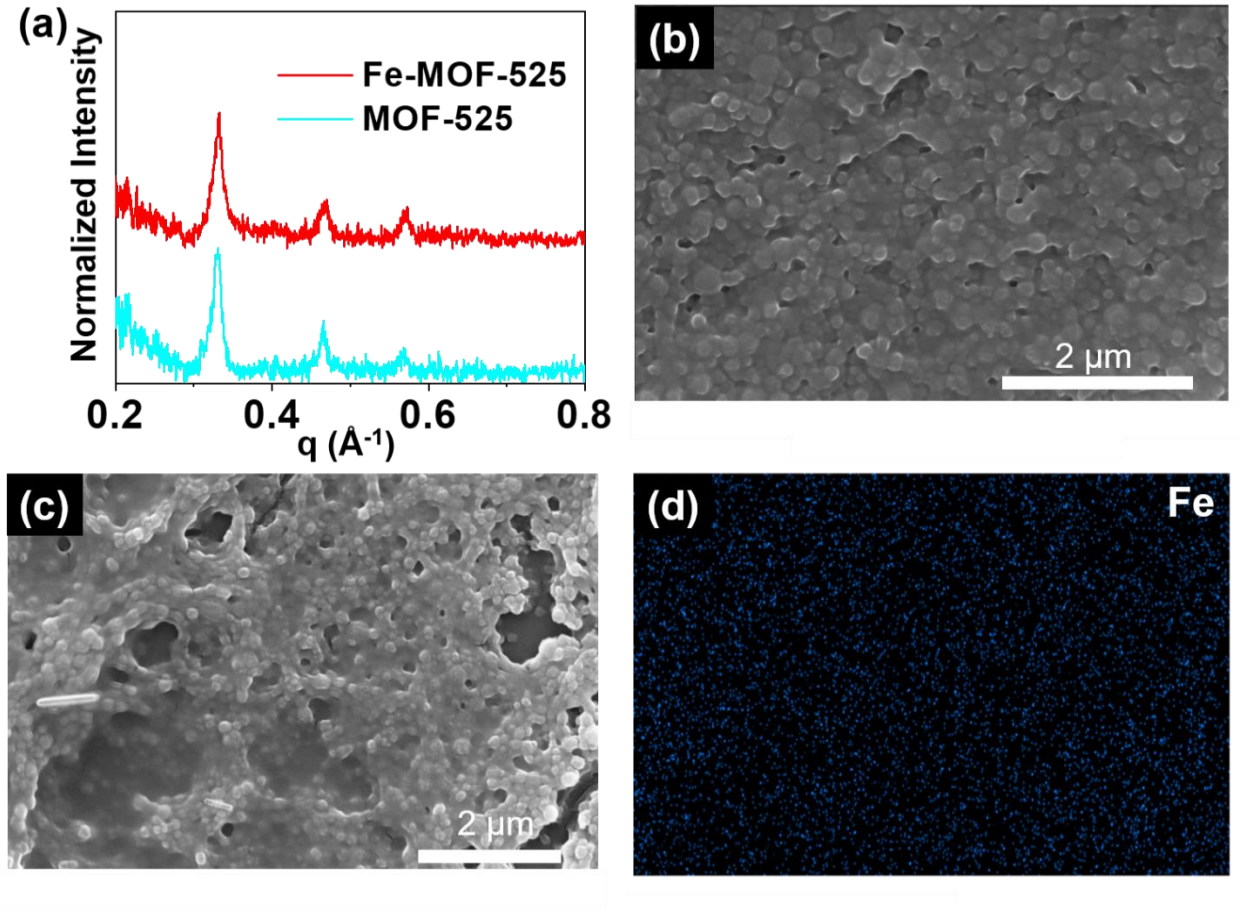

Figure 3.4. *Powder X-ray diffraction (PXRD) patterns of MOF-525 and Fe-MOF-525 thin films. SEM images of (b) MOF-525 and (c) Fe-MOF-525. (d) Elemental mapping of Fe in the Fe-MOF-525 film presented in (c). (For all conditions, solvent is DMSO, $ZrOCl_2 \cdot 8H_2O$ concentration is 35.4 mM, TCPP concentration is 14.1 mM, temperature is 180 °C, formic acid concentration is 1.9 M, and blade speed is 0.025 mm/s)*

The synthesis at 180 °C yielded MOF-525 films, as demonstrated by the PXRD pattern (**Figure 3.4a**), with higher coverage than the films made at 160 °C (**Figure A3.15**). High-magnification SEM image show the formation of spherical-shaped crystals (**Figure 3.4b**) and a film coverage of about 0.9. To utilize the MOF-525 films for electrocatalysis, we created an Fe-MOF-525 reduction catalyst thin film by soaking the MOF-525 films in iron chloride ($FeCl_3$) solution at 80 °C for 24 h.[44] After the soaking process, the crystal structure (**Figure 3.4a**) and morphology

of MOF-525 (**Figure 3.4c**) remain the same. Additionally, EDS mapping shows the homogeneous distribution of Fe within the MOF-525 crystals (**Figure 3.4d, A3.16-A3.17**), suggesting the successful Fe incorporation within MOF-525 crystals. We observed a slight decrease in the fraction coverage from 0.9 to 0.8 after post-metalation, suggesting the removal of loosely bound particles when the substrate is dipped in solution.

3.4.4 Electrochemistry of Fe-MOF-525

The electrocatalysis experiments were performed by the Machan Group at the University of Virgnia. To test the viability of the prepared Fe-MOF-525 as a catalyst for CO_2 reduction, electrochemical experiments were carried out similarly to previously reported experiments.[44] Cyclic voltammetry (CV) was performed to probe the electrochemical activity of the MOF-525 and Fe-MOF-525 films to verify that the solution shearing can produce viable catalytic electrode. Under inert, saturated argon gas conditions, the Fe-MOF-525 expresses a current profile that matches with the non-metalated MOF-525 (**Figure 3.5a**). However, an increase in current is observed under saturated carbon dioxide (CO_2) conditions for Fe-MOF-525, suggesting that CO_2 activation is occurring. Under protic conditions, utilizing 1.0 M 2,2,2-trifluoroethanol (TFE) as a proton donor, the MOF-525 electrode demonstrates an increase in the observed current under both saturated Ar and CO_2 conditions, relative to the absence of TFE (**Figure A3.18**). Interestingly, the current response of Fe-MOF-525 under saturated Ar conditions with TFE is suppressed relative to the MOF-525 electrode; however, under CO_2 saturated conditions Fe-MOF-525 shows a greater current enhancement, consistent with catalytic activity for CO_2 reduction relative to proton reduction (**Figures 3.5b, A3.19**). The increased current is presumed to be in response to CO_2 reduction to carbon monoxide (CO), as was previously observed.[44] The amount of Fe-MOF-525 could not be quantified by electrochemical methods, which is attributed to the sample having a relatively thin layer of MOF on the electrode.

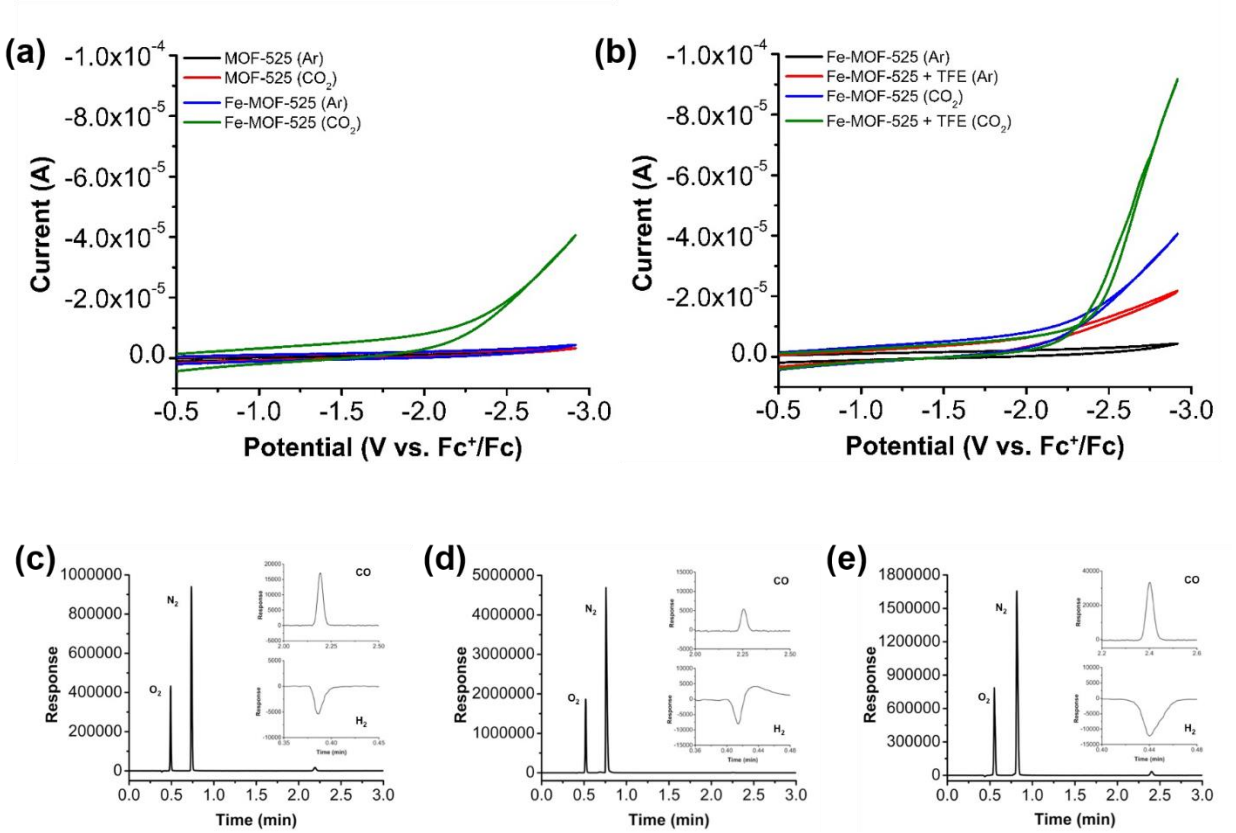

Figure 3.5. *(a) Cyclic voltammograms (CVs) of MOF-525 and Fe-MOF-525 deposited on ITO glass electrodes under saturated Ar and CO2 conditions in 1.0 M TBAPF6/MeCN at a scan rate of 100 mV/s. (b) CVs of Fe-MOF-525 deposited on ITO glass electrodes under saturated Ar and CO_2 conditions with and without TFE as a proton donor in 1.0 M $TBAPF_6$/MeCN at a scan rate of 100 mV/s. Gas chromatograph (GC) from CPE experiment in* ***Figure A3.20*** *of (c) bare ITO glass electrode, (d) MOF-525 deposited on an ITO glass electrode, and (e) Fe-MOF-525 deposited on an ITO glass electrode under saturated CO_2 conditions with 1.0 M TFE as a proton donor. CO and H_2 peak response peaks shown in the inserts.*

In conjunction with CV experiments, controlled potential electrolysis (CPE) was performed to confirm catalytic activity and the evolution of CO. CPE was performed under saturated CO_2 conditions in the presence of 1.0 M TFE, comparing MOF-525, Fe-MOF-525, and bare ITO electrodes at –2.75 V vs. Fc^+/Fc (**Figures A3.20-A3.21**). **Table 3.2** compares the electrochemical activity of the prepared electrodes for CO_2 conversion to CO determined by CPE, in conjunction with product analysis via gas chromatography (**Figures 3.5c-e**). The MOF-525 coated electrode generated less CO than the bare ITO, which suggested limited activity is intrinsic to the Fe-free framework. The Fe-MOF-525 coated electrode passed the most current over the course of the experiment, as well as generated more CO than the bare ITO and MOF-525 electrodes, consistent with its previously reported electrocatalytic activity (**Figure A3.20, Table 3.2**).[44]

Table 3.2. Results of CPE experiments in Figure A3.20 and Figure A3.21 including the integrated CO response, the total charge passed, and the average current at time-point 26609 s.

Controlled Potential Electrolysis Data at 26609 s			
Working Electrode	**Integrated CO Response**	**Charge Passed (C)**	**Avg Current (A)**
Bare ITO	630	0.410	-1.86E-05
MOF-525	230	0.551	-2.07E-05
Fe-MOF-525	1040	0.608	-2.30E-05

3.5 Conclusion

In summary, we show the successful formation of NU-901 and MOF-525 thin films using solution shearing, which utilizes solvent evaporation to induce MOF crystallization. Drop casting the NU-901 precursor solution at high temperatures (140 °C and 160 °C) on a glass substrate facilitates NU-901 crystal formation, demonstrating that solvent evaporation can induce NU-901 crystallization and thin films can be created using solution shearing. Solution shearing provides almost fully covered (> 90%) NU-901 thin films containing spherical-shaped crystals at various synthesis conditions within 15 minutes. We find that increasing the substrate temperature from 140 °C to 160 °C enhances the crystallinity and amount of NU-901 crystals. Decreasing the linker concentration from 6.8 mM to 3.4 mM minimally affects the NU-901 crystallinity but suppresses the formation rate of NU-901 crystallites. Conversely, increasing the linker concentration from 6.8 mM to 13.6 mM decreases the crystallinity but enhances the amount of NU-901 crystals. To demonstrate the capability of solution shearing in creating large-area MOF thin films, we fabricate NU-901 film over an area of 5 cm^2. To show the generalizability of solution shearing to make films of other Zr-MOFs, we synthesize MOF-525 thin films for their electrocatalytic activity. We incorporate Fe in MOF-525 films to obtain Fe-MOF-525 films, which are electrocatalytically active under CO_2-saturated solutions as indicated by CV measurements. CPE of Fe-MOF-525 further confirms catalytic activity under CO_2-saturated conditions and gas chromatography detects the

formation of CO and H_2. These reaction products, particularly CO, are useful feedstocks for production of fuels and industrial chemicals.

Overall, this study displays the versatility of solution shearing in controlling thin film properties. Other parameters, such as, blade speed and solvent can also be varied to study their effects on MOF thin film properties. We believe that our work significantly advances the field of MOF thin films by forming large-pore Zr-MOF films within minutes using solution shearing. We are currently evaluating the capability of solution shearing to creating thin films of other Zr-MOFs, such as, NU-1000 and MOF-545.

3.6 Appendix

Surface coverage analysis:

Film coverages were determined using ImageJ software. The images were converted to red and black colors using the software, where red color represents the area covered by MOF particles and black colors represents the bare substrates. For example,

This is a SEM image of NU-901 film (160 °C, 35.4 mM $ZrOCl_2 \cdot 8H_2O$, 1.9 M formic acid, 3.4 mM H_4TBAPy, and 0.03 mm/s blade speed):

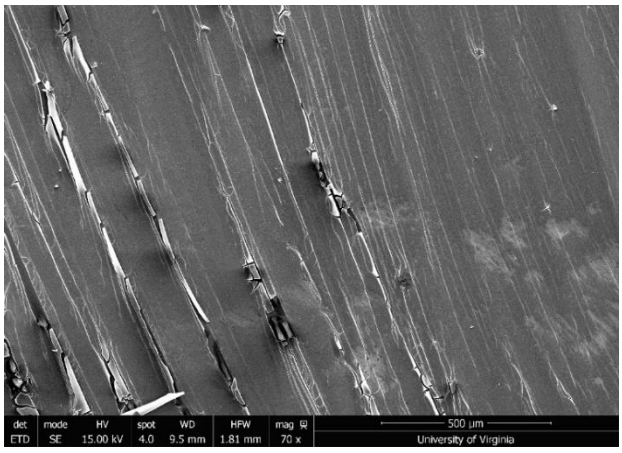

The same image after converting to red and black color:

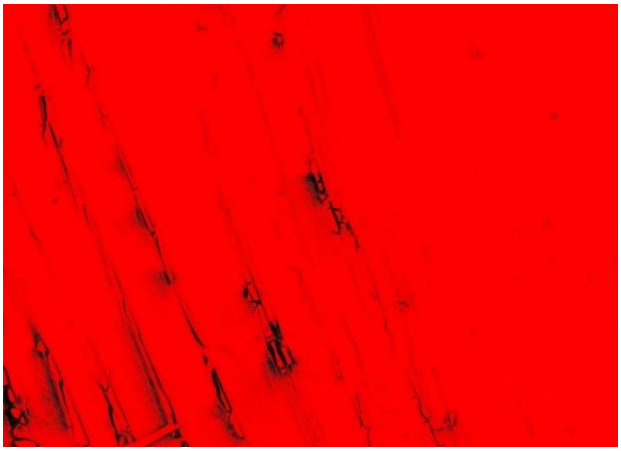

Film coverage was calculated using the following equation:

$$\boldsymbol{Film\ Coverage} = \frac{\boldsymbol{Area\ covered\ by\ the\ red\ color}}{\boldsymbol{Total\ area}}$$

Coherence Length Calculation:

Coherence length was calculated using the Scherrer equation,[48]

$$D = K\frac{2\pi}{\Delta q}$$

Where,

D = Coherence length

K = Constant (0.94 for spherical particle)

Δq = Full width half max (FWHM) of the most intense peak in the 1D diffraction patterns

Figure A3.1. *Optical image of the NU-901 film drop casted at 140 °C. (For this condition, solvent is DMSO, $ZrOCl_2 \cdot 8H_2O$ concentration is 35.4 mM, H_4TBAPy concentration is 6.8 mM, and formic acid concentration is 1.9 M)*

Figure A3.2. *Optical image of the NU-901 film drop casted at 160 °C. (For this condition, solvent is DMSO, $ZrOCl_2 \cdot 8H_2O$ concentration is 35.4 mM, H_4TBAPy concentration is 6.8 mM, and formic acid concentration is 1.9 M)*

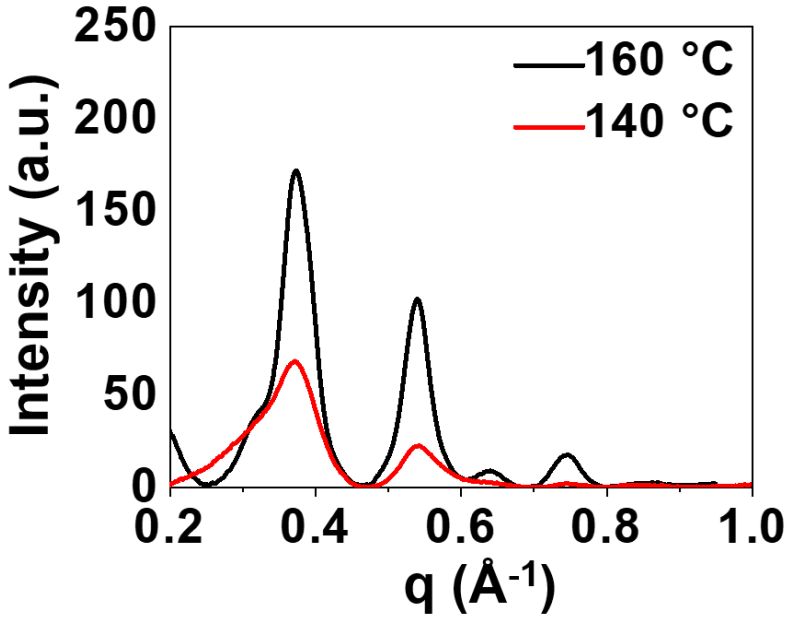

Figure A3.3. *Integrated 1D GIXD data of NU-901 films synthesized at 140 °C and 160 °C using solution shearing. (For all conditions, solvent is DMSO, $ZrOCl_2 \cdot 8H_2O$ concentration is 35.4 mM, H_4TBAPy concentration is 6.8 mM, formic acid concentration is 1.9 M, and blade speed is 0.03 mm/s)*

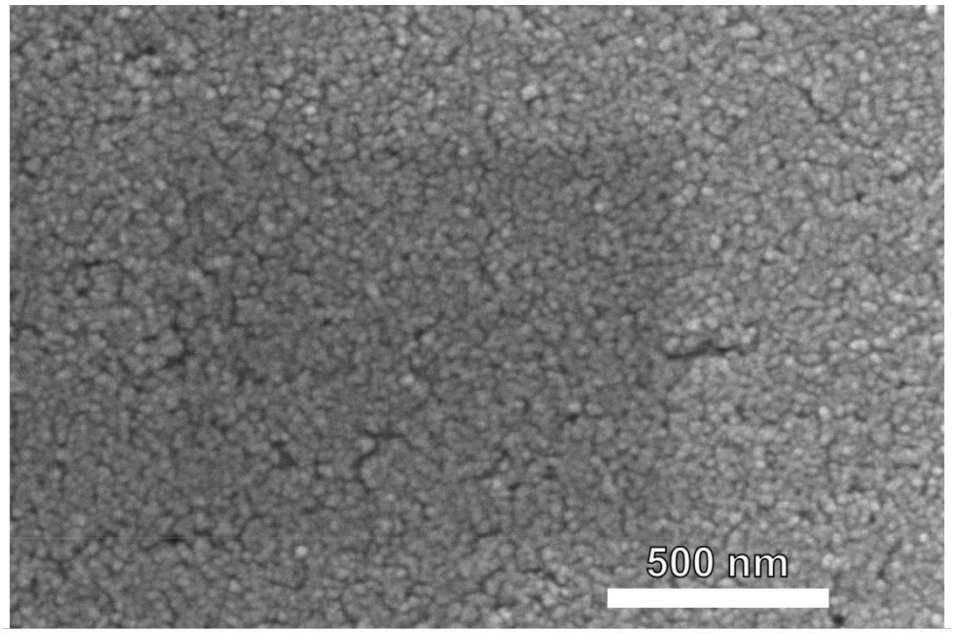

Figure A3.4. *High magnification SEM image of NU-901 film synthesized at 140 °C using solution shearing. (For this condition, solvent is DMSO, $ZrOCl_2 \cdot 8H_2O$ concentration is 35.4 mM, H_4TBAPy concentration is 6.8 mM, formic acid concentration is 1.9 M, and blade speed is 0.03 mm/s)*

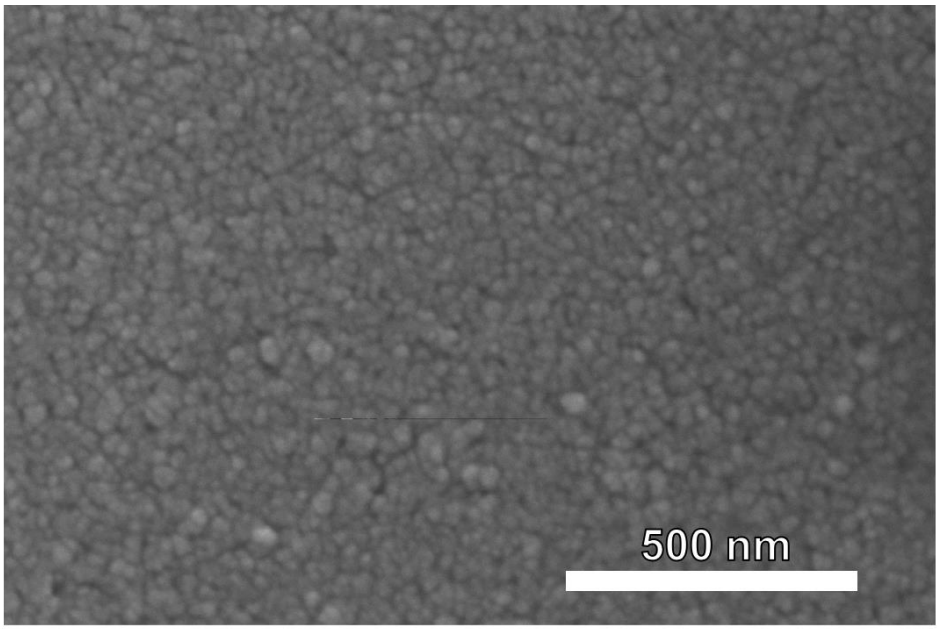

Figure A3.5. *High magnification SEM image of NU-901 film synthesized at 160 °C using solution shearing. (For this condition, solvent is DMSO, $ZrOCl_2 \cdot 8H_2O$ concentration is 35.4 mM, H_4TBAPy concentration is 6.8 mM, formic acid concentration is 1.9 M, and blade speed is 0.03 mm/s)*

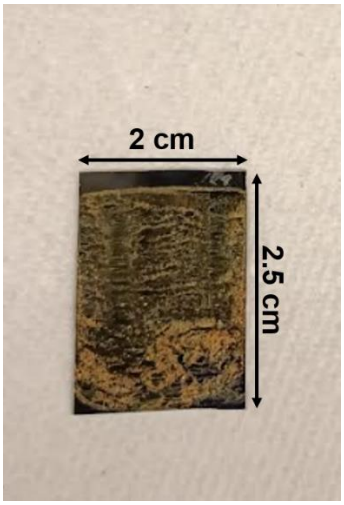

Figure A3.6. *Large-area (~5 cm2) fabrication of the NU-901 thin film using solution shearing. (The film is synthesized at the following conditions: solvent is DMSO, $ZrOCl_2 \cdot 8H_2O$ concentration is 35.4 mM, H_4TBAPy concentration is 6.8 mM, formic acid concentration is 1.9 M, temperature is 160 °C, and blade speed is 0.03 mm/s)*

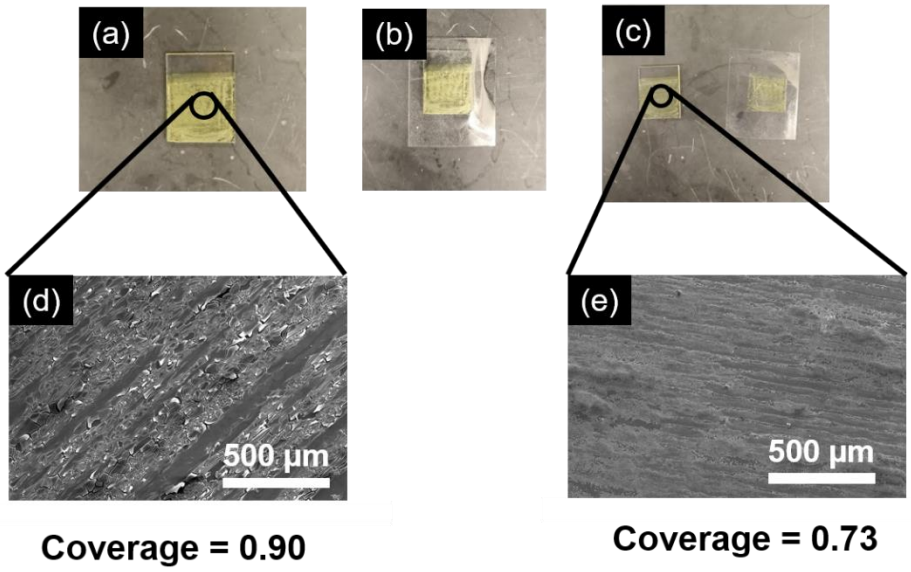

Figure A3.7. *Adhesion testing of the NU-901 film using scotch tape test. (a) Image of NU-901 film before the test. (b) Tape is attached to the NU-901 film. (c) The NU-901 film after tape is peeled off. (d) SEM image of the film shown in (a). (e) SEM image of the film shown in (c). (For this adhesion testing, the film is synthesized at the following conditions: solvent is DMSO, $ZrOCl_2 \cdot 8H_2O$ concentration is 35.4 mM, H_4TBAPy concentration is 6.8 mM, formic acid concentration is 1.9 M, temperature is 160 °C, and blade speed is 0.03 mm/s)*

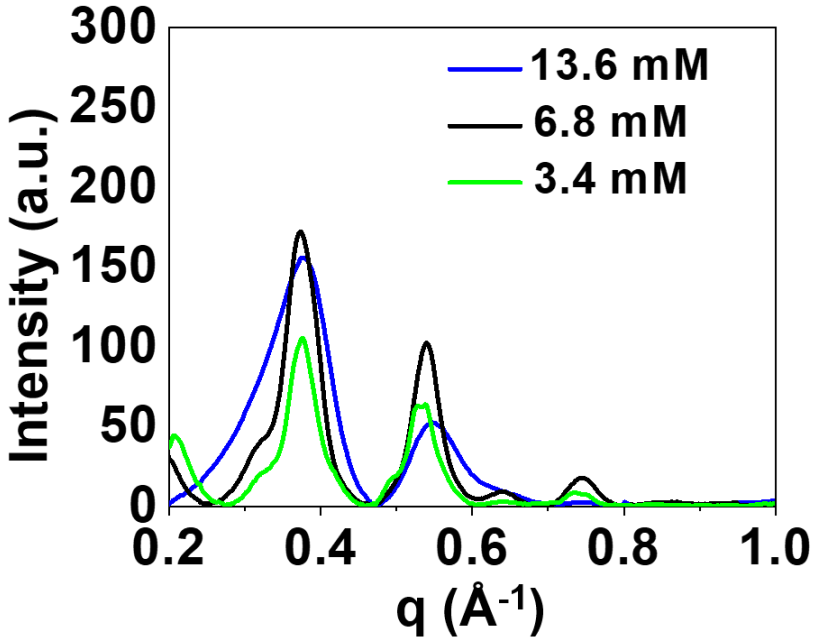

Figure A3.8. *Integrated 1D GIXD data of NU-901 films synthesized at different H_4TBAPy concentrations using solution shearing. (For all conditions, solvent is DMSO, $ZrOCl_2 \cdot 8H_2O$ concentration is 35.4 mM, temperature is 160 °C, formic acid concentration is 1.9 M, and blade speed is 0.03 mm/s)*

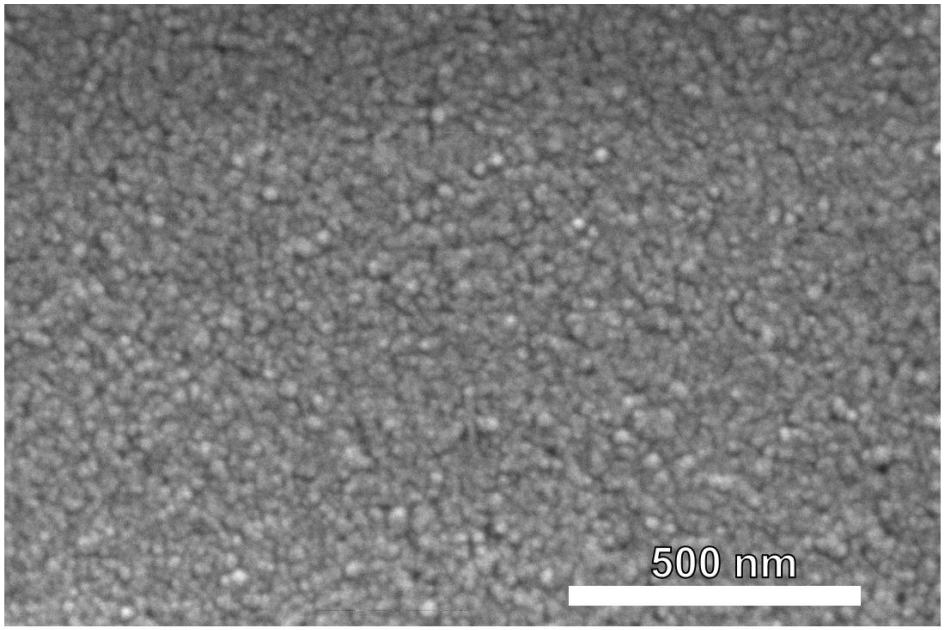

Figure A3.9. *High magnification SEM image of NU-901 film synthesized at 3.4 mM H_4TBAPy using solution shearing. (For this condition, solvent is DMSO, $ZrOCl_2 \cdot 8H_2O$ concentration is 35.4 mM, temperature is 160 °C, formic acid concentration is 1.9 M, and blade speed is 0.03 mm/s).*

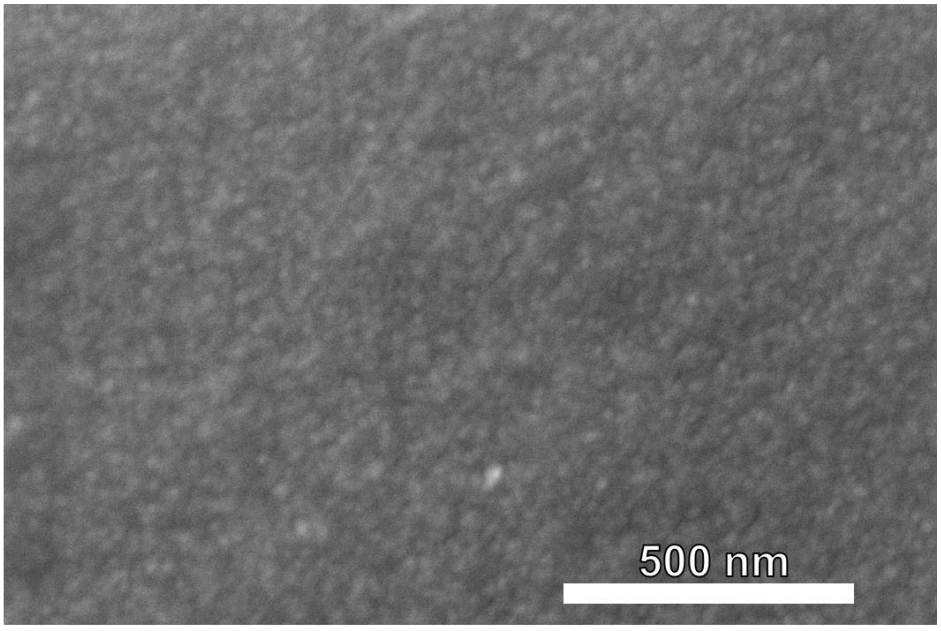

Figure A3.10. *High magnification SEM image of NU-901 film synthesized at 13.6 mM H_4TBAPy using solution shearing. (For this condition, solvent is DMSO, $ZrOCl_2 \cdot 8H_2O$ concentration is 35.4 mM, temperature is 160 °C, formic acid concentration is 1.9 M, and blade speed is 0.03 mm/s)*

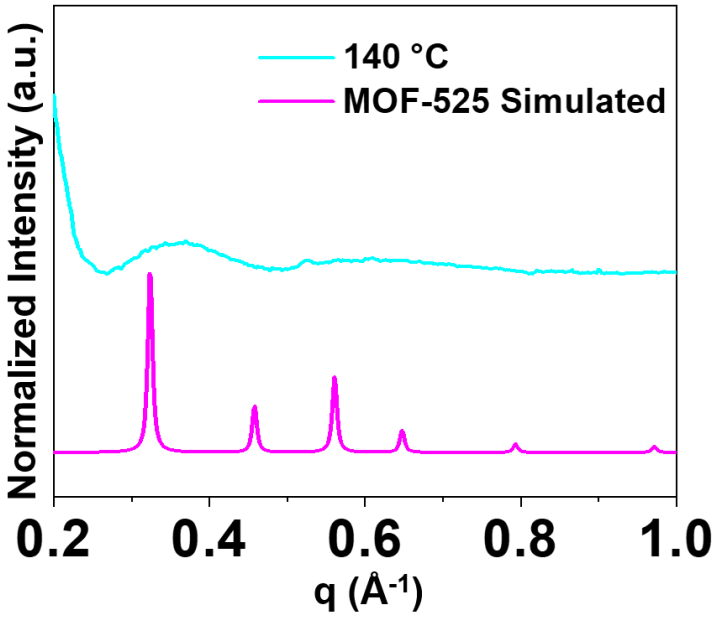

Figure A3.11. *Integrated 1D GIXD data of the MOF-525 film synthesized at 140 °C using solution shearing. (For this condition, solvent is DMSO, $ZrOCl_2 \cdot 8H_2O$ concentration is 35.4 mM, TCPP concentration is 14.1 mM, formic acid concentration is 1.9 M, and blade speed is 0.025 mm/s)*

Figure A3.12. *High magnification SEM image of the MOF-525 film synthesized at 140 °C using solution shearing. (For this condition, solvent is DMSO, $ZrOCl_2 \cdot 8H_2O$ concentration is 35.4 mM, TCPP concentration is 14.1 mM, formic acid concentration is 1.9 M, and blade speed is 0.025 mm/s)*

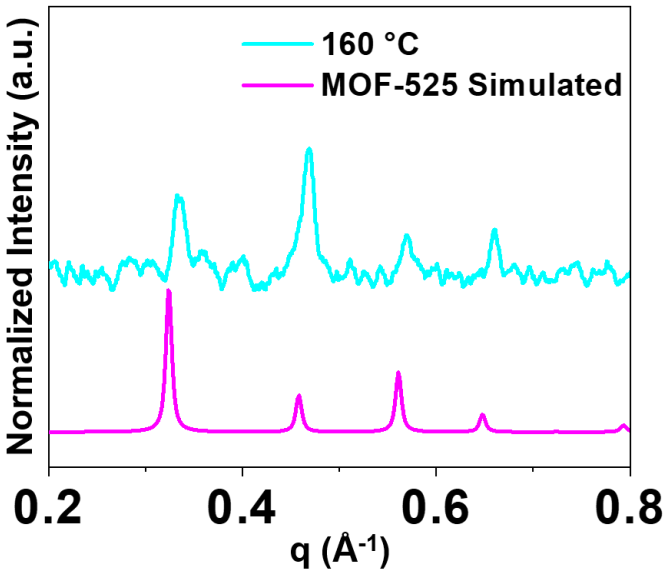

Figure A3.13. *Powder X-ray diffraction (PXRD) pattern of the MOF-525 film synthesized at 160 °C using solution shearing. (For this condition, solvent is DMSO, $ZrOCl_2 \cdot 8H_2O$ concentration is 35.4 mM, TCPP concentration is 14.1 mM, formic acid concentration is 1.9 M, and blade speed is 0.025 mm/s)*

Figure A3.14. *Optical image of the MOF-525 film synthesized at 160 °C using solution shearing. (For this condition, solvent is DMSO, $ZrOCl_2 \cdot 8H_2O$ concentration is 35.4 mM, TCPP concentration is 14.1 mM, formic acid concentration is 1.9 M, and blade speed is 0.025 mm/s)*

Figure A3.15. *Optical image of the MOF-525 film synthesized at 180 °C using solution shearing. (For this condition, solvent is DMSO, $ZrOCl_2 \cdot 8H_2O$ concentration is 35.4 mM, TCPP concentration is 14.1 mM, formic acid concentration is 1.9 M, and blade speed is 0.025 mm/s)*

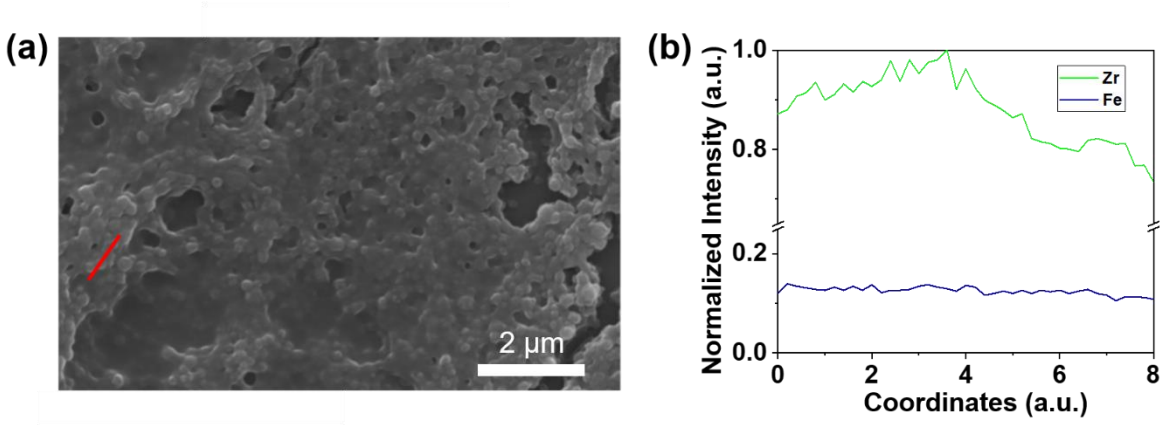

Figure A3.16. *Line scan data of Fe-MOF-525 film shows homogeneous distribution of Fe within MOF crystals. (For this condition, solvent is DMSO, $ZrOCl_2 \cdot 8H_2O$ concentration is 35.4 mM, TCPP concentration is 14.1 mM, formic acid concentration is 1.9 M, and blade speed is 0.025 mm/s)*

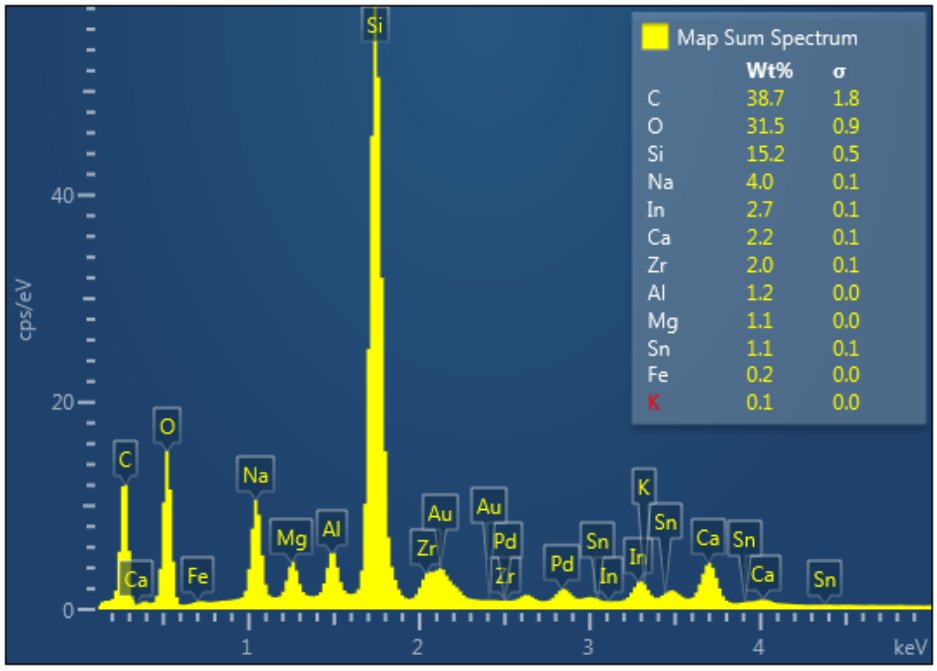

Figure A3.17. *Elemental wt% of the Fe-MOF-525 film shown in* ***Figure A3.16*** *Fe peak and Fe wt% confirm the presence of Fe within MOF-525 crystals.*

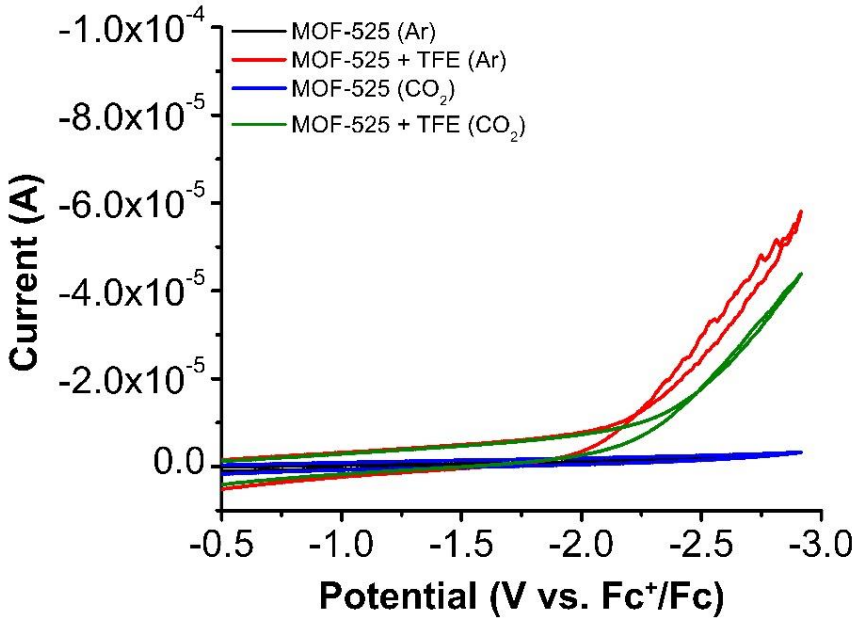

Figure A3.18. *CVs of MOF-525 deposited on ITO glass electrodes under saturated Ar and CO_2 conditions with and without TFE as a proton donor in 1.0 M $TBAPF_6$/MeCN at a scan rate of 100 mV/s.*

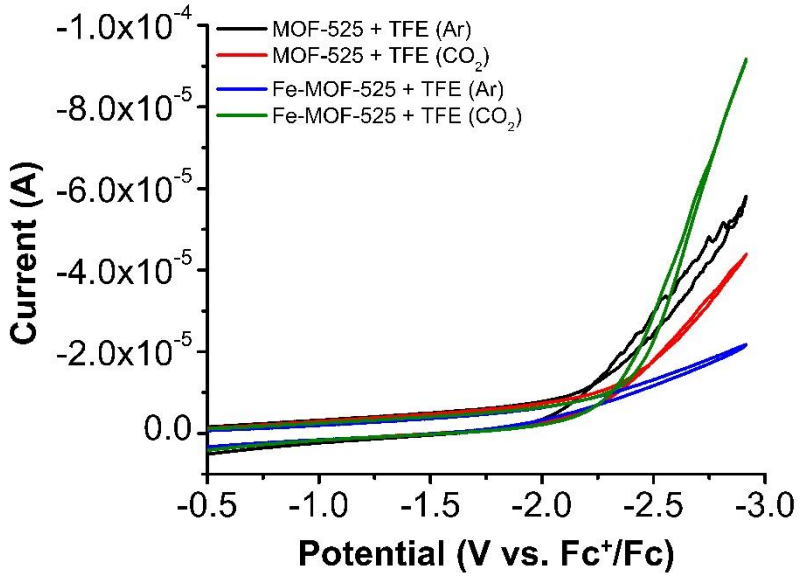

Figure A3.19. *CVs of MOF-525 and Fe-MOF-525 deposited on ITO glass electrodes under saturated Ar and CO_2 conditions with 1.0 M TFE as a proton donor in 1.0 M $TBAPF_6$/MeCN at a scan rate of 100 mV/s.*

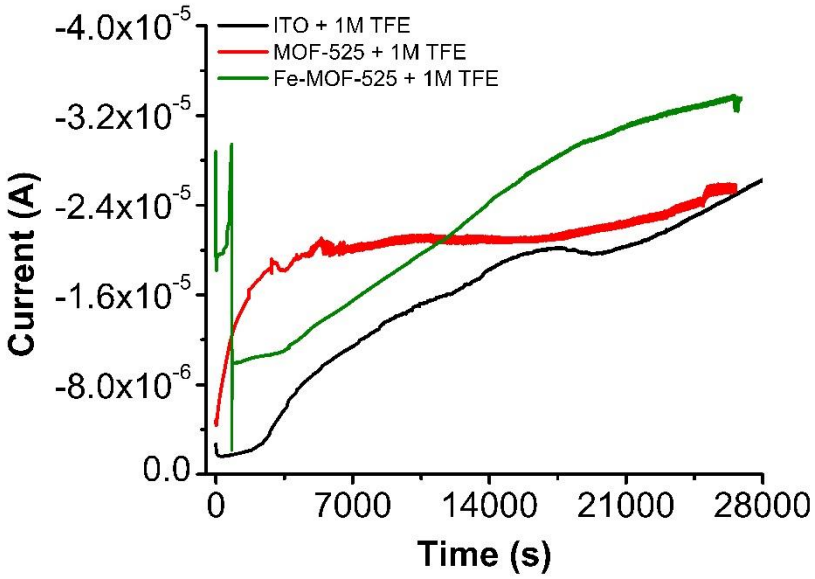

Figure A3.20. *Current versus time trace from CPE experiments of MOF-525, Fe-MOF-525, and bare ITO glass electrodes under saturated CO_2 conditions with 1.0 M TFE as a proton donor. Conditions: −2.75 V vs Fc+/Fc in 1.0 M $TBAPF_6$/MeCN.*

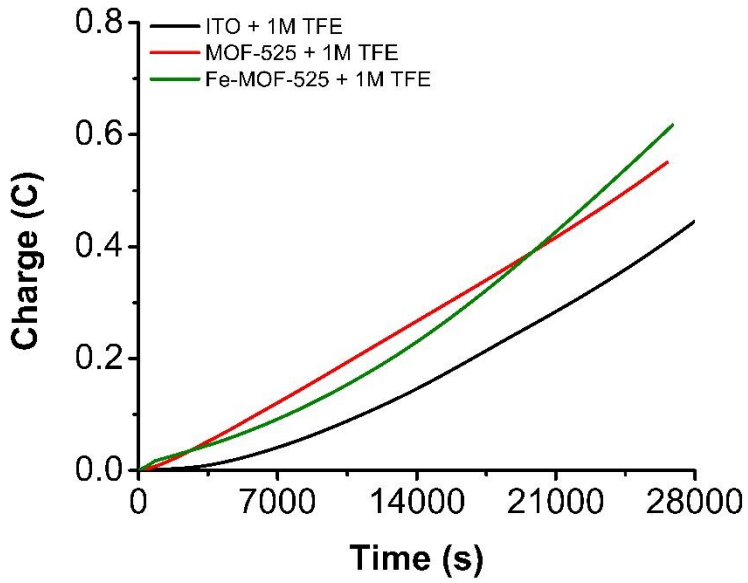

Figure A3.21. *Charge vs. Time plot from CPE experiments of MOF-525, Fe-MOF-525, and bare ITO glass electrodes under saturated CO_2 conditions with 1.0 M TFE as a proton donor. Conditions: −2.75 V vs Fc+/Fc in 1.0 M $TBAPF_6$/MeCN.*

3.7 References

(1) Furukawa, H.; Cordova, K. E.; O'Keeffe, M.; Yaghi, O. M. The Chemistry and Applications of Metal-Organic Frameworks. *Science* **2013**, *341* (6149), 1230444.

(2) Allendorf, M. D.; Stavila, V. Crystal Engineering, Structure-Function Relationships, and the Future of Metal-Organic Frameworks. *CrystEngComm* **2015**, *17* (2), 229–246.

(3) Kirchon, A.; Feng, L.; Drake, H. F.; Joseph, E. A.; Zhou, H. C. From Fundamentals to Applications: A Toolbox for Robust and Multifunctional MOF Materials. *Chem. Soc. Rev.* **2018**, *47* (23), 8611–8638.

(4) Mahmoud, E.; Ali, L.; Sayah, A. El; Alkhatib, S. A.; Abdulsalam, H.; Juma, M.; Al-Muhtaseb, A. H. Implementing Metal-Organic Frameworks for Natural Gas Storage. *Crystals* **2019**, *9* (8), 406.

(5) Ma, S.; Zhou, H. C. Gas Storage in Porous Metal-Organic Frameworks for Clean Energy Applications. *Chem. Commun.* **2010**, *46* (1), 44–53.

(6) Yang, X.; Xu, Q. Bimetallic Metal-Organic Frameworks for Gas Storage and Separation. *Cryst. Growth Des.* **2017**, *17* (4), 1450–1455.

(7) Li, H.; Wang, K.; Sun, Y.; Lollar, C. T.; Li, J.; Zhou, H. C. Recent Advances in Gas Storage and Separation Using Metal–Organic Frameworks. *Mater. Today* **2018**, *21* (2), 108–121.

(8) Qian, Q.; Asinger, P. A.; Lee, M. J.; Han, G.; Mizrahi Rodriguez, K.; Lin, S.; Benedetti, F. M.; Wu, A. X.; Chi, W. S.; Smith, Z. P. MOF-Based Membranes for Gas Separations. *Chem. Rev.* **2020**, *120* (16), 8161–8266.

(9) Li, X.; Liu, Y.; Wang, J.; Gascon, J.; Li, J.; Van Der Bruggen, B. Metal-Organic Frameworks Based Membranes for Liquid Separation. *Chem. Soc. Rev.* **2017**, *46* (23), 7124–7144.

(10) Yang, D.; Gates, B. C. Catalysis by Metal Organic Frameworks: Perspective and Suggestions for Future Research. *ACS Catal.* **2019**, *9* (3), 1779–1798.

(11) Ranocchiari, M.; Bokhoven, J. A. Van. Catalysis by Metal-Organic Frameworks: Fundamentals and Opportunities. *Phys. Chem. Chem. Phys.* **2011**, *13* (14), 6388–6396.

(12) Dong, J.; Zhao, D.; Lu, Y.; Sun, W. Y. Photoluminescent Metal-Organic Frameworks and Their Application for Sensing Biomolecules. *J. Mater. Chem. A* **2019**, *7* (40), 22744–22767.

(13) Ma, T.; Li, H.; Ma, J. G.; Cheng, P. Application of MOF-Based Materials in Electrochemical

Sensing. *Dalt. Trans.* **2020**, *49* (47), 17121–17129.
(14) Yang, G. L.; Jiang, X. L.; Xu, H.; Zhao, B. Applications of MOFs as Luminescent Sensors for Environmental Pollutants. *Small* **2021**, *17* (22), 1–19.
(15) Bétard, A.; Fischer, R. A. Metal-Organic Framework Thin Films: From Fundamentals to Applications. *Chem. Rev.* **2012**, *112* (2), 1055–1083.
(16) Shekhah, O.; Liu, J.; Fischer, R. A.; Wöll, C. MOF Thin Films: Existing and Future Applications. *Chem. Soc. Rev.* **2011**, *40* (2), 1081–1106.
(17) Heinke, L.; Tu, M.; Wannapaiboon, S.; Fischer, R. A.; Wöll, C. Surface-Mounted Metal-Organic Frameworks for Applications in Sensing and Separation. *Microporous Mesoporous Mater.* **2015**, *216*, 200–215.
(18) Ranjan, R.; Tsapatsis, M. Microporous Metal Organic Framework Membrane on Porous Support Using the Seeded Growth Method. *Chem. Mater.* **2009**, *21* (20), 4920–4924.
(19) Qiu, S.; Xue, M.; Zhu, G. Metal-Organic Framework Membranes: From Synthesis to Separation Application. *Chem. Soc. Rev.* **2014**, *43* (16), 6116–6140.
(20) Kung, C. W.; Mondloch, J. E.; Wang, T. C.; Bury, W.; Hoffeditz, W.; Klahr, B. M.; Klet, R. C.; Pellin, M. J.; Farha, O. K.; Hupp, J. T. Metal-Organic Framework Thin Films as Platforms for Atomic Layer Deposition of Cobalt Ions to Enable Electrocatalytic Water Oxidation. *ACS Appl. Mater. Interfaces* **2015**, *7* (51), 28223–28230.
(21) Kung, C. W.; Audu, C. O.; Peters, A. W.; Noh, H.; Farha, O. K.; Hupp, J. T. Copper Nanoparticles Installed in Metal-Organic Framework Thin Films Are Electrocatalytically Competent for CO_2 Reduction. *ACS Energy Lett.* **2017**, *2* (10), 2394–2401.
(22) Denny, M. S.; Moreton, J. C.; Benz, L.; Cohen, S. M. Metal–Organic Frameworks for Membrane-Based Separations. *Nat Rev Mater* **2016**, *1* (12), 16078.
(23) Wade, C. R.; Li, M.; Dincă, M. Facile Deposition of Multicolored Electrochromic Metal-Organic Framework Thin Films. *Angew. Chem., Int. Ed.* **2013**, *52* (50), 13377–13381.
(24) Miyamoto, M.; Kohmura, S.; Iwatsuka, H.; Oumi, Y.; Uemiya, S. In Situ Solvothermal Growth of Highly Oriented Zr-Based Metal Organic Framework UiO-66 Film with Monocrystalline Layer. *CrystEngComm* **2015**, *17* (18), 3422–3425.
(25) Ahrenholtz, S. R.; Epley, C. C.; Morris, A. J. Solvothermal Preparation of an Electrocatalytic Metalloporphyrin MOF Thin Film and Its Redox Hopping Charge-Transfer Mechanism. *J. Am. Chem. Soc.* **2014**, *136* (6), 2464–2472.
(26) So, M. C.; Jin, S.; Son, H. J.; Wiederrecht, G. P.; Farha, O. K.; Hupp, J. T. Layer-by-Layer Fabrication of Oriented Porous Thin Films Based on Porphyrin-Containing Metal-Organic Frameworks. *J. Am. Chem. Soc.* **2013**, *135* (42), 15698–15701.
(27) Ohara, H.; Yamamoto, S.; Kuzuhara, D.; Koganezawa, T.; Oikawa, H.; Mitsuishi, M. Layer-by-Layer Growth Control of Metal-Organic Framework Thin Films Assembled on Polymer Films. *ACS Appl. Mater. Interfaces* **2020**, *12* (45), 50784–50792.
(28) Gu, Z. G.; Zhang, J. Epitaxial Growth and Applications of Oriented Metal–Organic Framework Thin Films. *Coord. Chem. Rev.* **2019**, *378*, 513–532.
(29) Hod, I.; Bury, W.; Karlin, D. M.; Deria, P.; Kung, C.-W.; Katz, M. J.; So, M.; Klahr, B.; Jin, D.; Chung, Y.-W.; Odom, T. W.; Farha,O. K.; Hupp, J. T. Directed Growth of Electroactive Metal-Organic Framework Thin Films Using Electrophoretic Deposition. *Adv. Mater.* **2014**, *26*, 6295−6300.
(30) Kang, X.; Zhu, Q.; Sun, X.; Hu, J.; Zhang, J.; Liu, Z.; Han, B. Highly Efficient Electrochemical reduction of CO_2 to CH_4 in an Ionic Liquid Using a Metal-Organic Framework Cathode.
(31) Feng, J. F.; Gao, S. Y.; Liu, T. F.; Shi, J.; Cao, R. Preparation of Dual-Emitting Ln@UiO-66-Hybrid Films via Electrophoretic Deposition for Ratiometric Temperature Sensing. *ACS Appl. Mater. Interfaces* **2018**, *10* (6), 6014–6023.
(32) Han, H.; Yuan, X.; Zhang, Z.; Zhang, J. Preparation of a ZIF-67 Derived Thin Film Electrode via Electrophoretic Deposition for Efficient Electrocatalytic Oxidation of Vanillin. *Inorg. Chem.* **2019**, *58* (5), 3196–3202.
(33) Lee, J. C.; Kim, J. O.; Lee, H. J.; Shin, B.; Park, S. Meniscus-Guided Control of Supersaturation for the Crystallization of High Quality Metal Organic Framework Thin Films. *Chem. Mater.* **2019**, *31* (18), 7377–7385.
(34) Jung, S.; Huelsenbeck, L.; Hu, Q.; Robinson, S.; Giri, G. Conductive, Large-Area, and Continuous 7,7,8,8-Tetracyanoquinodimethane@HKUST-1 Thin Films Fabricated Using Solution Shearing.

ACS Appl. Mater. Interfaces **2021**, *13* (8), 10202–10209.
(35) Jung, S.; Verma, P.; Robinson, S.; Beyer, E.; Hall, H.; Huelsenbeck, L.; Stone, K. H.; Giri, G. Meniscus Guided Coating and Evaporative Crystallization of UiO-66 Metal Organic Framework Thin Films. *Ind. Eng. Chem. Res.* **2021**, *60* (48), 17585–17595.
(36) Huelsenbeck, L.; Jung, S.; Herrera Del Valle, R.; Balachandran, P. V.; Giri, G. Accelerated HKUST-1 Thin-Film Property Optimization Using Active Learning. *ACS Appl. Mater. Interfaces* **2021**, *13* (51), 61827–61837.
(37) Kim, J. O.; Koo, W. T.; Kim, H.; Park, C.; Lee, T.; Hutomo, C. A.; Choi, S. Q.; Kim, D. S.; Kim, I. D.; Park, S. Large-Area Synthesis of Nanoscopic Catalyst-Decorated Conductive MOF Film Using Microfluidic-Based Solution Shearing. *Nat. Commun.* **2021**, *12* (1), 1–8.
(38) Lee, T.; Kim, J.-O.; Park, C.; Kim, H.; Kim, M.; Park, H.; Kim, I.; Ko, J.; Pak, K.; Choi, S. Q.; Kim, I.-D.; Park, S.; Large-Area Synthesis of Ultrathin, Flexible, and Transparent Conductive Metal–Organic Framework Thin Films *via* a Microfluidic-Based Solution Shearing Process. *Adv. Mater.* **2022**, *34*, 2107696.
(39) Ghorbanpour, A.; Huelsenbeck, L. D.; Smilgies, D.-M.; Giri, G. Oriented UiO-66 Thin Films Through Solution Shearing. *CrystEngComm* **2018**, *20*, 294–300.
(40) Verma, P. K.; Huelsenbeck, L.; Nichols, A. W.; Islamoglu, T.; Heinrich, H.; Machan, C. W.; Giri, G. Controlling Polymorphism and Orientation of NU-901/NU-1000 Metal-Organic Framework Thin Films. *Chem. Mater.* **2020**, *32* (24), 10556–10565.
(41) Gong, X.; Gnanasekaran, K.; Ma, K.; Forman, C. J.; Wang, X.; Su, S.; Farha, O. K.; Gianneschi, N. C. Rapid Generation of Metal-Organic Framework Phase Diagrams by High-Throughput Transmission Electron Microscopy. *J. Am. Chem. Soc.* **2022**, *144* (15), 6674–6680.
(42) Kelty, M. L.; Morris, W.; Gallagher, A. T.; Anderson, J. S.; Brown, K. A.; Mirkin, C. A.; Harris, T. D. High-Throughput Synthesis and Characterization of Nanocrystalline Porphyrinic Zirconium Metal-Organic Frameworks. *Chem. Commun.* **2016**, *52* (50), 7854–7857.
(43) Feng, D.; Chung, W. C.; Wei, Z.; Gu, Z. Y.; Jiang, H. L.; Chen, Y. P.; Darensbourg, D. J.; Zhou, H. C. Construction of Ultrastable Porphyrin Zr Metal-Organic Frameworks through Linker Elimination. *J. Am. Chem. Soc.* **2013**, *135* (45), 17105–17110.
(44) Hod, I.; Sampson, M. D.; Deria, P.; Kubiak, C. P.; Farha, O. K.; Hupp, J. T. Fe-Porphyrin-Based Metal-Organic Framework Films as High-Surface Concentration, Heterogeneous Catalysts for Electrochemical Reduction of CO_2. *ACS Catal.* **2015**, *5* (11), 6302–6309.
(45) MacRae, C. F.; Sovago, I.; Cottrell, S. J.; Galek, P. T. A.; McCabe, P.; Pidcock, E.; Platings, M.; Shields, G. P.; Stevens, J. S.; Towler, M.; Wood, P. A. Mercury 4.0: From Visualization to Analysis, Design and Prediction. *J. Appl. Crystallogr.* **2020**, *53*, 226–235.
(46) Huelsenbeck, L.; Luo, H.; Verma, P.; Dane, J.; Ho, R.; Beyer, E.; Hall, H.; Geise, G. M.; Giri, G. Generalized Approach for Rapid Aqueous MOF Synthesis by Controlling Solution pH. *Cryst. Growth Des.* **2020**, *20* (10), 6787–6795.
(47) Usman, K. A. S.; Maina, J. W.; Seyedin, S.; Conato, M. T.; Payawan, L. M.; Dumée, L. F.; Razal, J. M. Downsizing Metal–Organic Frameworks by Bottom-up and Top-down Methods. *NPG Asia Mater.* **2020**, *12* (1), 58.
(48) Patterson, A. L. The Scherrer Formula for X-Ray Particle Size Determination. *Phys. Rev.* **1939**, *56* (10), 978–982.
(49) DeStefano, M. R.; Islamoglu, T.; Garibay, S. J.; Hupp, J. T.; Farha, O. K. Room-Temperature Synthesis of UiO-66 and Thermal Modulation of Densities of Defect Sites. *Chem. Mater.* **2017**, *29* (3), 1357–1361.
(50) Chernikova, V.; Yassine, O.; Shekhah, O.; Eddaoudi, M.; Salama, K. N. Highly Sensitive and Selective SO_2 MOF Sensor: The Integration of MFM-300 MOF as a Sensitive Layer on a Capacitive Interdigitated Electrode. *J. Mater. Chem. A* **2018**, *6* (14), 5550–5554.
(51) Yu, Y.; Wang, Y.; Xu, H.; Lu, J.; Wang, H.; Li, D.; Dou, J.; Li, Y.; Wang, S. Dual-Responsive Luminescent Sensors Based on Two Cd-MOFs: Rare Enhancement toward acac and Quenching toward $Cr_2O_7^{2-}$. *CrystEngComm* **2020**, *22* (22), 3759–3767.
(52) Dighe, A. V.; Huelsenbeck, L.; Bhawnani, R. R.; Verma, P.; Stone, K. H.; Singh, M. R.; Giri, G. Autocatalysis and Oriented Attachment Direct the Synthesis of a Metal-Organic Framework. *J. Am. Chem. Soc.* **2022**, *2* (2), 453–462.
(53) Webber, T. E.; Desai, S. P.; Combs, R. L.; Bingham, S.; Lu, C. C.; Penn, R. L. Size Control of the MOF NU-1000 through Manipulation of the Modulator/Linker Competition. *Cryst. Growth Des.*

2020, *20* (5), 2965–2972.
(54) Ifraemov, R.; Mukhopadhyay, S.; Hod, I. Photo-Assisted Electrochemical CO_2 Reduction to CH_4 Using a Co-Porphyrin-Based Metal–Organic Framework. *Sol. RRL* **2023**, *7*, 2201068.
(55) Hooe, S. L.; Dressel, J. M.; Dickie, D. A.; Machan, C. W. Highly Efficient Electrocatalytic Reduction of CO_2 to CO by a Molecular Chromium Complex. *ACS Catal.* **2020**, *10* (2), 1146–1151.

Chapter 4 Understanding the Effects of Interactions Between Polymers and Metal–Organic Frameworks (MOFs) on Polymer-MOF Composite Gel Formation

4.1 Abstract

Polymer-metal–organic framework (MOF) composite gels have shown great potential in dye adsorption, wound healing, and separation. The synergistic interactions between polymers and MOFs can render composite gels with superior properties compared to their individual components. However, these interactions can also detract from the intended properties of the composite gels. For example, polymers containing carboxylic acid groups can reduce the crystallinity of MOFs within composite gels compared to pristine MOFs. Similarly, MOF formation can consume cross-linking sites for polymers and reduce cross-linking density in the composite gels. Therefore, we need to understand the effects of molecular details of polymers and MOFs on the properties of the resulting polymer-MOF composite gel. In this study, we use polymers with varying density of functional groups (i.e., carboxylic acids, hydroxyl groups, or neither) to make composite gels. We find that polymers with carboxylic acid groups either inhibit or disrupt MOF formation within composite gels. On the other hand, polymers with hydroxyl groups minimally affects the MOF crystallization with composite gels. Surprisingly, we discover an exciting possibility of polymer entrapment inside MOF pores and this polymer entrapment facilitates gelation. In the end, we show the generalizability of the synthetic procedure by making composite gel with different MOFs. The synthesis protocol developed here can be extended to a variety of polymers and MOFs to create a library of polymer-MOF composite gels for studying the release of peptides and proteins.

4.2 Introduction

Metal organic frameworks (MOFs), crystals in which organic linkers bridge metal ions/clusters,[1–10] can be integrated with polymers to create polymer-MOF composite gels that advance capabilities in optoelectronics,[11,12] wound healing,[13–16] and separations.[17–23] The functionality and versatility of these composite materials arises from synergistic interactions between polymers and MOFs that can enhance processability, sorptive capacity, and mechanical stability of the resultant polymer-MOF composite gels. For example, forming HKUST-1 MOFs within bentonite clay-cross-linked poly(vinyl alcohol) networks furnished 3D-printable MOF-laden inks.[24] In another example, synthesizing MOF-808 within metal-cross linked alginate gels increased methylene blue sorption by an order of magnitude compared to the alginate gels alone.[22] Additionally, synthesis of ZIF-8 within a gelatin matrix enhanced the storage modulus of the composite gels (5x) compared to the gelatin alone.[25] While interactions between MOFs and polymers that facilitate composite gel formation are quite beneficial in these examples, polymer-MOF interactions can also detract from the intended properties of composite gels.

MOF formation requires coordination of organic linkers to metal ions/clusters, and gel formation generally relies on cross-linking of polymer chains by the same metal ions/clusters. Therefore, this competition between the organic linker and polymer for binding the metal ions/clusters can disrupt MOF crystallization in composite gels. For example, synthesizing MOF-808 within Zr^{4+}-cross-linked alginate gels yielded composite gels with lower crystallinity than MOF-808 particles formed in the absence of alginate.[22] It is in turn possible that this competition between polymers and MOFs for binding the metal ions/clusters reduces cross-link density in the composite gels.[23] To gain control over polymer-MOF composite gel properties, we must further understand this competition.

To date, many polymer-MOF composite gels created in literature contain carboxylic acid (–COOH)-toting polymers, such as alginate.[11,19,21,23,26,27] As many MOFs contain (–COOH)-

functionalized organic linkers, the (–COOH) groups on the polymer are particularly likely to compete with those on the organic linker to bind the metal ions/clusters. Using polymers with functional groups that more weakly bind metal (e.g., amines ($–NH_2$) or alcohols (–OH)) can permit crystalline MOF formation without preventing gelation. For example, four different MOFs were formed within chitosan gels, which contain hydroxyl (–OH) and amine ($–NH_2$) groups, producing composites with similar crystallinity to the MOFs alone.[18] Encouragingly, this suggests that polymer molecular details can tune the MOF formation properties and the polymer-MOF interactions and, by extension, the properties of the resulting composites.

Here, we investigate how the molecular details of polymers and MOFs affect the formation, gelation behavior, crystallinity, and sorption characteristics of their composite gels. Specifically, for these studies we form composite gels using polymers with different types and densities of functional groups (i.e., carboxylic acids, hydroxyl groups, or neither) as well as a range of Zr-based MOFs.

4.3 Experimental Section

Materials

Zirconium (IV) propoxide solution (70 wt% in 1-propanol, $Zr(O\textit{n}Pr)_4$), *N*,*N*-dimethylformamide (DMF, ≥99.8%), poly(vinyl alcohol) (PVA, M_w ~ 146000 – 186000 g/mol & 99%+ hydrolyzed, M_w ~ 31000 – 50000 g/mol & 98-99% hydrolyzed, and M_w ~ 9000 – 10000 g/mol & 80% hydrolyzed), poly(ethylene oxide) (PEO, M_v ~ 100000 g/mol), poly(acrylic acid) (PAA, M_w ~ 1033000 g/mol), terephthalic acid (H_2BDC, 98%), 2-aminoterephthalic acid (H_2ATA, 99%), biphenyl-4,4'-dicarboxylic acid (BPDC, 97%), 4,4′,4″,4‴-(porphine-5,10,15,20-tetrayl)tetrakis(benzoic acid) (TCPP, dye content 75%), dimethyl sulfoxide-d_6 (deuteration ≥ 99.8%), acetic acid (≥99.7%), 4-ethoxycarbonylphenylboronic acid (95%), dioxane (99%), 1,3,6,8-tetrabromopyrene (97%), potassium phosphate tribasic (98%), tetrakis-

(triphenylphosphine)palladium(0) (99%), potassium hydroxide (90%), chloroform (99%), dichloromethane (99.8%), and methylene blue (Dye content, >82%) were purchased from Sigma Aldrich. Dimethyl sulfoxide (DMSO, ≥99.9%), methanol (99.9%), and hydrochloric acid (HCl, 36.5−38%) were purchased from Fisher Scientific. Poly (acrylamide-*co*-acrylic acid) (PAAA, AMD: AA = 9:1, M_w ~ 210000 g/mol) was purchased from Polymer Source Inc. 4,4',4",4'"-(pyrene-1,3,6,8-tetrayl)tetrabenzoic acid (H_4TBAPy) linker was synthesized following a previously published procedure.[28]

Synthesis of Zr-oxo clusters in DMSO:

Synthetic conditions were adapted from a previously published procedure.[29] In a 20 mL glass vial, Zr(O*n*Pr)$_4$ (0.355 mL, 0.8 mmol) and acetic acid (4.00 mL, 70 mmol) were added to 7 mL of solvent (DMSO). The solution was sonicated for 10 min, placed in an oven at 130 ºC for 2 h, and cooled to room temperature for use in further synthesis.

Synthesis of UiO-66 powder in DMSO:

Into a Zr-oxo cluster solution in DMSO (10.0 mL, 0.7 mmol of Zr), H_2BDC (120 mg, 0.7 mmol) was added and dissolved using sonication. The solution was stirred for 24 h at room temperature. The particles produced from this synthesis were not isolatable by centrifugation, and therefore were isolated by dialysis against deionized water in a 3.5 kDa molecular weight cut-off regenerated cellulose dialysis membrane (Spectra/Por). Each water change was allowed to equilibrate for ≥3h. After dialysis, the UiO-66 particles sediment in DI water and DI water was dried at room temperature to obtain UiO-66 powder.

Synthesis of polymer-UiO-66 composite gels

In a 20 mL glass vial, 220 mg of polymer (PAA, PAAA, PVA, or PEO) was dissolved in DMSO (5.00 mL) by putting the mixture on a hot plate heated at 120 °C and stirring it continuously until polymer dissolves. Then the polymer solution in DMSO was allowed to cool to room

temperature, where it remained soluble, and H_2BDC (120 mg) was dissolved in the polymer solution. Then Zr-oxo cluster solution (5.00 mL in DMSO) was added to polymer – H_2BDC solution (5.00 mL in DMSO) and the mixture shaken for 1 min and allowed to stand at room temperature for 24 h. After 24 h, the mixture formed a polymer-UiO-66 composite gel as suggested by the inversion test.

Synthesis of polymer – Zr-oxo gels:

In a 20 mL glass vial, 220 mg of polymer (PAA, PAAA, PVA, or PEO) was dissolved in DMSO (5.00 mL) by putting the mixture on a hot plate heated at 120 ºC and stirring it continuously. Then the polymer solution in DMSO was allowed to cool to room temperature, where it remained soluble, and Zr-oxo cluster solution (5.00 mL in DMSO) was added to the polymer solution (5.00 mL in DMSO) and the mixture shaken for 1 min and allowed to stand at room temperature for 24 h. After 24 h, the mixture formed a polymer – Zr-oxo gel as suggested by the inversion test.

Synthesis of polymer-UiO-66 physical mixture:

In a 20 mL glass vial, 220 mg of polymer (PAA, PAAA, PVA, or PEO) was dissolved in DMSO (5.00 mL) by putting the mixture on a hot plate heated at 120 °C and stirring it continuously. Then the polymer solution in DMSO was allowed to cool to room temperature, where it remained soluble, and UiO-66 powder (95 mg, synthesized in DMSO) was added to the polymer solution and the mixture shaken for 1 min and allowed to stand at room temperature for 24 h. After 24 h, the polymer-UiO-66 physical mixture was obtained.

Synthesis of PVA – Zr-MOFs composite gels:

In a 20 mL glass vial, 220 mg of PVA was dissolved in DMSO (5.00 mL) by putting the mixture on a hot plate heated at 120 °C and stirring it continuously. Then the PVA solution in DMSO was allowed to cool to room temperature, where it remained soluble, and organic linkers (**Table 4.1**) were dissolved into the PVA solution. After that, Zr-oxo clusters solution (5.00 mL in DMSO) was

added to PVA – linker solution (5.00 mL) and the mixture shaken for 1 min and allowed to stand at room temperature for 24 h. After 24 h, the mixture formed a PVA-Zr-MOF composite gels as suggested by the inversion test. The linker amount was determine based on previously published syntheses and the references are mentioned in **Table 4.1**.

Table 4.1. Organic linkers used in the synthesis of PVA-Zr-MOFs composite gels

Composite gel	Organic linker used to obtain the composite gel	Amount of organic linker used in the synthesis
PVA-UiO-66-NH_2,[29]	H_2ATA	130 mg
PVA-NU-901,[30]	H_4TBAPy	50 mg
PVA-UiO-67,[29]	BPDC	175 mg
PVA-MOF-525,[30]	TCPP	60 mg

Solvent Exchange from DMSO to Water:

The gels were dialyzed against 4 changes of deionized water in a 3.5 kDa molecular weight cut-off regenerated cellulose dialysis membrane (Spectra/Por). Each water change was allowed to equilibrate for ≥4 h.

Characterization:

Grazing incidence X-ray Diffraction (GIXD):

GIXD experiments were performed at beamline 11-3 of the Stanford Synchrotron Radiation Lightsource at SLAC National Accelerator Laboratory with a fixed beam energy of 12.7 keV. The two-dimensional (2D) GIXD diffraction patterns were recorded using a Rayonix MX225 CCD area detector. Samples were put on a glass substrate to collect the 2D diffraction patterns. The sample-to-detector distance was 316 mm. Fast Azimuthal Integration (pyFAI) using Python was used to obtain 1D diffraction patterns from 2D GIXD diffraction patterns.

Scanning Electron Microscopy (SEM):

The organogels were dried at room temperature on a glass slide prior to characterization. The dry gel was sputter coated with a layer of Au/Pd using a Gatan 682 Precision Etching and Polishing System (PECS). SEM Images of the dry gel were obtained using a FEI quanta 650 field-emission secondary electron microscope. The accelerating voltage of the primary beam was kept between 5 kV and 15 kV, and the spot size was kept below 4.

Thermogravimetric analysis (TGA):

TGA was performed using TA instruments Q50 thermogravimetric analyzer. The DMSO-swollen gels and the hydrogel samples were dried at room temperature, the former in a fume hood, for 48-72 h before analysis. The sample gas was air (flowrate = 60 mL/min) and the balance gas was N_2 (flowrate = 40 mL/min). Samples were heated from room temperature to 1000 ºC at a rate of 10 ºC/min.

4.4 Result and Discussion

We first studied the impact of polymers on MOF formation, and the impact of MOF formation on polymer cross-linking. To probe the role of polymer chemistry in MOF formation, we formed MOFs in the presence and absence of poly(acrylic acid) (PAA), poly(acrylic acid-*co*-acrylamide) (PAAA), poly(vinyl alcohol) (PVA), and poly(ethylene glycol) (PEG), and we compared the resulting MOF crystallinity. We note that aside from PEG, these polymers are all simple hydrocarbon chains with functional groups pendent to every other carbon, allowing us to isolate the effects of these functional groups. In turn, to investigate the extent to which MOF formation plays a role in polymer cross-linking, we compared the gelation behavior of metal cross-linked polymers (no organic MOF linker) to that of the polymer-MOF composites. We selected the prototypical MOF UiO-66, featuring zirconium (Zr)-oxide (Zr-oxo) clusters linked with benzene dicarboxylic acid (H_2BDC), for these comparisons. Previously finding that pre-forming Zr-oxo

clusters prior to adding linker accelerates MOF formation,[29,31] we first synthesized the clusters by dissolving zirconium propoxide (70 wt% in 1-propanol) and acetic acid modulator in DMSO followed by heating at 130 °C for 2 h. Then, as shown in **Figure 4.1a**, we added the H_2BDC linker to the Zr-oxo cluster solution and stirred at room temperature (RT) for 24 h to form UiO-66. As is typical with UiO-66 formation, the solution turned white within 4-6 h, indicative of solid formation (**Figure A4.1**). We isolated the UiO-66 powder by dialyzing the suspension against DI water, followed by drying the particles at RT in ambient conditions. Scanning electron microscopy (SEM) images of the MOF powder revealed spherical particles ~30 to 80 nm in diameter, typical of rapid MOF formation,[31] (**Figure A4.2**). Grazing incidence X-ray diffraction (GIXD) from the powder shows that diffraction peaks corresponding to scattering from the (111) and (200) planes of UiO-66 peaks are obtained, confirming UiO-66 formation (**Figure 4.1b**). From the GIXD pattern, we used the Scherrer equation to calculate the coherence length of UiO-66, reflective of the length scale over which crystalline order persists. Synthesizing UiO-66 in DMSO yields a coherence length of 40 nm (**Table A4.1**).

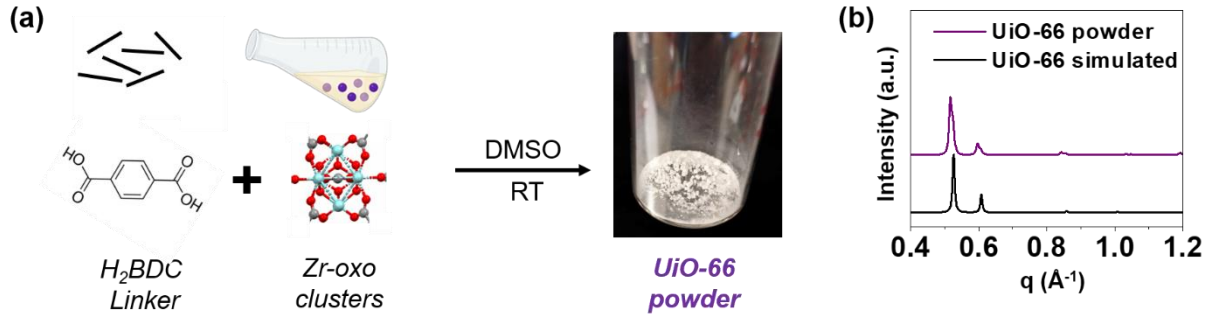

Figure 4.1. *(a) Synthesis process to make UiO-66 powder in dimethyl sulfoxide (DMSO). Benzene dicarboxylic acid (H_2BDC) powder is added to Zr-oxo cluster solution to make UiO-66 at RT. For Zr-oxo cluster structure, Zr, C, and O have been represented in cyan, grey, and red, respectively. (b) Grazing incidence X-ray diffraction (GIXD) pattern of UiO-66 powder compared with simulated UiO-66 pattern, thus confirming the formation of UiO-66.*

4.4.1 Poly(acrylic acid) (PAA)-UiO-66 gel

Anticipating that polymers with carboxylic acid groups would compete most strongly with the carboxylic acid-containing linkers for binding the Zr-oxo metal clusters, we started our study

by attempting to form PAA-UiO-66 composite gels. Specifically, we added a solution of Zr-oxo clusters to a solution containing H_2BDC linker and 2 wt.% PAA (1,033,000 Da) in DMSO. The high molecular weight of PAA was selected to enable the polymer chains to bridge multiple MOF particles. After 24 h at RT, inversion of the vial revealed the mixture to form a self-supporting gel (**Figure 4.2b).** Yet, as the gel was transparent, and since rapid UiO-66 formation should produce particles that give the gel a white color, we suspected limited-to-no UiO-66 formation within the gel. Suspecting that gelation was due to Zr-oxo clusters cross-linking PAA chains, we added a solution of Zr-oxo clusters to a PAA solution, which indeed produced a self-supporting PAA-Zr-oxo gel (**Figure 4.2c**). Consistent with the lack of MOF linker in these polymer-Zr-oxo gels, the GIXD pattern did not show scattering from planes associated with the UiO-66 crystal lattice (**Figure 4.2d)** and the SEM images contained no spherical particles (**Figure A4.3**).

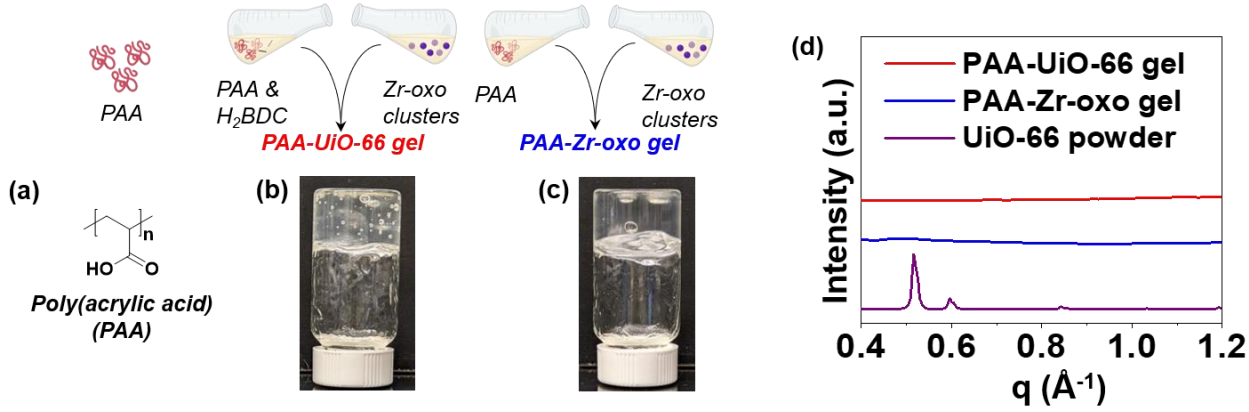

Figure 4.2. *(a) Chemical structure of poly(acrylic acid) (PAA). Inversion test of (b) PAA-UiO-66 gel and (c) PAA-Zr-oxo gel, suggesting gelation. (d) Grazing incidence X-ray diffraction (GIXD) pattern of PAA-UiO-66 gel compared with UiO-66 powder diffraction pattern, thus confirming no UiO-66 formation within the gel.*

Since MOF formation does not occur in the presence of PAA, presumably due to PAA outcompeting the H_2BDC linker for binding the Zr-oxo clusters, we next sought to form composites by adding pre-formed UiO-66 to PAA. Yet, we did not observe gelation of these physical mixtures of MOF and polymer (**Figure A4.4**), a result that we ascribe to the lower availability of Zr-oxo clusters needed for polymer cross-linking within the pre-formed MOFs. Therefore, formation of

MOF in the presence of polymer seems to be important for availing metal clusters for polymer cross-linking. As PAA inhibited UiO-66 formation, we reasoned that lowering the (–COOH) density on the polymer would permit MOF formation *simultaneously* with gelation.

4.4.2 Poly(acrylamide-*co*-acrylic acid) (PAAA)-UiO-66 composite gel

We next attempted composite gel formation with UiO-66 and PAAA, a copolymer containing just 10% acrylic acid groups randomly dispersed among acrylamide units with M_w ~ 210,000 g/mol (**Figure 4.3a**). Despite the lower density of carboxylic acids, mixtures of PAAA and Zr-oxo still form gels in the absence of linker (**Figure 4.3c**). In the presence of linker, we observed the formation of an opaque, self-supporting gel (**Figure 4.3b**). The turbid white color of the gel indicated UiO-66 particle formation within the gel, which GIXD patterns (**Figure 4.3d**) and SEM confirmed (**Figure A4.5**). While lowering carboxylic acid density within the polymer permitted simultaneous MOF formation and gelation, the coherence length of UiO-66 formed within the composite gel was lower (26 nm) than that of UiO-66 formed in the absence of polymer (40 nm). Therefore, despite its lower (-COOH) content, PAAA still disrupts MOF crystallinity.

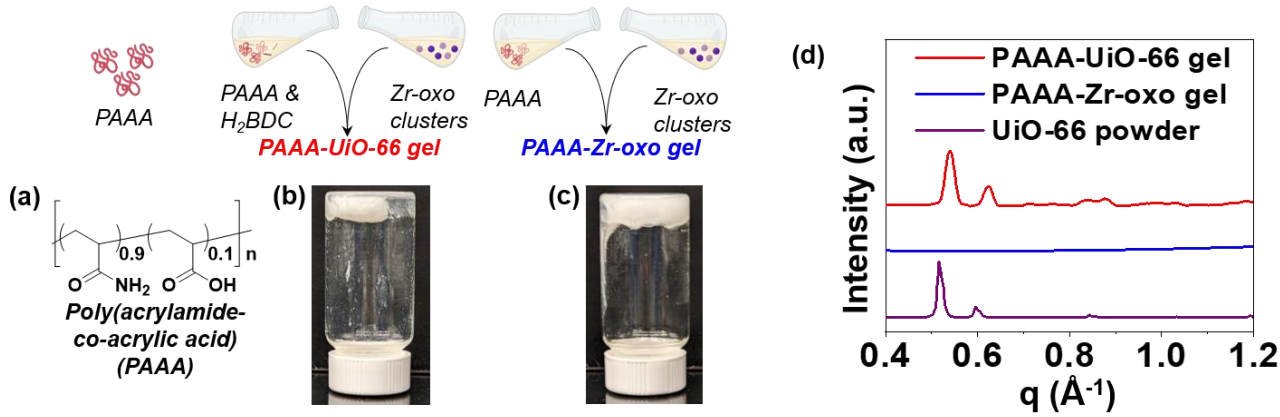

Figure 4.3. *(a) Chemical structure of poly(acrylamide-co-acrylic acid) (PAAA). Inversion test of (b) PAAA-UiO-66 gel and (c) PAAA-Zr-oxo gel, suggesting gelation. (d) Grazing incidence X-ray diffraction (GIXD) pattern of PAAA-UiO-66 gel compared with UiO-66 powder diffraction pattern, thus confirming UiO-66 formation within the gel.*

4.4.3 Poly(vinyl alcohol) (PVA)-UiO-66 composite gel

As hydroxyl groups (–OH) interact less strongly with Zr-oxo clusters compared to (-COOH) groups,[32] we expected that forming UiO-66 in the presence of PVA (146000-186000 g/mol, **Figure 4.4a**) would furnish composite gels with more crystalline MOF than PAAA. Even though PVA was expected to less strongly bind Zr-oxo clusters, adding a Zr-oxo cluster solution to a PVA solution in the absence of H_2BDC linker yielded a self-supporting PVA-Zr-oxo gel (**Figure 4.4c**). Addition of Zr-oxo solution to a mixture of PVA and H_2BDC resulted in a self-supporting gel (**Figure 4.4b**). SEM (**Figure A4.6**) and GIXD (**Figure 4.4d)** revealed UiO-66 particles within the composite gels having a similar coherence length (44 nm) to UiO-66 particles formed in the absence of polymer (40 nm). Relative to the composites formed with PAAA featuring a low density of carboxylic acids (coherence length = 26 nm), composites formed in the presence of PVA contained more crystalline MOFs (44 nm).

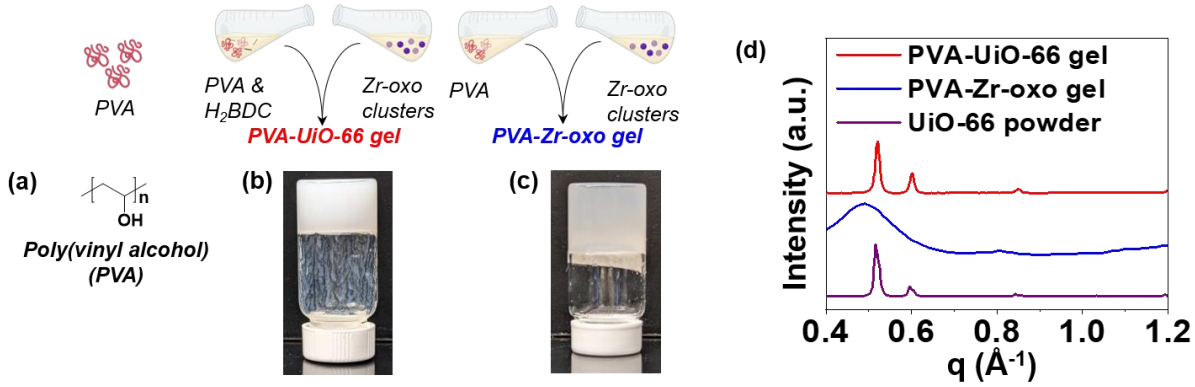

Figure 4.4. *(a) Chemical structure of poly(vinyl alcohol) (PVA). Inversion test of (b) PVA-UiO-66 gel and (c) PVA-Zr-oxo gel, suggesting gelation. (d) Grazing incidence X-ray diffraction (GIXD) pattern of PVA-UiO-66 gel compared with UiO-66 powder diffraction pattern, thus confirming UiO-66 formation within the gel.*

Given that PVA furnished more crystalline UiO-66 within gel composites compared to the carboxylate-containing polymers, we next sought to determine the PVA molecular weight and concentration needed to form gels. After varying the concentration of PVA (M_W ~ 146000-186000

g/mol) used to form PVA-UiO-66 composites from 0.1 to 3.0 wt%, we obtained self-supporting gels at or above 2.0 wt% (**Figure 4.5**).

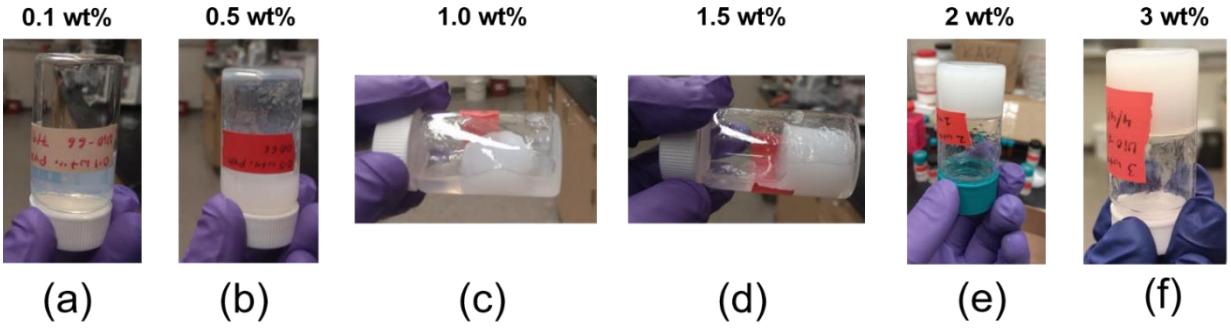

***Figure 4.5**. Inversion tests of PVA (146000-186000 g/mol) - UiO-66 formulations as a function of polymer concentration: (a) 0.1; (b) 0.5; (c) 1.0; (d) 1.5; (e) 2; and (f) 3 wt% PVA. The study shows that a critical PVA concentration (1.5-2 wt%) is required to induce gelation.*

Next, we varied the chain length of PVA to observe its effect of gelation. We used short PVA chains (M_W ~ 9000-10000 g/mol) and intermediate PVA chains (M_W ~ 31000-50000 g/mol) to synthesize PVA-UiO-66 composite gels. Short PVA chains (M_W ~ 9000-10000 g/mol) do not form gels even at high concentrations of PVA as illustrated in **Figure 4.6** cross-linking of PVA chains might not be possible for such short chains. Conversely, intermediate PVA chains (M_W ~ 31000-50000 g/mol) render gels at 3.0 wt% and above (**Figure 4.7**). Together, these results suggest that polymer chains must be long enough or at a high enough concentration in solution to bridge multiple MOF particles (or Zr-oxo clusters) for gelation to occur (**Figure 4.8**).

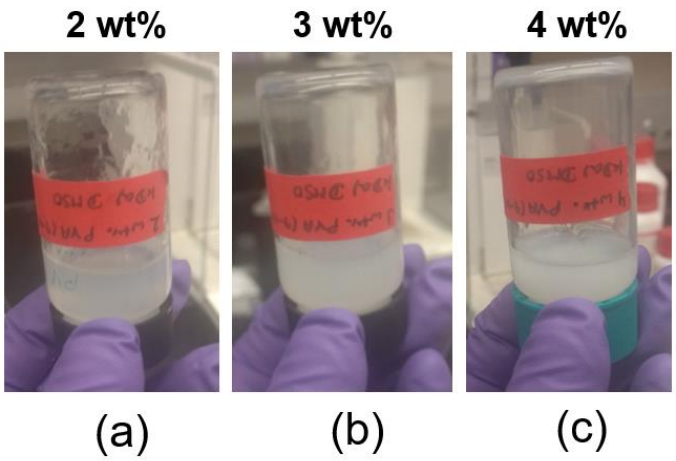

Figure 4.6. *Inversion test of PVA (9000-10000 g/mol) - UiO-66 formulations at (a) 2, (b) 3, and (c) 4 wt% PVA. The study shows no gelation even at 4 wt% PVA concentration using this low molecular weight polymer.*

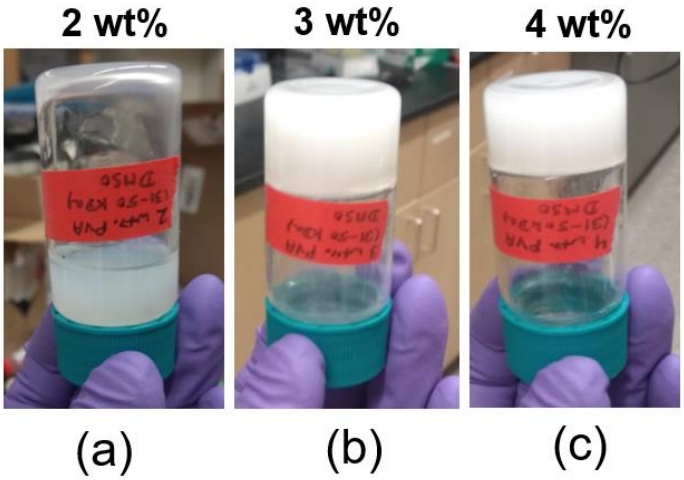

Figure 4.7. *Inversion tests of PVA (31000-50000 g/mol) – UiO-66 formulations at (a) 2, (b) 3, and (c) 4 wt% PVA. The study shows that for this lower molecular weight PVA, gelation occurs at or above 3 wt% PVA concentration, slightly higher than that needed for gelation using the higher molecular weight PVA (146000-186000 g/mol).*

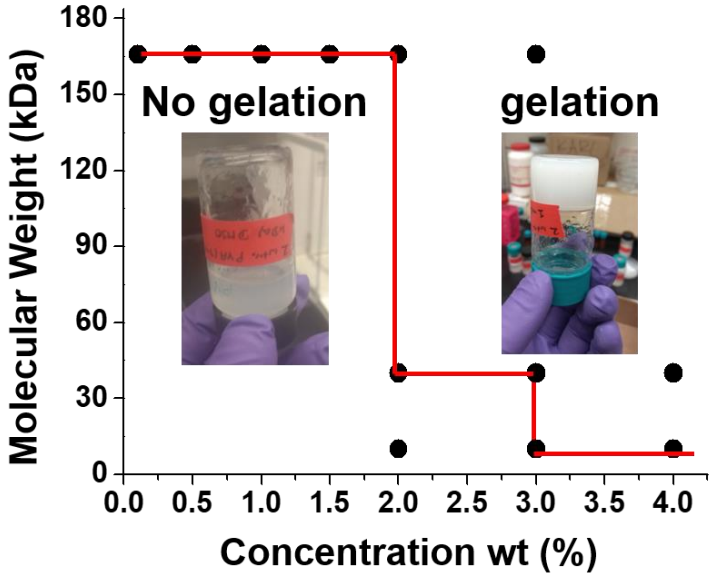

Figure 4.8. *Phase diagram of PVA-UiO-66 formulations showing regions where gelation does not or does occur.*

4.4.4 Poly(ethylene glycol) (PEG)-UiO-66 composite gel

We further reduced the interaction between polymers and Zr-oxo clusters by using poly(ethylene glycol) (PEG, M_v > 100000 g/mol) (**Figure 4.9a**), which does not have metal binding functional groups like (-COOH) and (-OH) on its backbone. Unlike carboxylic acid- and hydroxyl-toting polymers, mixing PEG with Zr-oxo clusters does not form gels (**Figure 4.9c**). Adding a solution of Zr-oxo clusters to a mixture of PEG and H_2BDC linker in DMSO, which yielded a self-supporting gel (**Figure 4.9b**). SEM (**Figure A4.7**) and GIXD (**Figure 4.9d**) revealed the presence of UiO-66 particles with a comparable, yet slightly lower coherence length (32 nm) to UiO-66 synthesized in the absence of polymer (40 nm). Since Zr-oxo does not cross-link PEG, the observation of gelation during MOF formation suggests the exciting possibility that MOFs may cross-link polymers by physically entrapping them as they form.

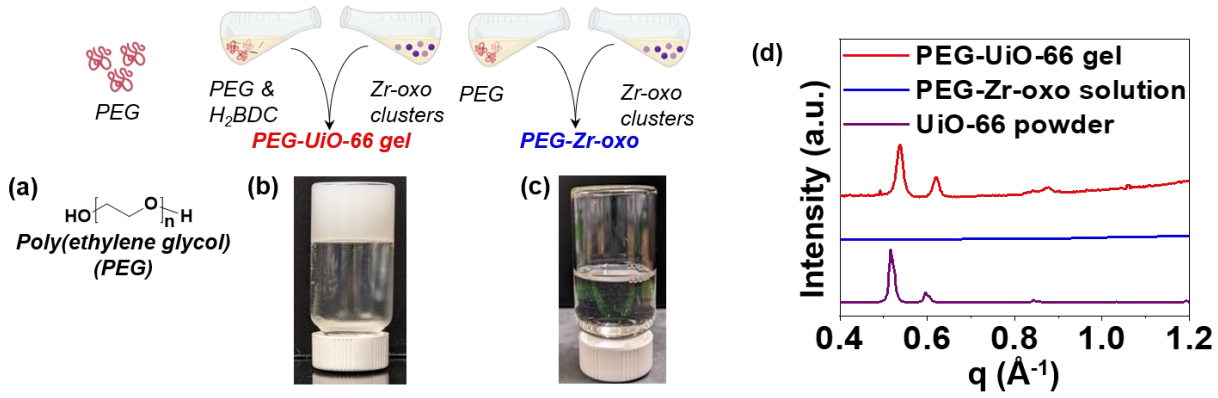

Figure 4.9. *(a) Chemical structure of poly(ethylene glycol) (PEG). Inversion test of (b) PEG-UiO-66 gel and (c) PEG-Zr-oxo gel, suggesting gelation for PEG-UiO-66 and not for PEG-Zr-oxo. (d) Grazing incidence X-ray diffraction (GIXD) pattern of PEG-UiO-66 gel compared with UiO-66 powder diffraction pattern, thus confirming UiO-66 formation within the gel.*

Wishing to further probe the possibility that MOFs are physically entrapping polymers, we compared the stability of PVA and PEG composite gels, since Zr-oxo can cross-link PVA, but not PEG chains. After heating both composites to 40 °C for 24 h, the PEG composite gel collapsed (**Figure 4.10a**); however, the PVA composite gel remained intact (**Figure 4.10b**). We hypothesize that heating facilitates the movement of PEG chains out of the MOF pores and gel collapses. This indicates that PEG chains are entrapped within UiO-66 pores to facilitate gelation.

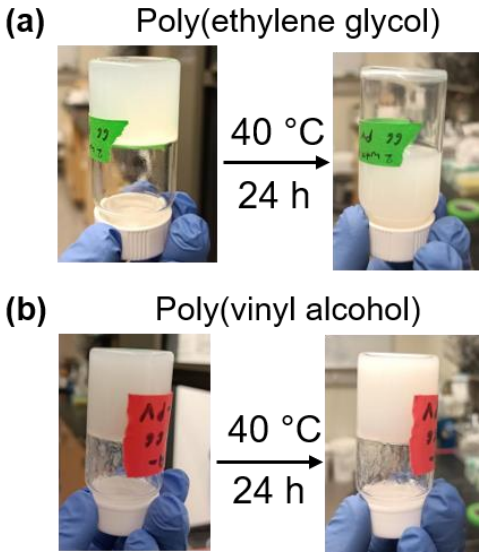

Figure 4.10. *Role of polymer chain entrapment on (a) PEG-UiO-66 and (b) PVA-UiO-66 composite gels. Inversion test results of PEG-UiO-66 and PVA-UiO-66 composite gels before and after heating at 40 °C for 24 h.*

4.4.5 Extending PVA-MOF composite gel synthesis to other Zr-based MOFs

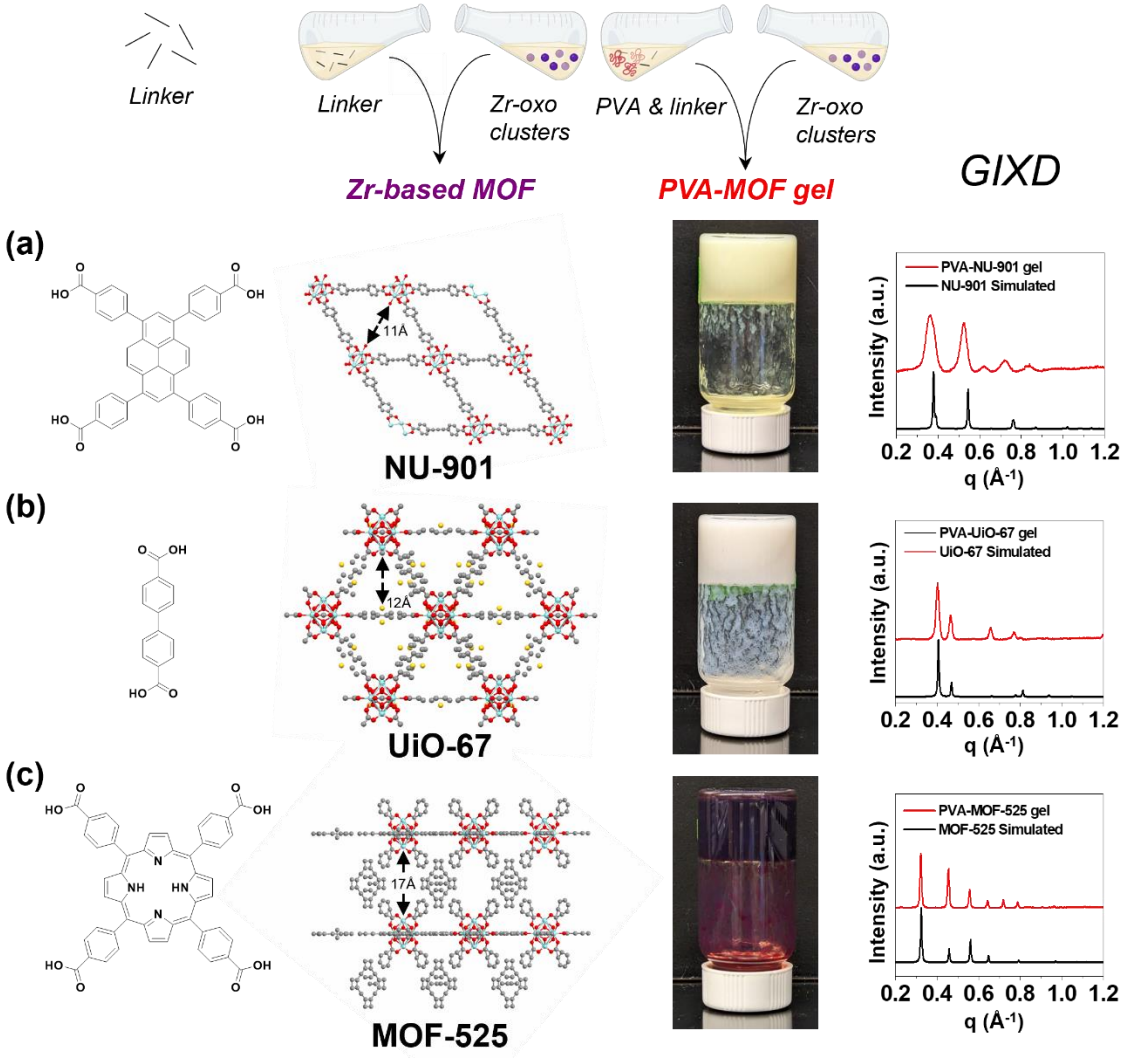

Figure 4.11. *Extension of the composite gel synthesis process to different Zr-based MOFs. Formation and properties of gel composites formed from: (a) NU-901, with 4,4',4'',4'''-(1,3,6,8-pyrenetetrayl) tetrakis-benzoic acid) (H_4TBAPy) linker; (b) UiO-67, with biphenyl-4,4'-dicarboxylic acid (BPDC) linker; and (c) MOF-525, with tetrakis (4-carboxyphenyl porphyrin (TCPP) linker. For each formulation, we show the organic linker used in the synthesis, the crystal structures of each MOF obtained from Mercury software,[37] composite gelation behavior via inversion tests, and grazing incidence X-ray diffraction (GIXD) patterns comparing the crystal structures of the MOFs formed in each composite gel to the simulated patterns for the corresponding MOFs. For crystal structures, Zr, C, and O have been represented in cyan, grey, and red, respectively.*

To determine the generalizability of the composite gel formation process, we attempted to form composite gels from PVA and other different Zr-oxo-based MOFs (UiO-66-NH_2,[33] NU-901,[34] UiO-67,[35] and MOF-525,[36]). We selected PVA as the polymer to add with these MOFs, as PVA

facilitated the formation of most crystalline UiO-66 within the composite gels. Just as in PVA-UiO-66 composite gel synthesis, we added a solution of Zr-oxo clusters to a solution containing PVA and the organic linkers, adjusting the ligand concentrations to achieve ligand:metal ratios commonly used for each MOF in the literature, (**Table 4.1**). All formulations produced self-supporting gels, and SEM images (**Figure A4.8-A4.10**) and GIXD patterns (**Figure 4.11a-c**) confirmed the presence of MOFs within the gels. The extra peaks appearing in the diffraction pattern could be due to the defects forming within the MOF crystals. Encouragingly, the examples presented here involving 3 different MOFs demonstrate that this composite gel formation process extends to different Zr-oxo based MOFs.

4.5 Conclusion

In conclusion, we demonstrated a generalizable one-step method to synthesize polymer-MOF composite gels with a range of polymers and Zr-based MOFs. Polymers containing (-COOH) and (-OH) metal-binding functional groups, such as PAA, PAAA, and PVA, interact with Zr-oxo clusters to induce gelation but also affect UiO-66 formation. We found that PAA, which contains (-COOH) groups only, outcompeted H_2BDC linker to bind Zr-oxo clusters and inhibited UiO-66 formation within the gel. Furthermore, PAAA, which contains just 10% (-COOH) groups compared to PAA, subdued the competition between polymers and linker to bind metal clusters and promoted UiO-66 formation within the gel, but with reduced crystallinity compared to the UiO-66 formed in the absence of polymer. On the other hand, using polymer containing (-OH) functional groups, such as PVA produced UiO-66 crystals within the gel with crystallinity similar to UiO-66 alone. Surprisingly, PEO, which interacts minimally with Zr-oxo clusters, also produce a gel during UiO-66 formation, suggesting the exciting possibility of polymer entrapment within UiO-66 pores. The formation of 4 other PVA-Zr-MOF gels highlights the robustness and versatility of the synthesis protocol developed here.

4.6 Appendix

Coherence length calculation:

Coherence length was calculated using the Scherrer equation,[38]

$$L = \frac{K * 2\pi}{\Delta q}$$

Where L is coherence length, Δq is the full width at half maximum (FWHM) of the most intense peak in the diffraction pattern, and K is a dimensionless shape factor that depends on the shape of the crystallites. For spherical particles, K = 0.93.

Table A4.1. **Coherence length of UiO-66 particles synthesized with and without polymers**

Sample name	Coherence length (nm)
UiO-66 particles	40
PAAA-UiO-66 composite gel	26
PVA-UiO-66 composite gel	44
PEG-UiO-66 composite gel	32

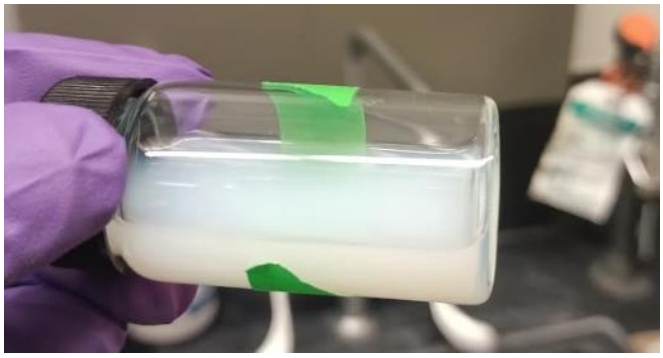

Figure A4.1*: Formation of UiO-66 particles in DMSO as evidenced by the solution turning white.*

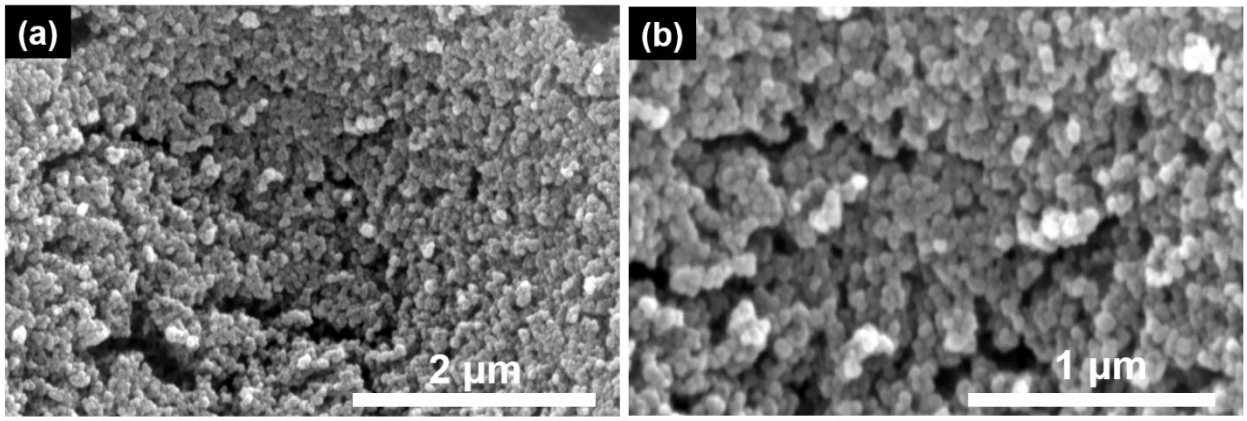

Figure A4.2*: (a), (b): High-magnification scanning electron microscopy (SEM) images of UiO-66 synthesized in DMSO show the formation of spherical particles.*

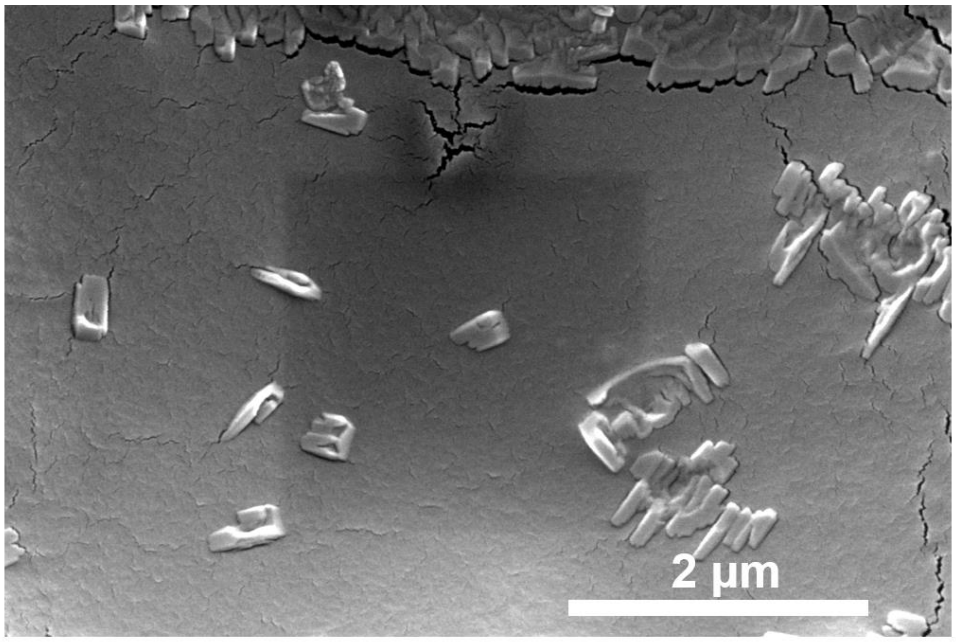

Figure A4.3*: High-magnification SEM image of PAA-UiO-66 gel shows no spherical particles such as those observed in* ***Figure A4.2*** *for UiO-66 particles synthesized in DMSO in the absence of PAA. The absence of spherical particles in the PAA-UiO-66 gels suggests no UiO-66 formation in the presence of PAA.*

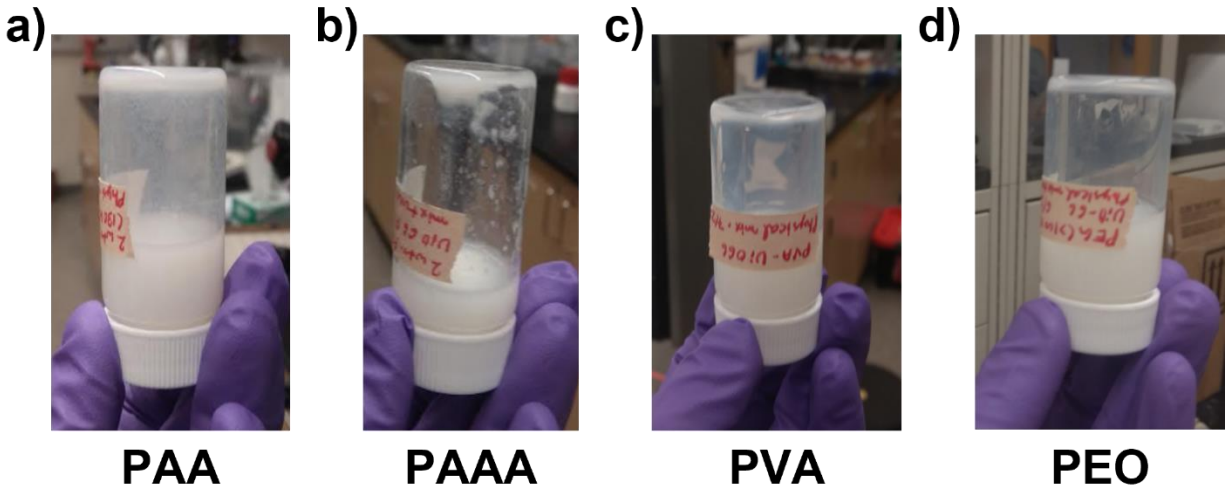

***Figure A4.4**: Inversion test results of physical mixtures of a) PAA and UiO-66, b) PAAA and UiO-66, c) PVA and UiO-66, and d) PEO and UiO-66 showing the absence of gelation when pre-formed MOFs are mixed with polymers.*

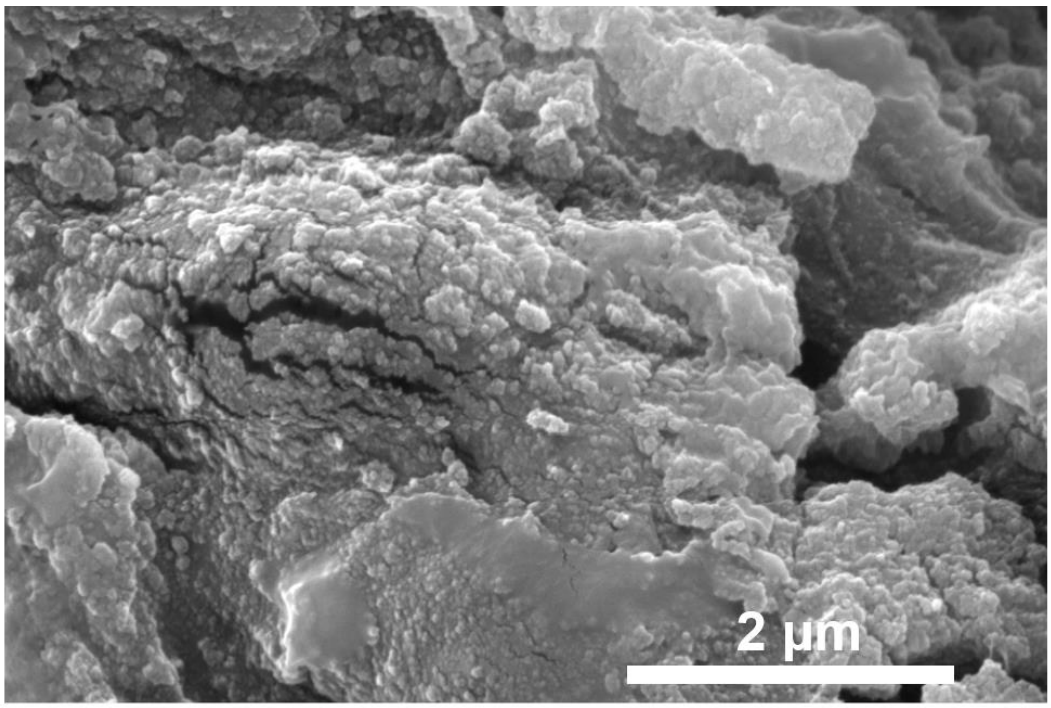

***Figure A4.5**: High-magnification SEM image of PAAA-UiO-66 composite gel showing the presence of spherical particles, suggesting the formation of UiO-66 in the presence of PAAA.*

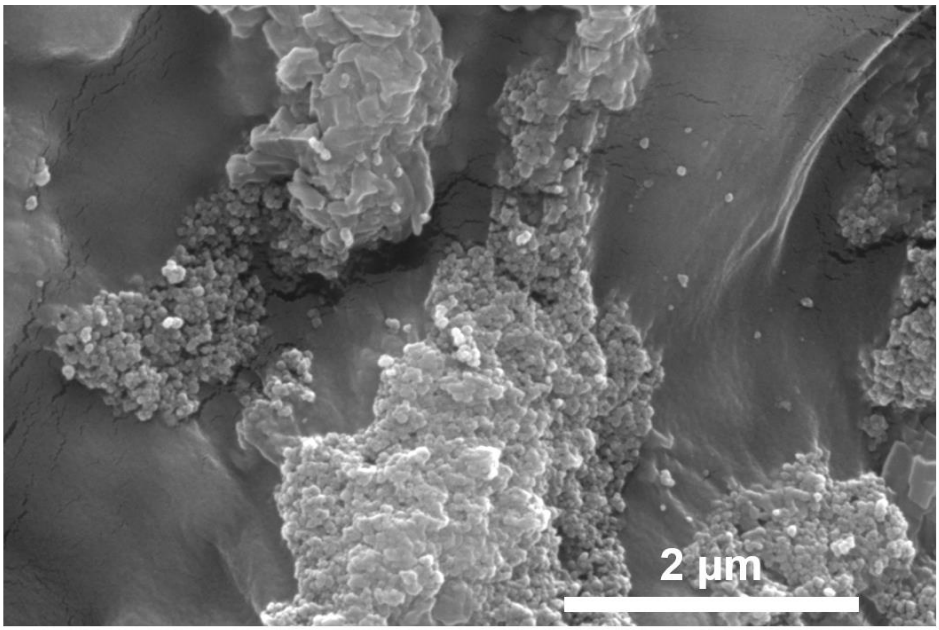

***Figure A4.6**: High-magnification SEM image of PVA-UiO-66 composite gel showing the presence of spherical particles, suggesting the formation of UiO-66 in the presence of PVA.*

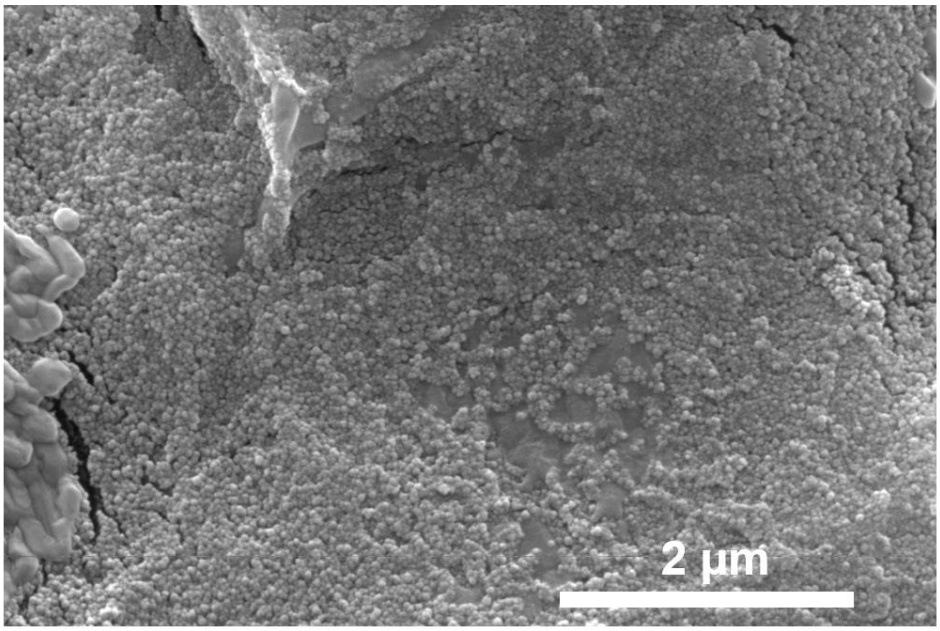

***Figure A4.7**: High-magnification SEM image of PEG-UiO-66 composite gel shows the presence of spherical particles, suggesting the formation of UiO-66 in the presence of PEG.*

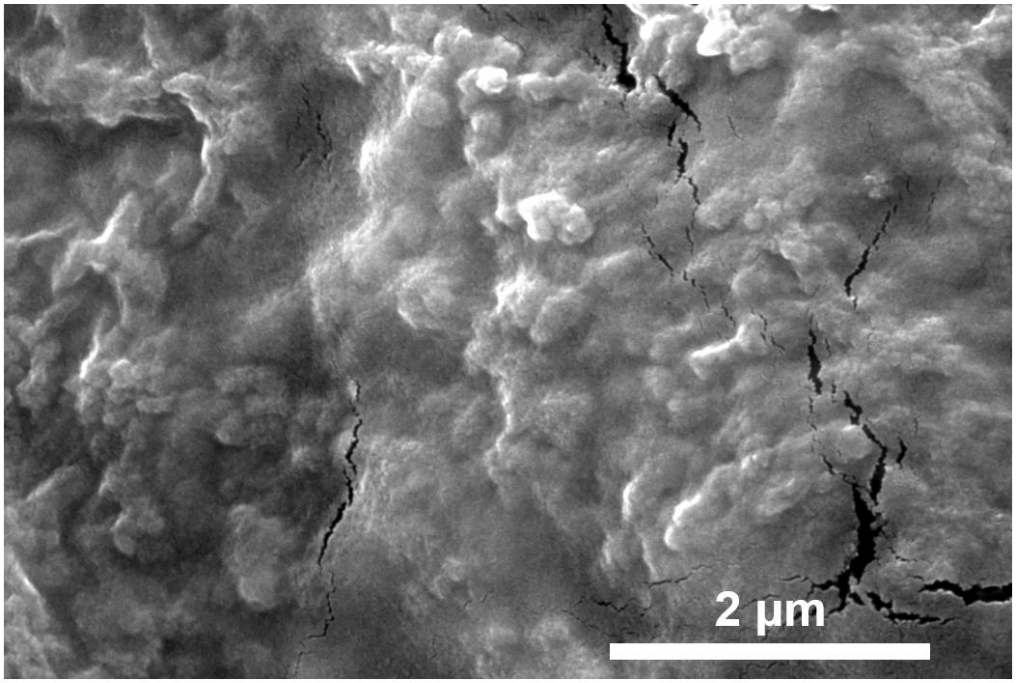

***Figure A4.8**: High-magnification SEM image of PVA-NU-901 composite gel shows the presence of spherical particles, suggesting the formation of NU-901 in the presence of PVA.*

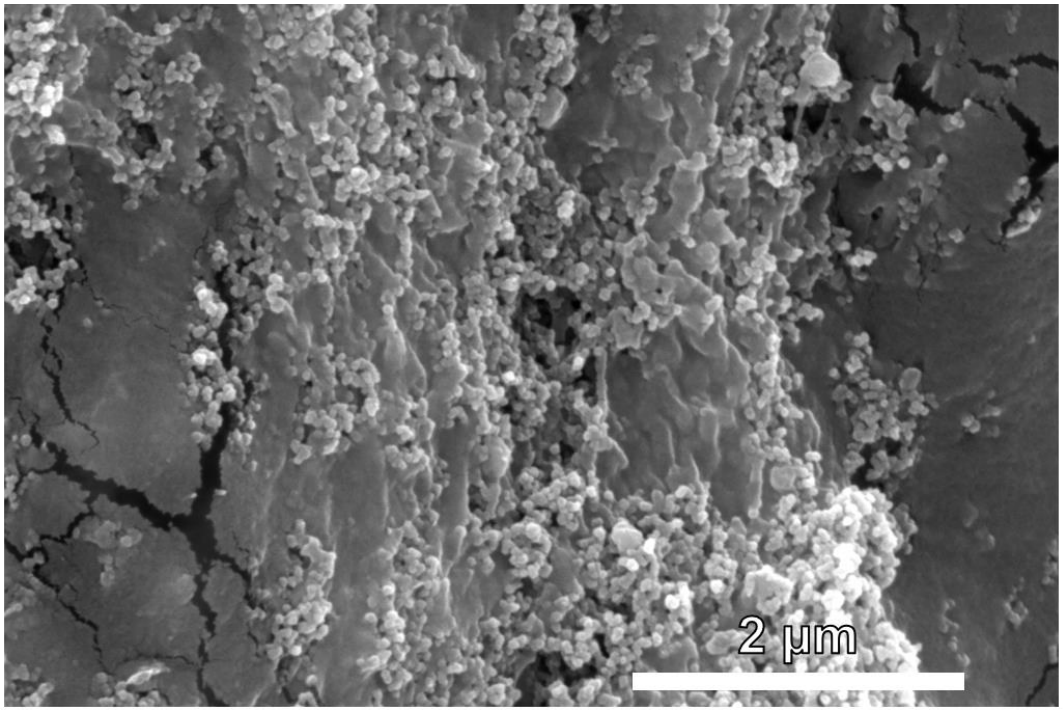

***Figure A4.9**: High-magnification SEM image of PVA-UiO-67 composite gel shows the presence of spherical particles, suggesting the formation of UiO-67 in the presence of PVA.*

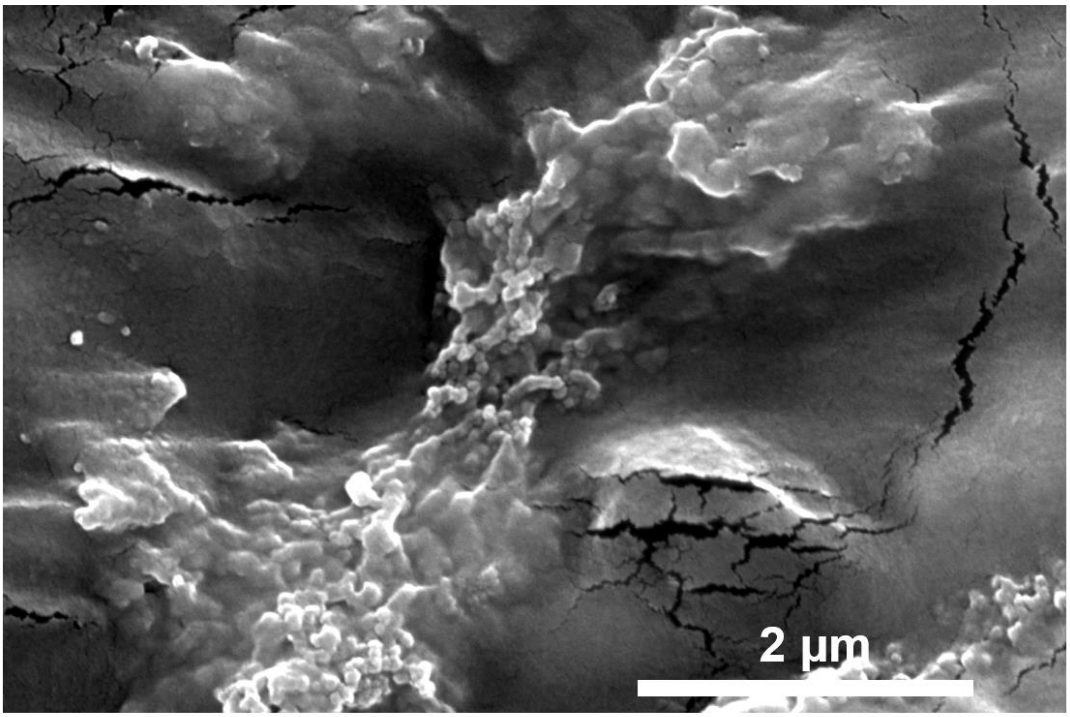

Figure A4.10*: High-magnification SEM image of PVA-MOF-525 composite gel shows the presence of spherical particles, suggesting the formation of MOF-525 in the presence of PVA.*

Sorptive Capacity and Sustained Release of PVA-MOF composite gels

The sorption and release study were performed by Rachel Letteri's group (one of her students Mark Bannon did all the work).

We next sought to examine the sorptive properties of the composite gels, but rather than performing these studies in DMSO, we opted to load and release in aqueous conditions more relevant to drug delivery applications. For these experiments, we used composite gels and Zr-oxo cross-linked PVA containing 3 wt% polymer, as they were easier to cut into uniform samples than the samples with 2 wt% PVA. To exchange the DMSO solvent for water, we dialyzed the DMSO-swollen PVA-UiO-66 composite gels and controls (i.e., MOF powder and PVA-Zr-oxo gel) against DI water (**Figure A4.11**). Since dialysis removes unincorporated organic linker and dissolved Zr-oxo clusters, we used thermal gravimetric analysis (TGA) to compare the compositions (i.e., Zr

content) of the materials before and after solvent exchange.[22] Since TGA was run in air, we assumed the inorganic fraction to be ZrO_2 and calculated the wt% Zr in each sample. The Zr content in the PVA-Zr-oxo control gels decreases substantially from 7.83 to 1.20 wt% Zr during solvent exchange (**Figure A4.12**), indicating that dialysis removes much of the Zr-oxo that is cross-linking polymer chains and these samples are primarily PVA hydrogels. In contrast, the Zr content in the PVA-UiO-66 composite gels decreases from 7.25 to 4.32 wt% Zr (**Figure A4.13**). Since the composite gels lose little Zr during solvent exchange, it is likely that the Zr-oxo clusters in the composites are primarily incorporated into UiO-66. As a control, UiO-66 prepared in the absence of polymer contained an appreciable amount of Zr (21.28 wt%) after dialysis (**Figure A4.14**).

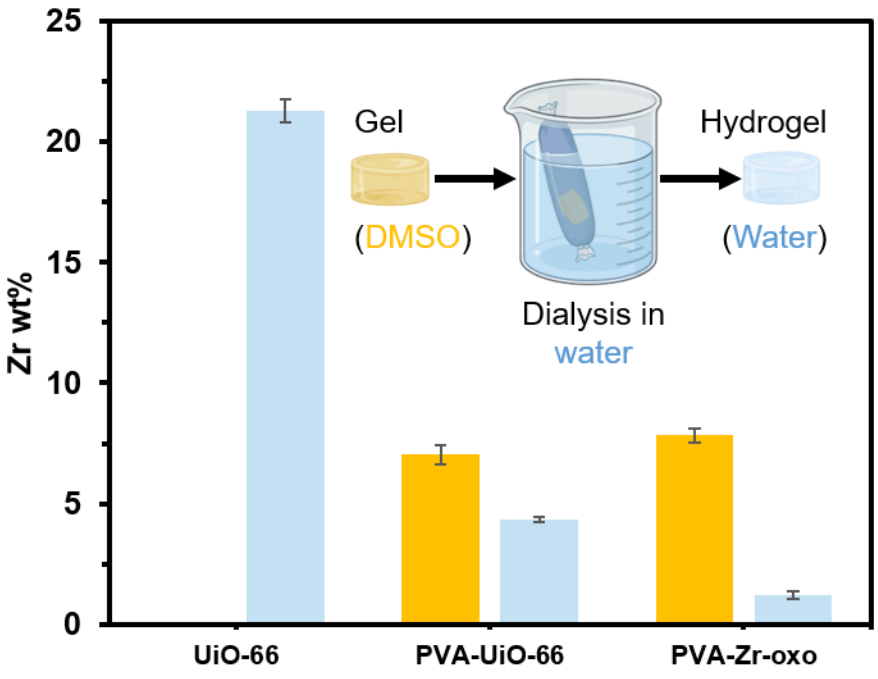

Figure A4.11. *Compositions of composite gels and control samples following solvent exchange from DMSO into water: Zr content before and after solvent exchange of PVA-UiO-66 and PVA-Zr-oxo gels from DMSO (yellow) into water (blue) by dialysis, as determined by TGA in air after drying samples at room temperature for 24 h. Zr content decreased significantly in the PVA-Zr-oxo gels during dialysis, but not in the PVA-UiO-66 composite hydrogels. UiO-66 prepared in the absence of polymer contained 21.28 wt% Zr following dialysis. The Zr content is reported as an average of 3 samples.*

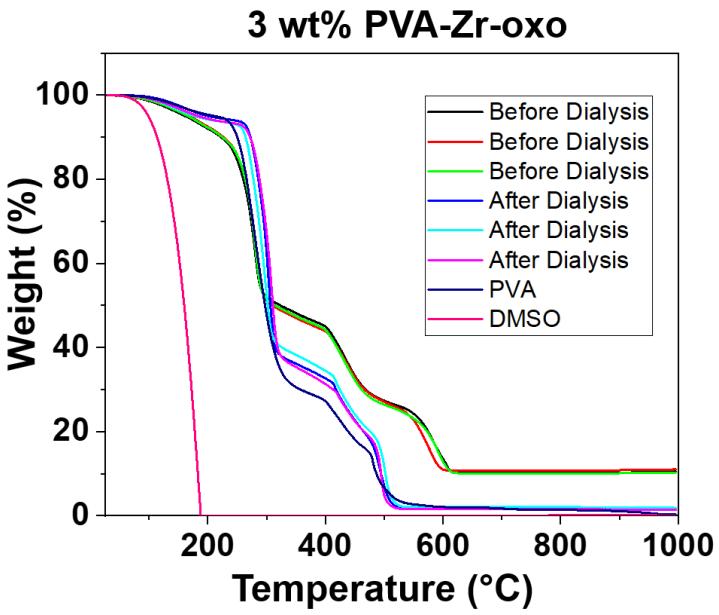

Figure A4.12: *TGA profiles of 3 wt% PVA-Zr-oxo gels before and after dialysis, PVA, and DMSO. After dialyzing the 3 wt% PVA-Zr-oxo gels, the ZrO_2 wt% significantly decreases. The samples were run under air.*

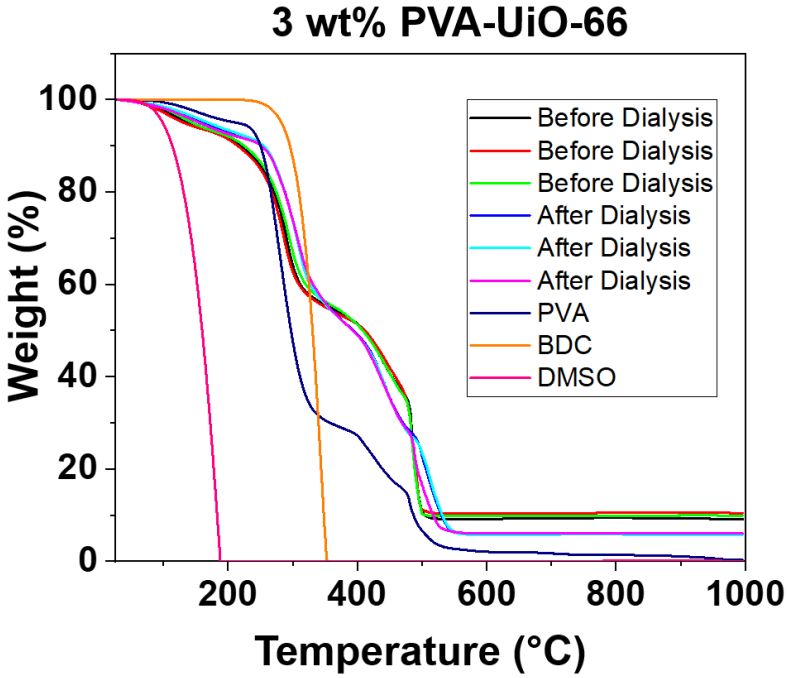

Figure A4.13: *TGA profiles of 3 wt% PVA-UiO-66 composite gels before and after dialysis, BDC linker, PVA, and DMSO. After dialyzing the 3 wt% PVA-UiO-66 composite gels, the ZrO_2 wt% slightly decreases. The samples were run under air.*

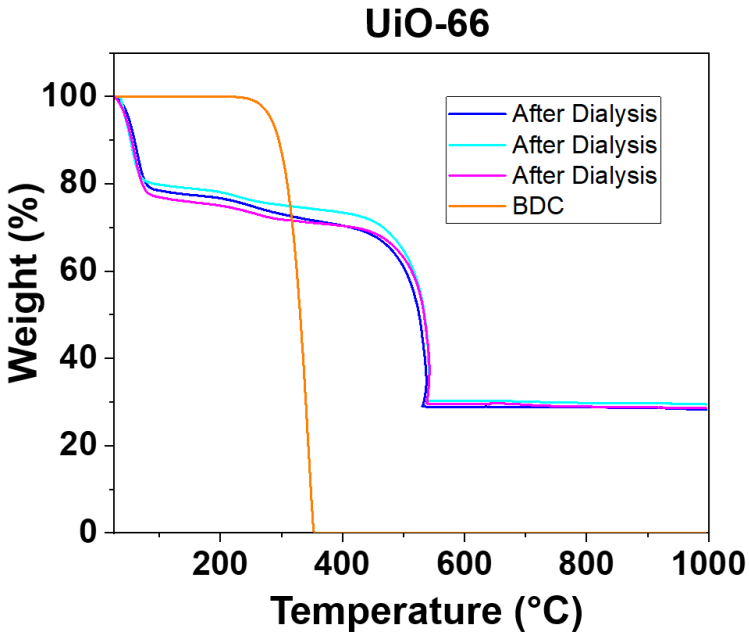

Figure A4.14: *TGA profiles of UiO-66 powder synthesized in DMSO after dialysis and BDC linker. The samples were run under air.*

Having characterized the compositions of the PVA-UiO-66 composite gels, Zr-oxo cross-linked polymer (PVA-Zr-oxo hydrogels containing no MOF linker), and UiO-66 MOF synthesized in the absence of polymer after transfer to aqueous solution, we next compared their sorption characteristics. In these studies, we monitored the sorption of the small molecule dye methylene blue (MB, 319 g/mol) into each formulation by measuring the decrease in MB absorbance (660 nm) in the surrounding solution. After 7 days, sorption plateaued into all formulations and we compared amounts sorbed to determine the contributions of the polymer and MOF constituents to the composite sorption characteristics (**Figure A4.15**).

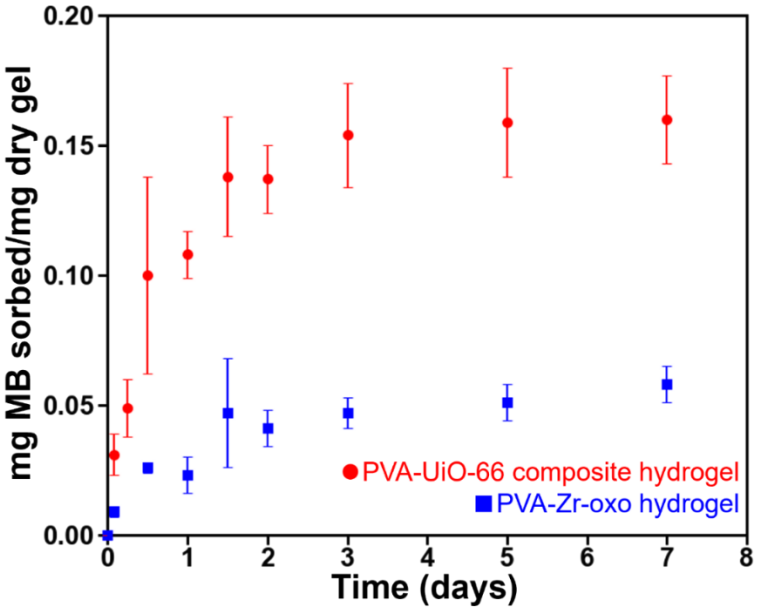

Figure A4.15. *MB Sorption profiles of PVA-UiO-66 composite hydrogels (red) and PVA-Zr-oxo hydrogels (blue) over 7 days, normalized by the dry weight of the carrier. Points on the plot represent the means of 3 independently synthesized samples, and error bars represent the standard deviation of that mean.*

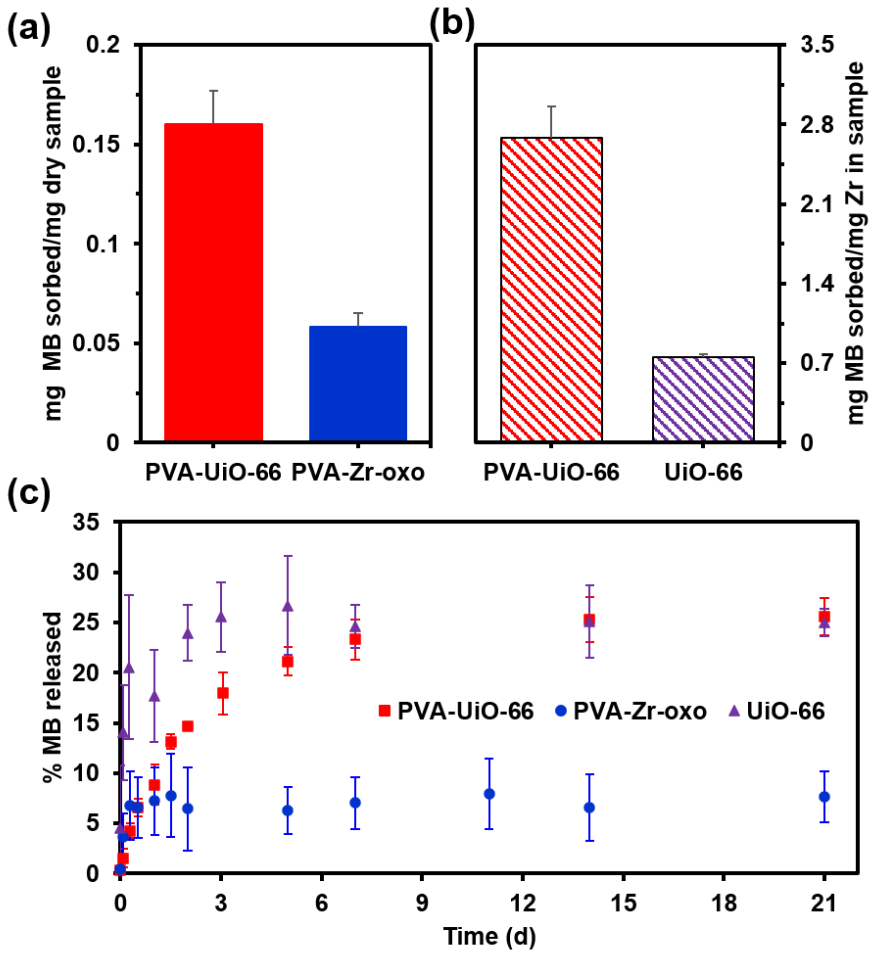

Figure A4.16. *Sorptive capacity and release behavior of PVA-UiO-66 composite hydrogels (red) relative to that of PVA-Zr-oxo hydrogels (blue), and UiO-66 powder (purple). (a) Methylene blue (MB) sorption into the PVA-UiO-66 composite hydrogels and PVA-Zr-oxo hydrogels after 7 days (mg MB/mg dry sorbent) showing UiO-66 incorporation into polymer to increase sorption. (b) MB sorbed into the PVA-UiO-66 composite hydrogels and UiO-66 MOF (mg MB/mg Zr) after 7 days, showing that forming UiO-66 in the presence of PVA increases MB sorption capacity on a per Zr basis (c) Percent of MB released from loaded samples over 21 days. The composite hydrogels (red, circles) sustain MB release over ~7 d, while the PVA-Zr-oxo hydrogels (blue, squares) and MOF-525 powder (purple, triangles) show burst release behavior (~1-2 days). Error bars represent the standard deviation between three separately synthesized samples, with * in the loading data indicating an equal variances two sample t-test giving $p < 0.05$.*

We first compared the sorption of MB into PVA-UiO-66 composite hydrogels and PVA-Zr-oxo samples (essentially PVA hydrogels) to determine how the presence of MOF impacts the sorption properties of the PVA hydrogels (**Figure A4.16a**). The composite hydrogels sorbed significantly more MB (0.16 +/- 0.02 mg MB/mg dry sample) than the PVA-Zr-oxo hydrogels (0.06

+/- 0.01 mg MB/mg dry sample), indicating that the MOF contributes appreciable sorption capacity to these composites.

We next determined how the presence of the polymer impacts the sorption properties of MOFs by comparing MB sorption into PVA-UiO-66 composite hydrogels relative to UiO-66 MOF alone. When adding similar dry weights of these sorbents to MB solution, we found the UiO-66 sample to deplete the surrounding solution of MB (**Figure A4.17**). To ensure saturation of the highly sorptive UiO-66 sample with MB, we instead added MB to each sample based on the Zr content determined from TGA. Given that after dialysis, the Zr content in the samples can be primarily ascribed to intact MOF (**Figure A4.11**), we compared MB sorption on a Zr basis (i.e., mg MB/mg Zr). The composite hydrogels sorbed substantially more MB (2.7 +/- 0.30 mg MB/mg Zr) MB than UiO-66 (0.69 +/- 0.02 mg MB/mg Zr) after 7 days. (**Figure A4.16b**).

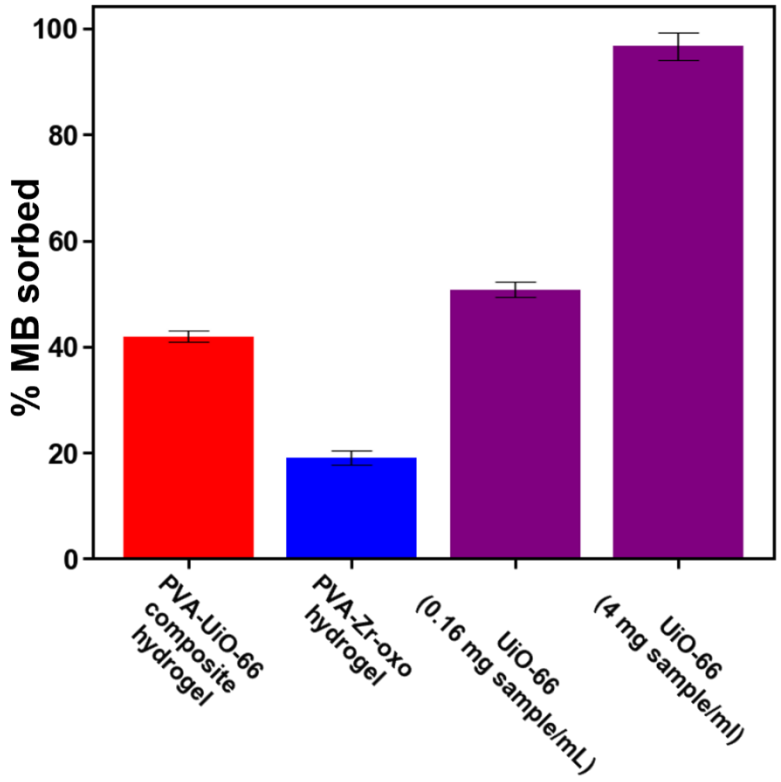

Figure A4.17. *% of MB in solution sorbed by tested carriers after 7 days. Plot depicts PVA-UiO-66 composite hydrogels (red), PVA-Zr-oxo hydrogels (blue), and UiO-66 (purple). Two separate experiments with UiO-66 are depicted, where the concentration of UiO-66 added into the solution was normalized by dry weight (4 mg sample/mL) and by Zr weight (0.16 mg sample/mL), relative to the PVA-UiO-66 composite*

hydrogels. The UiO-66 sample normalized by dry weight (4 mg/mL sample) did not reach sorptive capacity, as it sorbed ~100% of the MB in the solution; however, the Zr weight-normalized sample sorbed ~50% of the MB in the solution, indicating that it reached sorptive capacity. Plotted bars represent the average of 3 independently synthesized samples incubated with MB for 7 days. Error bars represent the standard deviation of the average.

We next studied the release of MB from the composite gels relative to the PVA-Zr-oxo and UiO-66 control samples. After loading the samples with MB for 7 days, we replaced the surrounding solution with an equivalent volume of water and monitored the release of MB into the surrounding solution. The PVA-UiO-66 composite hydrogels sustained MB release for longer than the UiO-66 and PVA-Zr-oxo hydrogel controls (**Figure A4.16c**). This study showed that synthesizing UiO-66 in the presence of polymer resulted in a sustained release profile relative to the PVA-Zr-oxo hydrogel and UiO-66 synthesized in the absence of polymer.

After demonstrating the sorption and release of MB, we investigated the loading and release of larger, therapeutically relevant cargo (*i.e.,* peptides). Angiotensin 1-7 (DRVYIHP, Ang 1-7), a therapeutic peptide with anti-tumor and cardioprotective properties, has an *in vivo* half-life of just 30 min.[39] Encapsulation and sustained release into a carrier such as these composites could offer a way to extend the half-life of Ang1-7. Because Ang 1-7 (899 g/mol) (**Figure A4.18**) is larger than MB (320 g/mol) we first attempted to encapsulate it within UiO-67 and MOF-525, which have larger pores (12 Å and 17 Å, respectively) than UiO-66 (6 Å). Though reverse-phase high performance liquid chromatography showed little decrease in Ang 1-7 absorbance in the outer solution after incubation with a UiO-67 after 27 h, there was no detectable trace of Ang 1-7 in the solution containing MOF-525 (**Figure A4.19**). Therefore, we performed the Ang 1-7 loading and release experiments using PVA-MOF-525 composite hydrogels.

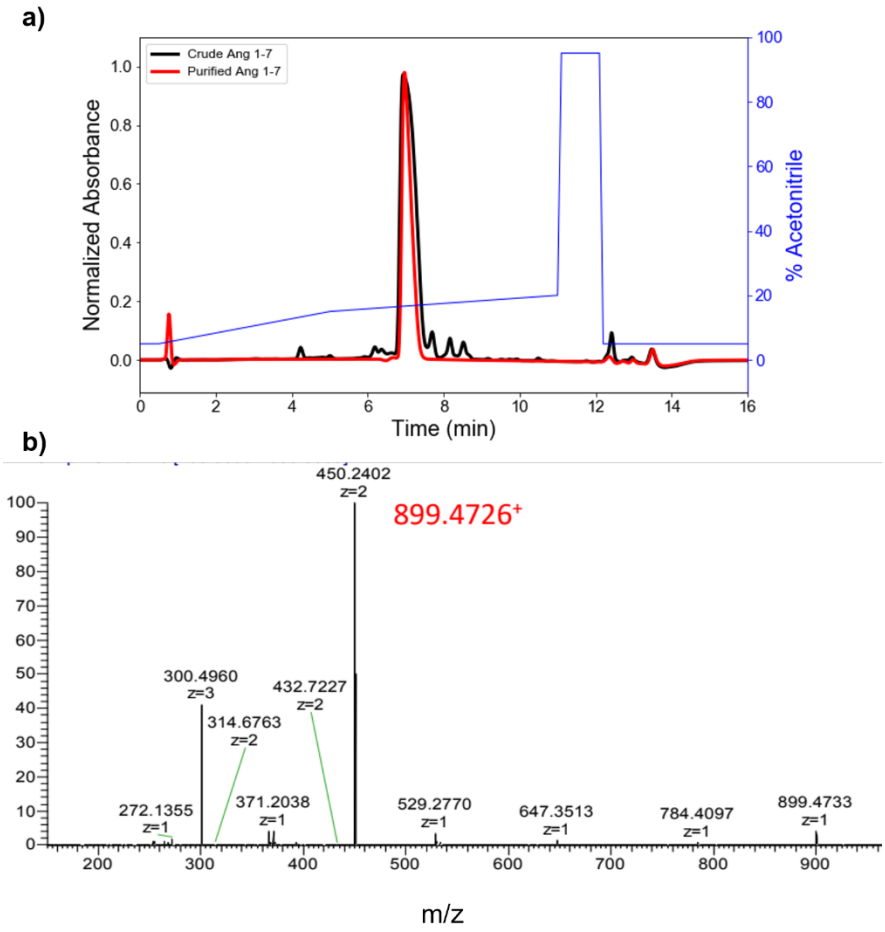

Figure A4.18. *Characterization of Ang 1-7 peptide.* ***a)*** *Analytical reverse phase high performance liquid chromatography (RP-HPLC) of Ang 1-7 before (black) and after purification (red) using preparative scale RP-HPLC. Analytical RP-HPLC was performed on a Waters E2695 Alliance Separations Module, using a 4.5 mm x 50 mm XBridge C18 3.5 µm chromatographic separation column, where the acetonitrile gradient is plotted in blue. Preparative scale RP-HPLC was performed on a Waters Empower system, using a 30 mm x 150 mm XBridge Prep C18 5 µm optimum bed density chromatographic separation columns. UV absorbance was measured at 214 nm.* ***b)*** *Electrospray ionization (ESI) spectrometry of Ang 1-7 after purification. ESI was measured a Thermo Orbitrap Exploris 480 mass spectrometer by the UVA Biomolecular Analysis Core.*

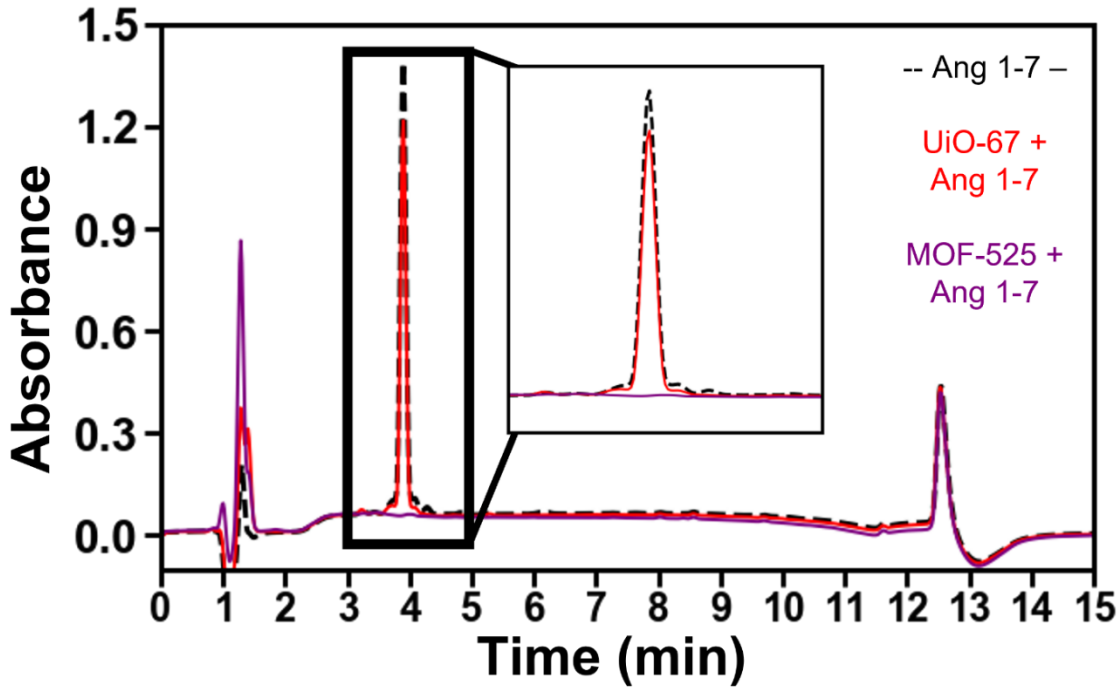

Figure A4.19. *Reverse phase high performance liquid chromatography depicting Ang 1-7 (black) encapsulation into UiO-67 (red) and MOF-525 (purple). Little-to-no decrease in the Ang 1-7 peak (~3.75 min) was detected after incubation with UiO-67, suggesting little-to-no encapsulation of Ang 1-7 in UiO-67. Complete disappearance of the Ang 1-7 peak in the sample incubated with MOF-525 suggests encapsulation of Ang 1-7. Analytical RP-HPLC was performed on a Waters E2695 Alliance Separations Module, using a 4.5 mm x 50 mm XBridge C18 3.5 µm chromatographic separation column. Mobile phase composed of ultrapure water and acetonitrile + 0.1% trifluoroacetic acid, run at a gradient of 15 to 20% acetonitrile from 2 to 12 minutes. UV absorbance was measured at 214 nm.*

To encapsulate Ang 1-7 into PVA-MOF-525 composite hydrogels, PVA-Zr-oxo hydrogels, and MOF-525 powder, we incubated each sample in an aqueous solution of Ang 1-7. After 7 days, we found that the sorption leveled off at 10 +/- 1%, 3 +/- 1%, and 19 +/- 0% of Ang 1-7 added to the surrounding solution for PVA-MOF-525 composite hydrogels, PVA-Zr-oxo hydrogels, and MOF-525, respectively. Here, we report the dry weight normalized sorption data (mg Ang 1-7 sorbed/mg dry material). All 3 tested samples appeared to be saturated with Ang 1-7, as they all only sorbed less than 20% of the available Ang 1-7 in the solution (**Figure A4.20**). The PVA-MOF-525 composite hydrogels sorbed significantly more Ang 1-7 (0.08 +/- 0.01 mg Ang 1-7/mg dry sample) than both the PVA-Zr-oxo hydrogel (0.045 +/- 0.01 mg Ang 1-7/mg dry sample) and the MOF-525 alone (0.01 +/- 0.0 mg Ang 1-7/mg dry sample) (**Figure A4.21a**). The PVA-MOF-525

composite hydrogels still sustained Ang 1-7 release longer (~16 h) than the MOF-525 powder and PVA-Zr-oxo hydrogels, which reached equilibrium at ~8 h. (**Figure A4.21b**).

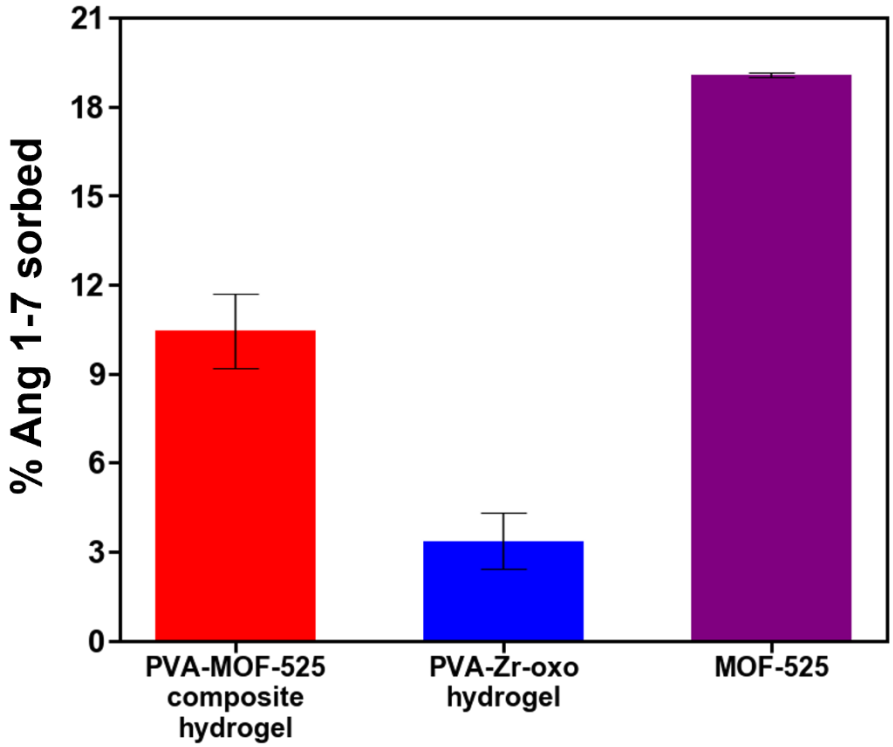

Figure A4.20. *% of Ang 1-7 in solution sorbed by tested carriers. The plot depicts PVA-UiO-66 composite hydrogels (red), PVA-Zr-oxo hydrogels (blue), and MOF -525 (purple). Plotted bars represent the average of 3 independently synthesized samples incubated with Ang 1-7 for 7 days. Error bars represent the standard deviation of the average.*

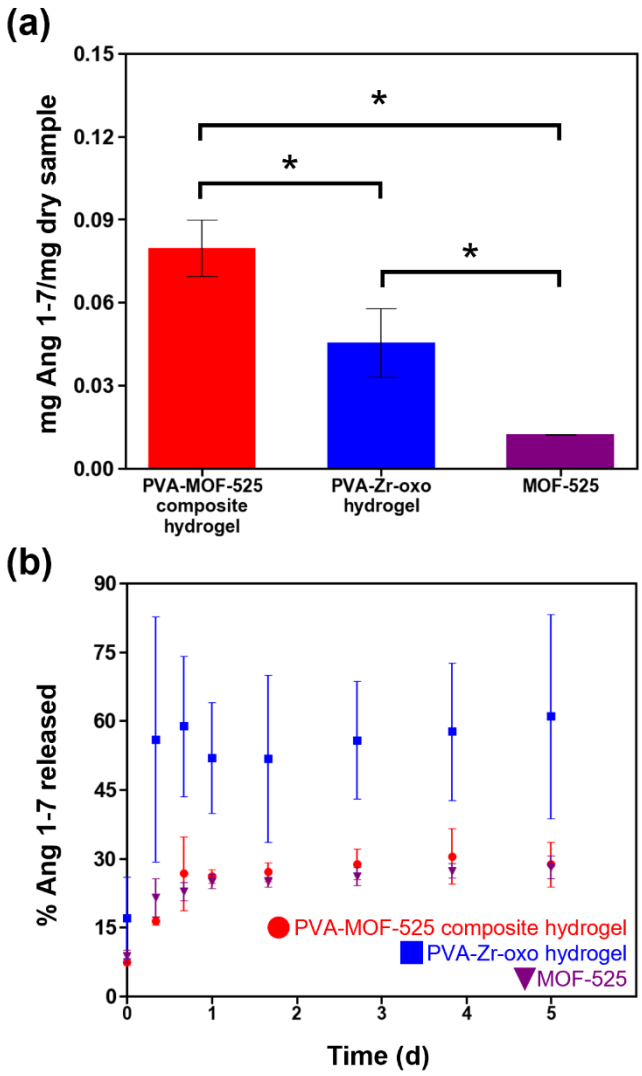

Figure A4.21. *Sorptive capacity and release behavior of PVA-MOF-525 composite hydrogels (red), PVA-Zr-oxo hydrogels (blue), and MOF-525 powder (purple) for the therapeutic peptide Ang 1-7. (a) Amount of Ang 1-7 sorbed into each sample after 7 days, normalized relative to the dry mass of each sample. More Ang 1-7 sorbs into the PVA-MOF-525 composite hydrogels than the PVA-Zr-oxo hydrogels and the MOF-525 powder. (b) Percent of Ang 1-7 released from sorbed samples over 7 days. The composite hydrogels (red, circles) sustain Ang 1-7 release over ~16 h, while the PVA-Zr-oxo hydrogels (blue, squares) and MOF-525 powder (gray, triangles) show a burst release (~8 h). Both sorption and release were calculated by tracking the absorbance of the outer solution using UV-vis spectroscopy at 277 nm. Error bars represent the standard deviation between three separately synthesized samples. *P value < 0.05 with equal variances two sample t-test.*

Encapsulating solutes into MOF-based carriers:

To measure the mass (in mg) of either methylene blue (MB) or the peptide Angiotensin 1-7 (Ang1-7) encapsulated into the MOF-based carriers at any given time (t), or $m(t)_{s,carrier}$, we first prepared an aqueous solution of solute *s* (0.05 mg/mL for MB and). This solution was termed the

"outer solution" (os), and a specific volume, V_{os} (L), was added to each sample. For consistency, we performed the encapsulation experiments with 70 – 80 mg of each gel (4 mg/mL MB solution) and/or 10 – 12 mg of UiO-66 powder (0.16 mg/mL MB solution) in the MB encapsulation experiments, and ~100 – 120 mg gels and/or MOF-525 (10 mg/mL Ang 1-7 solution) in the Ang 1-7 encapsulation experiments.

To determine how to measure the sorption of *s* into each sample at any time t, we performed a mass balance on the solute in the system. Specifically, we considered that the mass of the solute in the carrier at time t, or $m(t)_{s,carrier}$, would be the difference between the total mass of MB in the vial at time t, $m(t)_{s,vial}$, minus that in the outer solution at time t, $m(t)_{s,os}$ (equation 1). We note that the total mass of solute in the vial decreased over time as we removed aliquots for measuring concentration in the outer solution.

To determine measurable values we can use to calculate $m(t)_{s,carrier}$, we performed a MB mass balance on the vial. There are only two phases, the outer solution (os) and the carrier, that can hold *s* in the vial; therefore, the total mass of *s* in the vial at time t ($m(t)_{s,vial}$) is the sum of the mass of *s* in the outer solution ($m(t)_{s,os}$) and $m(t)_{s,carrier}$ at time t (**1**).

(1) $m(t)_{s,vial} = m(t)_{s,os} + m(t)_{s,carrier}$

Because $m(t)_{s,carrier}$ is on the order of single mgs, we can't weight the change of mass in the carrier reliably; therefore, we can convert **(1)**, to solve for $m(t)_{s,vial}$ in terms of the concentration (C, in mM) of s in each phase (**2**). equation 2.

(2) $m(t)_{s,vial} = C(t)_{s,os}V_{os} + m(t)_{s,carrier}$

In equation 2, we assume V_{os} to be constant, as the carriers are swollen when they enter the vial and therefore are unlikely to absorb appreciable amounts water from the outer solution upon incubation. Since we are measuring the absorbance of the outer solution ($A_{\lambda,os}$) at a wavelength (λ) specific to the solute *s*, we convert it to a corresponding concentration ($C(t)_{\lambda,os}$) using the Beer Lambert law (**3**),

(3) $A(t)_{\lambda,os} = (\varepsilon_s b)C(t)_{\lambda,os}$

where ε_s is the molar absorptivity of *s* and *b* is the optical path length in the configuration used, which we lump into one term determined from calibration curves specific to a given solute and instrument configuration. In these experiments, $A(t)_{\lambda,os}$ was measured at the absorbance maximum of each solute *s* (660 nm for MB and 277 nm for Ang 1-7) on a Biotek Synergy 4 plate reader. We developed calibration curves for both MB and Ang 1-7, fitting the data linearly to determine the ($\varepsilon_s b$) term for each solute *s* (5 x 10^{-3} absorbance units/μM MB and 7 x 10^{-4} absorbance units/μM Ang 1-7).

To account for absorbance due to the carrier rather than to solute (e.g., linker that leaches into the outer solution), we placed each sample in two aqueous solutions, one containing *s* and the other containing only water, the latter. Once we subtracted the absorbance of water alone from each sample, we accounted for any absorbance from the carrier at λ by subtracting the absorbance of the control sample ($A(t)_{\lambda,os,cntrl}$) from that of the test sample ($A(t)_{\lambda,os,s}$) (equation 4).

(4) $A(t)_{s,os} = A(t)_{\lambda,os,s} - A(t)_{\lambda,os,cntrl}$

Using our calibration curve for *s*, we then converted $A(t)_{s,os}$ to $C(t)_{s,os}$ (**3**), and solved for $m(t)_{s,os}$ (equation 5).

(5) $m(t)_{s,os} = \frac{A(t)_{s,os}}{(\varepsilon_s b)} V_{os} MW_s$

To measure $A(t)_{s,os}$, we removed an aliquot (with a volume V_a) of the outer solution at each timepoint (V_a = 6 x 10^{-4} L for MB and V_a = 1 x 10^{-4} L for Ang 1-7); however, removing these aliquots also decreased the total mass of MB in the vial, $m(t)_{s,vial}$. The initial absorbance ($A(0)_{s,os}$) was measured immediately after adding each sample to the MB solution. To accurately calculate $m(t)_{s,vial}$, we needed to calculate the mass of *s* in each aliquot ($m(t)_{s,aliquot}$) that we are removing from the vial (**7**) using (**6**).

(6) $m(t)_{s,aliquot} = \frac{A(t)_{s,os}}{(\varepsilon_s b)} V_a MW_s$

In (**7**), we simply replace V_{os}, the volume of the outer solution, with V_a, the constant volume of an aliquot, as $C(t)_{s,os} = C(t)_{s,aliquot}$. After every aliquot, we replaced the volume removed in each aliquot

(V_a) with the same volume of water (not containing *s*) to keep V_{os} constant. We then calculated $m(t)_{s,vial}$ in terms of the initial mass of *s* added to the vial ($m(0)_{s,vial}$) and the sum of the mass of the aliquots removed before the time t (equation 7).

(7) $m(t)_{s,vial} = m(0)_{s,os} - \sum_{i=0}^{t-1} m(t)_{s,aliquot}$

Rewriting equation 7 in terms of absorbance gives us a mass balance on the vial in terms of measured and/or known variables (equation 8).

(8) $m(t)_{s,vial} = \left[\frac{A(0)_{s,os}}{(\varepsilon_s b)} V_{os} - \sum_{i=0}^{t-1} \frac{A(i)_{s,os}}{(\varepsilon_s b)} V_{aliquot}\right] MW_s$

As we now know $m(t)_{s,os}$ and $m(t)_{s,vial}$ in terms of measured values, we can rearrange equation 1 to solve for $m(t)_{s,carrier}$ using the absorbance of *s* in the outer solution (equation 9).

(9) $m(t)_{s,carrier} = \left[\left(A(0)_{s,os} - A(t)_{s,os}\right)V_{os} - \sum_{i=0}^{t-1}\left(A(i)_{s,os}\right)V_{aliquot}\right]\frac{MW_s}{(\varepsilon_s b)}$

After calculating $m(t)_{s,carrier}$, we normalized these values relative to either the dry weight of the carrier or the weight of Zr in the carrier, as indicated. To calculate the dry weight of the carrier we weighed a sample of each hydrogel used in the encapsulation experiments and dried it at room temperature for 24 h. We then weighed the mass of the dried gels and calculated a dry/wet weight ratio for each hydrogel (dry weight of hydrogel/wet weight of hydrogel). The dry mass of each hydrogel used in the encapsulation experiment was calculated by multiplying the wet weight of the gel by this ratio. As we performed the encapsulation experiments using dry MOF powder, we normalized the sorption into the MOF powder by the weight of the MOF added into the vial. The Zr weight of each gel was calculated by multiplying the dry weight of each gel or MOF powder used for encapsulation by the Zr wt%, as determined by TGA.

Release:

After encapsulation was complete, the outer solution of each sample (*s* and *cntrl*) was removed. Each carrier sample was then immersed in the same amount of DI water. To account for the lower molar absorptivity of Ang 1-7 at 277 nm relative to MB at 660 nm, the volume of outer solution was halved (20 mg carrier/mL) in the Ang 1-7 experiments in an effort to increase $A(t)_{s,os}$.

In these experiments, we were interested in determining the mass of solute released into the outer solution as a function of time, or $m(t)_{s,rel}$. To determine $C(t)_{s,os}$, we measured $A(t)_{s,os}$ at each timepoint t. We can directly measure $m(t)_{s,rel}$ through equation 5; however, we still have to account for $m_{s,aliquot}$, as we're removing a mass of *s* from our system for each measurement at time t. Taken together, we can use equation 10 to calculate $m(t)_{s,rel}$ from a measured $A(t)_{s,os}$.

(10) $$m(t)_{s,rel} = \left[\left(A(t)_{s,os}\right)V_{os} + \sum_{i=0}^{t-1}\left(A(i)_{s,os}\right)V_{aliquot}\right]\frac{MW_s}{(\varepsilon_s b)}$$

Here, $m(t)_{s,rel}$ is reported as a % of *s* released in the outer solution, which is calculated by normalizing $m(t)_{s,rel}$ to the total amount of *s* that is in each carrier at the start of the release experiment $m(0)_{s,carrier,rel}$, equal to the amount of *s* encapsulated by the carrier at the end of the encapsulation experiment, or $m(7d)_{s,carrier,encaps}$. Here, we convert $m(t)_{s,rel}$ to a % using equation 11.

(11) % *s* released = $$\frac{m(t)_{s,rel}}{m(7)_{s,carrier,encaps}}$$

Statistics:

Each measurement represents an average of 3 independently synthesized samples, meaning 3 *s* and *cntrl* samples. Error bars represent the standard deviation between these three measurements. Each absorbance measurement represents the average of three individual measurements of one sample, and the standard deviation between these measurements was negligible.

Calculating Zr content from TGA profiles:

Let's take an example of 3 wt% PVA-UiO-66 composite gel before dialysis.

Initial mass = 7.34 mg

After heating the sample to 1000 ºC,

Final mass = 0.66 mg

Since TGA was run under oxidative environment, the final mass corresponds to zirconia (ZrO_2). Therefore,

Mass of ZrO_2 = 0.66 mg

Based on the mass of ZrO_2, the mass of Zr was calculated using the following equation:

Mass of Zr = $\frac{g\ of\ ZrO_2}{\frac{123.22\ g\ of\ ZrO2}{mol}} * \frac{91.22\ g\ of\ Zr}{mol}$

So, in case of 3 wt% PVA-UiO-66,

Mass of Zr = 0.49 mg

The Zr content in the sample was calculated using the following equation:

% Zr = $\frac{Mass\ of\ Zr}{Inital\ mass} * 100\%$

% Zr = $\frac{0.49\ mg}{7.34\ mg} * 100\%$ = 6.68%

Plate reader absorbance measurements:

The absorbance of MB and Ang 1-7 were measured at 660 nm and 277 nm, respectively, on a Biotek Synergy 4 plate reader. Calibration curves were developed in triplicate through serial dilution of the MB and Ang 1-7 stock solution.

4.7 References

(1) Furukawa, H.; Cordova, K. E.; O'Keeffe, M.; Yaghi, O. M. The Chemistry and Applications of Metal-Organic Frameworks. *Science* **2013**, *341* (6149), 1230444.

(2) Mondloch, J. E.; Katz, M. J.; Isley, W. C.; Ghosh, P.; Liao, P.; Bury, W.; Wagner, G. W.; Hall, M. G.; Decoste, J. B.; Peterson, G. W.; Snurr, R. Q.; Cramer, C. J.; Hupp, J. T.; Farha, O. K. Destruction of Chemical Warfare Agents Using Metal-Organic Frameworks. *Nat. Mater.* **2015**, *14* (5), 512–516.

(3) Ricco, R.; Pfeiffer, C.; Sumida, K.; Sumby, C. J.; Falcaro, P.; Furukawa, S.; Champness, N. R.; Doonan, C. J. Emerging Applications of Metal-Organic Frameworks. *CrystEngComm* **2016**, *18* (35), 6532–6542.

(4) Lu, K.; Aung, T.; Guo, N.; Weichselbaum, R.; Lin, W. Nanoscale Metal–Organic Frameworks for Therapeutic, Imaging, and Sensing Applications. *Adv. Mater.* **2018**, *30* (37), 1–20.

(5) Zhao, X.; Wang, Y.; Li, D. S.; Bu, X.; Feng, P. Metal–Organic Frameworks for Separation. *Adv. Mater.* **2018**, *30* (37), 1–34.
(6) Zhan, X. Q.; Tsai, F. C.; Xie, L.; Zhang, K. D.; Liu, H. L.; Ma, N.; Shi, D.; Jiang, T. Ligands-Coordinated Zr-Based MOF for Wastewater Treatment. *Nanomaterials* **2018**, *8* (9), 1–13.
(7) Abánades Lázaro, I.; Forgan, R. S. Application of Zirconium MOFs in Drug Delivery and Biomedicine. *Coord. Chem. Rev.* **2019**, *380*, 230–259.
(8) Sun, X. Y.; Zhang, H. J.; Zhao, X. Y.; Sun, Q.; Wang, Y. Y.; Gao, E. Q. Dual Functions of PH-Sensitive Cation Zr-MOF for 5-Fu: Large Drug-Loading Capacity and High-Sensitivity Fluorescence Detection. *Dalt. Trans.* **2021**, *50* (30), 10524–10532.
(9) Sule, R.; Mishra, A. K.; Nkambule, T. T. Recent Advancement in Consolidation of MOFs as Absorbents for Hydrogen Storage. *Int. J. Energy Res.* **2021**, *45* (9), 12481–12499.
(10) Fan, L.; Kang, Z.; Li, M.; Sun, D. Recent Progress in Pristine MOF-Based Catalysts for Electrochemical Hydrogen Evolution, Oxygen Evolution and Oxygen Reduction. *Dalt. Trans.* **2021**, *50* (17), 5732–5753.
(11) Tang, L.; Gong, L.; Xu, Y.; Wu, S.; Wang, W.; Zheng, B.; Tang, Y.; Zhang, D.; Tang, J.; Zheng, J. Mechanically Strong Metal–Organic Framework Nanoparticle-Based Double Network Hydrogels for Fluorescence Imaging. *ACS Appl. Nano Mater.* **2022**, *5* (1), 1348–1355.
(12) Sappia, L. D.; Tuninetti, J. S.; Ceolín, M.; Knoll, W.; Rafti, M.; Azzaroni D Sappia, O. L.; Tuninetti, J. S.; Ceolín, M.; Rafti, M.; Azzaroni, O.; Knoll, W. MOF@PEDOT Composite Films for Impedimetric Pesticide Sensors. *Global Challenges* **2020**, 4, 1900076.
(13) Wang, M.; Huang, H.; Ma, X.; Huang, C.; Peng, X. Copper Metal-Organic Framework Embedded Carboxymethyl Chitosan-g-Glutathione/Polyacrylamide Hydrogels for Killing Bacteria and Promoting Wound Healing. *Int. J. Biol. Macromol.* **2021**, *187*, 699–709.
(14) Nie, W.; Huang, Y.; Wang, Y.; Kengla, C.; Scott Copus, J.; Sun, J.; Shao, Z.; Dai, X.; Shen, Y. Temperature Sensitive PolyMOF Hydrogel Formed by in Situ Open-Ring Polymerization for Infected Chronic Wound Treatment. *Chem. Eng. J.* **2022**, *446* (P2), 136948.
(15) Gwon, K.; Han, I.; Lee, S.; Kim, Y.; Lee, D. N. Novel Metal-Organic Framework-Based Photocrosslinked Hydrogel System for Efficient Antibacterial Applications. *ACS Appl. Mater. Interfaces* **2020**, *12* (18), 20234–20242.
(16) Javanbakht, S.; Nabi, M.; Shadi, M.; Amini, M. M.; Shaabani, A. Carboxymethyl Cellulose/Tetracycline@UiO-66 Nanocomposite Hydrogel Films as a Potential Antibacterial Wound Dressing. *Int. J. Biol. Macromol.* **2021**, *188*, 811–819.
(17) Denny, M. S.; Cohen, S. M. In Situ Modification of Metal–Organic Frameworks in Mixed-Matrix Membranes. *Angew. Chemie Int. Ed.* **2015**, *54* (31), 9029–9032.
(18) Zhao, R.; Ma, T.; Zhao, S.; Rong, H.; Tian, Y.; Zhu, G. Uniform and Stable Immobilization of Metal-Organic Frameworks into Chitosan Matrix for Enhanced Tetracycline Removal from Water. *Chem. Eng. J.* **2020**, *382*, 122893.
(19) Mahmoud, M. E.; Mohamed, A. K. Novel Derived Pectin Hydrogel from Mandarin Peel Based Metal-Organic Frameworks Composite for Enhanced Cr(Vl) and Pb(II) Ions Removal. *Int. J. Biol. Macromol.* **2020**, *164*, 920–931.
(20) Allegretto, J. A.; Giussi, J. M.; Moya, S. E.; Azzaroni, O.; Rafti, M. Synthesis and Characterization of Thermoresponsive ZIF-8@PNIPAm-: Co-MAA Microgel Composites with Enhanced Performance as an Adsorption/Release Platform. *RSC Adv.* **2020**, *10* (5), 2453–2461.
(21) Lim, J.; Lee, E. J.; Choi, J. S.; Jeong, N. C. Diffusion Control in the in Situ Synthesis of Iconic Metal-Organic Frameworks within an Ionic Polymer Matrix. *ACS Appl. Mater. Interfaces* **2018**, *10* (4), 3793–3800.
(22) Klein, S. E.; Sosa, J. D.; Castonguay, A. C.; Flores, W. I.; Zarzar, L. D.; Liu, Y. Green Synthesis of Zr-Based Metal-Organic Framework Hydrogel Composites and Their Enhanced Adsorptive Properties. *Inorg. Chem. Front.* **2020**, *7* (24), 4813–4821.
(23) Zhu, H.; Zhang, Q.; Zhu, S. Alginate Hydrogel: A Shapeable and Versatile Platform for in Situ Preparation of Metal-Organic Framework-Polymer Composites. *ACS Appl. Mater. Interfaces* **2016**, *8* (27), 17395–17401.
(24) Lawson, S.; Alwakwak, A. A.; Rownaghi, A. A.; Rezaei, F. Gel-Print-Grow: A New Way of 3D Printing Metal-Organic Frameworks. *ACS Appl. Mater. Interfaces* **2020**, *12* (50), 56108–56117.
(25) Garai, A.; Shepherd, W.; Huo, J.; Bradshaw, D. Biomineral-Inspired Growth of Metal-Organic Frameworks in Gelatin Hydrogel Matrices. *J. Mater. Chem. B* **2013**, 1 (30), 3678–3684.

(26) Zhuang, Y.; Kong, Y.; Wang, X.; Shi, B. Novel One Step Preparation of a 3D Alginate Based MOF Hydrogel for Water Treatment. *New J. Chem.* **2019**, *43* (19), 7202–7208.
(27) Wang, Y.; Peng, H.; Wang, H.; Zhang, M.; Zhao, W.; Zhang, Y. In-Situ Synthesis of MOF Nanoparticles in Double-Network Hydrogels for Stretchable Adsorption Device. *Chem. Eng. J.* **2022**, *450* (P3), 138216.
(28) Wang, T. C.; Vermeulen, N. A.; Kim, I. S.; Martinson, A. B. F.; Stoddart, J. F.; Hupp, J. T.; Farha, O. K. Scalable Synthesis and Post-Modification of a Mesoporous Metal-Organic Framework Called NU-1000. *Nat. Protoc.* **2016**, *11* (1), 149–162.
(29) DeStefano, M. R.; Islamoglu, T.; Garibay, S. J.; Hupp, J. T.; Farha, O. K. Room-Temperature Synthesis of UiO-66 and Thermal Modulation of Densities of Defect Sites. *Chem. Mater.* **2017**, *29* (3), 1357–1361.
(30) Islamoglu, T.; Otake. K.; Li, P.; Buru, C.T.; Peters, A.W.; Akpinar, I.; Garibay, S.J.; Farha, O. K. Revisiting the Structural Homogeneity of NU-1000, a Zr-Based Metal–Organic Framework. *CrystEngComm* **2018**, *20* (39), 5913-5918.
(31) Huelsenbeck, L.; Luo, H.; Verma, P.; Dane, J.; Ho, R.; Beyer, E.; Hall, H.; Geise, G. M.; Giri, G. Generalized Approach for Rapid Aqueous MOF Synthesis by Controlling Solution PH. *Cryst. Growth Des.* **2020**, *20* (10), 6787–6795.
(32) Wang, A.; Barcus, K.; Cohen, S. M. Quantifying Ligand Binding to the Surface of Metal − Organic Frameworks. *J. Am. Chem. Soc.* **2023**, *145* (30), 16821-16827.
(33) Destefano, M. R.; Islamoglu, T.; Garibay, S. J.; Hupp, J. T.; Farha, O. K. Room-Temperature Synthesis of UiO-66 and Thermal Modulation of Densities of Defect Sites. *Chem. Mater.* **2017**, *29* (3), 1357–1361.
(34) Verma, P. K.; Huelsenbeck, L.; Nichols, A. W.; Islamoglu, T.; Heinrich, H.; Machan, C. W.; Giri, G. Controlling Polymorphism and Orientation of NU-901/NU-1000 Metal-Organic Framework Thin Films. *Chem. Mater.* **2020**, *32* (24), 10556–10565.
(35) Chavan, S.; Vitillo, J. G.; Gianolio, D.; Zavorotynska, O.; Civalleri, B.; Jakobsen, S.; Nilsen, M. H.; Valenzano, L.; Lamberti, C.; Lillerud, K. P.; Bordiga, S. H 2 Storage in Isostructural UiO-67 and UiO-66 MOFs. *Phys. Chem. Chem. Phys.* **2012**, *14* (5), 1614–1626.
(36) Morris, W.; Volosskiy, B.; Demir, S.; Gándara, F.; McGrier, P. L.; Furukawa, H.; Cascio, D.; Stoddart, J. F.; Yaghi, O. M. Synthesis, Structure, and Metalation of Two New Highly Porous Zirconium Metal-Organic Frameworks. *Inorg. Chem.* **2012**, *51* (12), 6443–6445.
(37) MacRae, C. F.; Sovago, I.; Cottrell, S. J.; Galek, P. T. A.; McCabe, P.; Pidcock, E.; Platings, M.; Shields, G. P.; Stevens, J. S.; Towler, M.; Wood, P. A. Mercury 4.0: From Visualization to Analysis, Design and Prediction. *J. Appl. Crystallogr.* **2020**, *53*, 226–235.
(38) Patterson, A. L. The Scherrer Formula for X-Ray Particle Size Determination. *Phys. Rev.* **1939**, *56* (10), 978–982.
(39) Lau, J. L.; Dunn, M. K. Therapeutic Peptides: Historical Perspectives, Current Development Trends, and Future Directions. *Bioorganic Med. Chem.* **2018**, *26* (10), 2700–2707.

Chapter 5 Conclusion and Future Work

Promising applications of metal-organic frameworks (MOFs) can be fulfilled by making MOF composites as thin films and polymer-MOF gels. MOF thin films have the potential in catalysis, sensing, and separation, while polymer-MOF gels are useful for therapeutic applications. However, the MOF field is relatively young and the challenges still exist. This thesis aims to address some of those challenges. We presented several methods to control the crystallization of MOFs on the substrate and in the presence of polymers. The methods developed here will pave the way to engineer MOF-based composites for target applications.

5.1 Controlling Polymorphism and Orientation of NU-901/NU-1000 Metal–Organic Framework Thin Films Using Solvothermal Method

Chapter 2 demonstrated a unique way to control the orientation of the NU-1000 MOF. Rather than relying on the stochastic nature of nucleation to direct orientation, controlling nucleation is a more effective method. We find that the presence of Zr-oxo clusters on the substrate during the MOF formation results in the growth of NU-1000 crystals in the perpendicular direction. We suggest that nucleation density increases due to the presence of Zr-oxo clusters on the substrate and this increased nucleation density allows growth in perpendicular direction.

Future work could investigate how the orientation of NU-1000 crystals affects its performance on electrocatalysis.[1] It's possible that catalyst nanoparticles may not diffuse into NU-1000 pores during parallel orientation, while may diffuse during perpendicular orientation. In that case, catalytic activity will be higher for perpendicular orientation compared to parallel orientation. This technique could be further expanded to other anisotropic MOFs like MOF-545.[2]

5.2 Solution Shearing to Make Thin Films of Metal–Organic Frameworks

Chapter 3 expands the solution shearing technique to make thin films of Zr-based MOFs. We show the formation of UiO-66 thin films using solution shearing and study the effects of temperature, blade speed, precursor concentration, and solvent on thin film properties (i.e., thickness, crystal orientation, and surface coverage). We further show the formation of MOFs containing tetratropic linker, like NU-901 and MOF-525, and their potential in electrocatalysis. Overall, we show that solution shearing is a versatile tool and offers many parameters to tune thin film properties.

Future work on this will be to make thin films of anisotropic MOFs like NU-1000 and MOF-545 (**Figure 5.1**). The large pore MOFs are particularly useful in catalysis,[1] where large pores allow fast diffusion of reactant and products in and out of MOF pores. It will be interesting to make the perpendicularly oriented NU-1000 crystals using solution shearing. Hopefully, this work motivates the development of a roll-to-roll coating process to make MOF thin films at industrial scale.

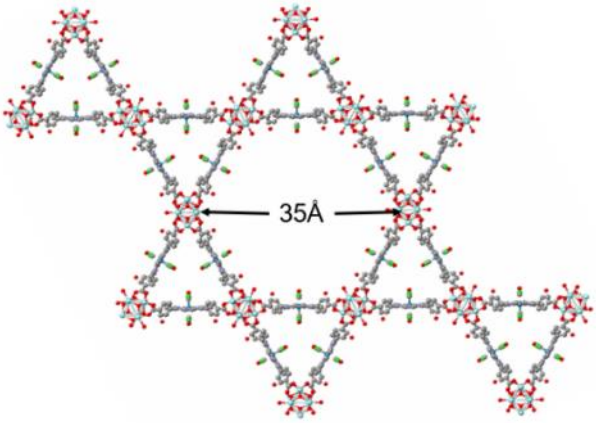

Figure 5.1. *Crystal structure of MOF-525 generated using Mercury.[3] Zr, C, and O have been represented in cyan, grey, and red, respectively.*

5.3 Understanding the effects of interactions between polymers and metal–organic frameworks (MOFs) on polymer-MOF composite gel formation

In chapter 4, we shed light on how the interactions between polymers and MOFs affect MOF formation/crystallinity within polymer-MOF composite gels, which could inform future design of these composite gels. We find that polymers having carboxylic acid groups outcompete linker to bind metal clusters and inhibit MOF formation within the gel. On the other hand, polymers having hydroxyl groups does not disrupt MOF formation within the gel. Excitingly, we find the

possibility of polymer entrapment within the MOF pores, which restricts the movement of polymer chains out of the MOF pores and facilitate gelation.

Future work will focus on understanding the gel mechanics as a function of polymer-MOF interactions. It would be interesting to see how the MOF chemistry (metal cluster and linker) affect gel mechanics. Also, we want to expand the synthesis process to large-pore MOFs, like NU-1000 and MOF-545. Specifically, the synthesis of PVA-NU-1000 and PVA-MOF-545 composite gels is beneficial to study the loading and release of protein, which has implications in therapeutics.

We also want to study the nucleation and growth of MOF in the presence of polymers studied in chapter 4 using *in-situ* SAXS/WAXS. This will help us answer the question whether polymer is getting entrapped inside the pores or not?

5.4 Final Remarks

This works presents interesting insights on the MOF crystallization in the presence of a solid substrate and polymers. Although MOFs have shown great potential in various fields, implementation of MOFs at industrial scale is still a challenge. The author wishes that this work will help in developing the technologies to implement MOFs at industrial scale.

5.5 References

(1) Kung, C. W.; Mondloch, J. E.; Wang, T. C.; Bury, W.; Hoffeditz, W.; Klahr, B. M.; Klet, R. C.; Pellin, M. J.; Farha, O. K.; Hupp, J. T. Metal-Organic Framework Thin Films as Platforms for Atomic Layer Deposition of Cobalt Ions to Enable Electrocatalytic Water Oxidation. *ACS Appl. Mater. Interfaces* **2015**, *7* (51), 28223–28230.

(2) Morris, W.; Volosskiy, B.; Demir, S.; Gándara, F.; McGrier, P. L.; Furukawa, H.; Cascio, D.; Stoddart, J. F.; Yaghi, O. M. Synthesis, Structure, and Metalation of Two New Highly Porous Zirconium Metal-Organic Frameworks. *Inorg. Chem.* **2012**, *51* (12), 6443–6445.

(3) Macrea, C.F.; Sovago, I.; Cottrell, S.J.; Galek, P.T.A.; McCabe, P.; Pidcock, E.; Platings, M.; Shields, G.P.; Stevens, J.S.; Towler, M.; Wood, P.A. Mercury 4.0: From Visualization to Analysis, Design, and Prediction. *J. Appl. Cryst.* **2020**, *53*, 226-235.